Title
Highly controlled fabrication of carbon nanotube based probes for atomic force microscopy

Author
Chen, I-Chen

Publication Date
2007

UNIVERSITY OF CALIFORNIA, SAN DIEGO

Highly Controlled Fabrication of Carbon Nanotube Based Probes for Atomic Force Microscopy

A dissertation submitted in partial satisfaction of the
requirements for the degree Doctor of Philosophy
in
Materials Science and Engineering

by

I-Chen Chen

Committee in Charge:

Professor Sungho Jin, Chair
Professor Prabhaker Bandaru
Professor Yu-Hwa Lo
Professor Vitali Nesterenko
Professor Lea M. Rudee

2007

The dissertation of I-Chen Chen is approved, and it is acceptable in quality and form for publication on microfilm:

Chair

University of California, San Diego

2007

Dedicated to my parents

TABLE OF CONTENTS

CHAPTER 1: INTRODUCTION

CHAPTER 2: FUNDAMENTALS OF ATOMIC FORCE MICROSCOPY

CHAPTER 3: FABRICATION OF CARBON NANOTUBE BASED PROBES

CHAPTER 4: CONTROL OF CANTILEVER BENDING DURING GROWTH

CHAPTER 5: HIGH RESOLUITON AFM IMAGING USING CNT PROBES

LIST OF FIGURES

LIST OF TABLES

ACKNOWLEDGEMENTS

I am deeply grateful to my advisor, Professor Sungho Jin, for his strong support and guidance during the course of this research work. I would like to thank Dr. Christine Orme of Lawrence Livermore National Lab for being my co-advisor and valuable discussion and direction. I also appreciate Dr. Leon Chen for his encouragement and assistance in the lab.

I wish to express my gratefulness to my committee members for their time and helpful suggestions: Professor Lea M. Rudee, Professor Vitali Nesterenko, Professor Yu-Hwa Lo, and Professor Prabhaker Bandaru.

It has been a great experience to work in the Jin's group. I would like to thank to Dr. Xiang-Rong Ye for his encouragement and useful discussions, and Joseph AuBuchon, Chiara Daraio and Andy Gapin for their assistance in various aspects of this work. My experience in UC San Diego was enriched by friends. I would like to thank each and all of them for their help in and out of my research. In particular, I would like to express my appreciation to Xing Zhang for his company and help, especially while I had surgeries and recovered in Taiwan.

I deeply thank the following collaborators and individuals from outside the group: Prof. Ratnesh Lal, Arjan Quist, Julie Muyco, Jeremy Gray, Jennifer Giocondi, Timothy Ratto, Robert Rudd and Prof. Michael Sailor. Without their help, it would surely have been more difficult finishing this work.

The parts of the following papers were selected as the content of this study: "Extremely Sharp Carbon Nanocone Probes for Atomic Force Microscopy Imaging", I.-C. Chen, L.-H. Chen, X.-R. Ye, C. Daraio, S. Jin, C. A. Orme, A. Quist and R. Lal, Applied Physics Letters 88, 153102 (2006), “Fabrication of high-aspect-ratio carbon nanocone probes by electron beam induced deposition patterning”, I.-C. Chen, L.-H. Chen, C. A. Orme, A. Quist, R. Lal and S. Jin, Nanotechnology 17, 4322 (2006), “Control of curvature in highly compliant probe cantilevers during carbon nanotube growth”, I.-C. Chen, L.-H. Chen, C. A. Orme and S. Jin, Nano Letters (in press) and “Iron-platinum coated carbon nanocone probes on tipless cantilevers for high resolution magnetic force imaging”, I.-C. Chen, L.-H. Chen, A. I. Gapin, S. Jin, L. Yuan and S.-H. Liou, Nanotechnology (Submitted). The dissertation author was the primary investigator and author of these papers.

I graciously acknowledge the financial support from the National Science Foundation (NSF-NIRT grant numbers DMR-0210559 and DMI-0303790), the University of California Discovery Fund (grant number ele02-10133/Jin and ele05-10241/Jin), Lawrence Livermore National Lab (grant number MI-04-006), National Institute of General Medical Sciences (GM056290) and the Philip Morris External Grant Program.

Last but not least, thanks to my parents for their love and encouragement, which have been a source of strength to me all my life. I also wish to thank my many friends and other colleagues who are too numerous to mention all by name.

VITA

1974	Born in Taichung, Taiwan
1996	B.S., Materials Science and Engineering, National Cheng Kung University, Taiwan
1998	M.S., Materials Science and Engineering, National Cheng Kung University, Taiwan
2007	Ph.D., Materials Science and Engineering, University of California, San Diego

JOURNAL PUBLICATIONS

1. I.-C. Chen, L.-H. Chen, C. A. Orme and S. Jin, “Control of curvature in highly compliant probe cantilevers during carbon nanotube growth”, Nano Letters (in press).

2. I.-C. Chen, L.-H. Chen, X.-R. Ye, C. Daraio, S. Jin, C. A. Orme, A. Quist and R. Lal, “Extremely Sharp Carbon Nanocone Probes for Atomic Force Microscopy Imaging”, Applied Physics Letters 88, 153102 (2006)

3. I.-C. Chen, L.-H. Chen, C. A. Orme, A. Quist, R. Lal and S. Jin,, “Fabrication of high-aspect-ratio carbon nanocone probes by electron beam induced deposition patterning”, Nanotechnology 17, 4322 (2006).

4. L. -H. Chen, J. F. AuBuchon, I. -C. Chen, C. Daraio, X. -R. Ye, A. I. Gapin, S. Jin, C. M. Wang, ”Growth of Aligned Carbon Nanotubes on Carbon Microfibers by DC Plasma-Enhanced Chemical Vapor Deposition”, Applied Physics Letters 88, 033103 (2006).

5. X. R. Ye, L. H. Chen, C. Wang, J. F. Aubuchon, I. C. Chen, A. I. Gapin, J. B. Talbot and S. Jin, “Electrochemical Modification of Vertically Aligned Carbon Nanotube Arrays”, Journal of Physical Chemistry B 110, 12938 (2006).

6. D. –W. Kim, L. -H. Chen, J. F. AuBuchon, I.-C. Chen, S. –H. Jeong, I. K. Yoo, S. Jin, “Prevention of Si-contaminated nanocone formation during plasma enhanced chemical vapor deposition growth of carbon nanotubes”, Carbon 43, 835 (2005).

7. I.-C. Chen, L.-H. Chen, A. I. Gapin, S. Jin, L. Yuan and S.-H. Liou, “Iron-platinum coated carbon nanocone probes on tipless cantilevers for high resolution magnetic force imaging”, Nanotechnology (Submitted).

ABSTRACT OF THE DISSERTATION

Highly Controlled Fabrication of Carbon Nanotube Based Probes for
Atomic Force Microscopy
by
I-Chen Chen
Doctor of Philosophy in Materials Science and Engineering
University of California, San Diego, 2007
Professor Sungho Jin, Chair

This thesis describes a fabrication process to grow a single carbon nanotube (CNT) based probe on an atomic force microscopy (AFM) cantilever by direct current plasma enhanced chemical vapor deposition (DC-PECVD). Electron beam induced deposition (EBID) of carbon dots is utilized for catalyst patterning without using any e-beam resist. Its resist-free characteristic makes EBID a good choice for fabrication of patterns on the edge of the cantilever. CNT probes with < 10 nm tip radius and desired growth direction were produced by electric-field-guided DC-PECVD growth. This process is also capable of being integrated in batch fabrication.

A tunable CNT growth technique was also developed to control the plasma-induced surface stresses on cantilever beams during PECVD process. By introducing hydrogen gas to the (acetylene + ammonia) feed gas during CNT growth and adjusting the ammonia to hydrogen flow ratio, the cantilever surface stress can be altered from compressive to tensile stress, and in doing so controlling the degree of cantilever bending. This technique enables us to solve the serious bending of low stiffness cantilevers after PECVD growth, which makes the CNT probe unsuitable for AFM measurements.

High resolution imaging of thin film specimens and deep trenches were demonstrated using these CNT based probes in tapping-mode, as well as in contact-mode. The mechanical durability of CNT probes was examined by continuous scanning on silicon nitride surface. No degradation in imaging performance was observed after 8 hours of operation. Additionally, high coercivity iron-platinum coated CNT probes have been fabricated for magnetic force microscopy (MFM) applications. The FePt-coated CNT probe has much localized magnetic stray field due to the high-aspect-ratio geometry and small radius of the tip. The MFM imaging on magnetic recording media was performed, and images with 20 nm lateral resolution have been demonstrated.

CHAPTER 1: INTRODUCTION

1.1 Introduction of atomic force microscopy

Scanning probe microscopy is a new branch of microscopy that forms images of surfaces based on detection of interactions between a physical probe and a specimen surface. The first demonstrated scanning probe microscope (SPM) was the scanning tunneling microscope (STM), which was developed by G. Binnig and H. Rohrer of IBM's Zurich Lab in Switzerland.[1] In this technique, the atomic scale image is obtained by monitoring the electric tunneling current between a metallic tip and sample surface when the tip is brought sufficiently close to the surface and raster scanned.

STM is dependent on the conductivity of the sample being imaged. Since a finite tunneling current is required, STM can not be used for imaging non-conducting samples. In 1986, the atomic force microscope (AFM) was invented by Binning, Quate and Gerber.[2] The AFM can overcome this limit and be used for imaging conducting specimens, as well as non-conducting ones. AFM operates by measuring the atomic forces (either attractive or repulsive forces) between the probe and the surface. AFM has been an important and powerful technique for resolving nanoscale features, and thus has been utilized for various scientific, engineering, and biological applications.

1.2 Issues of the conventional AFM probe tip

The key component of AFM is the probe tip, as the resolution and reliability of AFM imaging is determined by its sharpness, shape and the nature of materials. Standard commercial probes made of silicon or silicon nitride have tips with a pyramid shape (shown in Figure 1.1), which do not allow easy access to narrow or deep structural features, and generally have a relatively blunt tip radius on the order of 10 nm.

There have been several techniques developed for making high-aspect-ratio probes with sharp tips for AFM applications, such as using focused ion beam etching on Si or metal tips,[3-5] focused electron beam deposited amorphous carbon tips,[6,7] and nanowire probes by field emission induced deposition.[8] However, these high-aspect-ratio probes are not durable and are easily damaged during scanning, which doesn't allow long time imaging. In addition, these fabrication methods have their own disadvantages. The methods based on focused ion beam etching, focused electron beam deposition or field emission induced deposition require a serial process and are only capable of making a single tip at a time, which is very time-consuming.

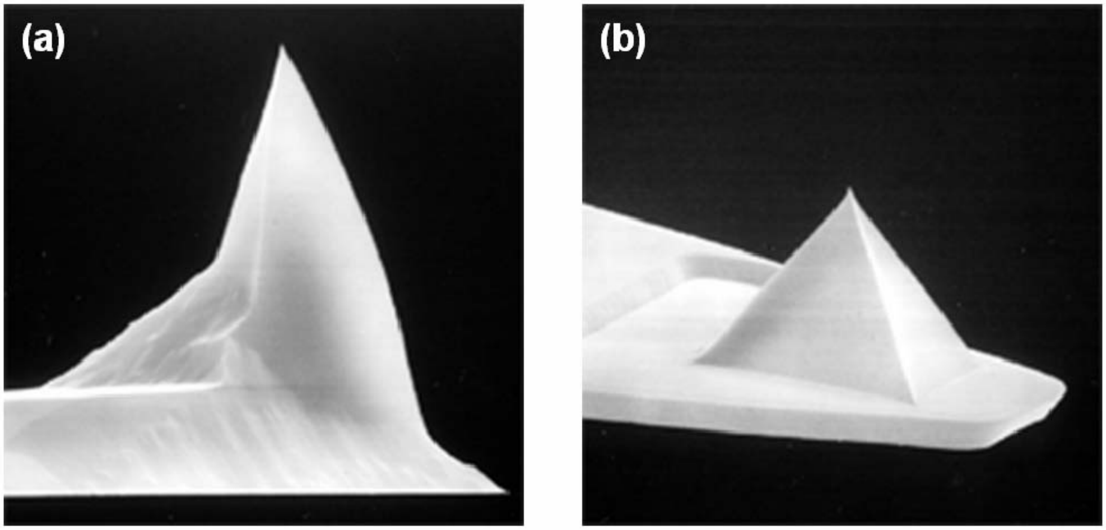

Figure 1.1 SEM images of (a) a Si AFM probe and (b) a silicon nitride AFM probe. (Veeco Probes)

1.3 Methods of making carbon nanotube AFM probes and their drawbacks

Due to its high aspect ratio geometry, small tip diameter and excellent mechanical properties, carbon nanotubes (CNTs) have become a promising candidate for new AFM probes to replace standard silicon or silicon nitride probes. CNT tips could offer high resolution images, while the length of CNT tips allows the tracing of steep and deep features.

However, there has been much less progress towards development of reliable processes for CNT AFM probes. CNTs have been attached on to pyramid tips by various approaches[9-13] as well as directly grown using thermal chemical vapor deposition (CVD).[14-16] The attachment methods are manual and time consuming, and often results in non-reproducible CNT configuration and placement. While thermal CVD approach can potentially lead to wafer scale production of AFM tips, the number, orientation and length of CNTs are difficult to control.

Recently, two approaches have been employed to fabricate multi-walled nanotube probes on tipless cantilevers by DC plasma enhanced CVD (DC-PECVD)[17,18] These approaches, however, require somewhat complicated, multiple patterning steps The catalyst dots in both approaches are patterned by lift-off of spin-coated polymethyl methacrylate (PMMA) layer following typical e-beam lithography. Reliable and uniform spin coating of a resist layer generally requires a relatively large area, and is difficult to achieve for a tipless cantilever which has a narrow and elongated geometry. In one of these reports,[17] patterned catalyst dots were formed before the fabrication of the cantilevers, but the catalyst had to be protected by PECVD-deposited Si_3N_4 layer in order for the catalyst dots to survive and preserve catalytic activity throughout the subsequent microfabrication steps. In the other report,[18] the e-beam lithography steps had to be used twice to pattern a catalyst dot on the commercial tipless cantilever in order to remove extra Ni catalyst on the cantilever. The probe tip radii reported are also relatively large.

An important aspect to consider in utilizing CNT probes is that the single-walled nanotube probes with a desirable small diameter tend to exhibit an inherent thermal vibration problem if the length is made reasonably long, and hence they can not be used to trace deep structural profiles. On the other hand, multi-walled nanotubes such as synthesized in DC-PECVD[19-22] have a larger diameter in the regime of 20–100 nm and hence exhibit improved mechanical and thermal stability, but the catalyst particle at the nanotube probe tip (or the natural dome structure in a nanotube grown by a base growth mechanism) has a finite radius of curvature which limits the AFM resolution.

1.4 Overview of thesis

In this work, the fabrication of a sharp and high-aspect-ratio conical carbon nanotube probe which possesses desirable thermal stability and mechanical toughness has been demonstrated by employing resist-free electron beam induced deposition (EBID) of carbon masks combined with electric-field-controlled CVD growth. A tunable CNT growth technique was also developed to control the plasma-induced surface stresses on cantilever beams during PECVD process. High resolution AFM imaging of nano-scale features and deep trenches was demonstrated using the fabricated probes. In addition, high coercivity iron-platinum coated CNT probes were fabricated and evaluated for magnetic force microscopy (MFM) application.

In chapter 2, a brief introduction of AFM is given, including its principles, instrumentations, commonly used operation modes and imaging artifacts from the tip convolution.

In chapter 3, section 3.1 gives a brief background on CNTs, including structures, properties, synthesis methods and applications. Section 3.2 presents the development of the EBID patterning technique for CNT probe fabrication. Section 3.3 shows geometry-controlled and direction-controlled growth of CNT probes on tipless cantilevers by PECVD.

Chapter 4 discusses how to control the surface stresses of cantilevers during PECVD growth of CNTs. Section 4.2 and 4.3 give a brief introduction and definition of plasma-induced stresses, and how the surface stresses cause the cantilever bending and thus affect the AFM measurements. Section 4.4 shows how the surface stresses of the cantilevers can be well-controlled by introducing hydrogen gas and adjusting the flow rate.

Chapter 5 contains all of the results and discussions of AFM and MFM imaging using conical CNT AFM probes. Section 5.2 demonstrates the tapping-mode imaging in air, as well as in liquid. Section 5.3 demonstrates the contact-mode images of soft materials and trench patterns. Section 5.4 shows durability test on CNT probes. Section 5.5 demonstrates the MFM images using magnetic film coated CNT probes and presents some analysis on the image quality and resolution.

Chapter 6 gives a conclusion of the main results in this study and discusses some ideas for future work.

1.5 References

[1] G. Binnig, H. Rohrer, Ch. Gerber. and E. Weibel, *Phys. Rev. Lett.* **49**, 57 (1982).

[2] G. Binnig, C. F. Quate and Ch. Gerber., *Phys. Rev. Lett.* **56**, 930 (1986).

[3] Vasile M J, Grigg D A, Griffith J E, Fitzgerald E A and Russell P E, *Rev. Sci. Instrum.* **62** 2167 (1991).

[4] Vasile M J, Grigg D A, Griffith J E, Fitzgerald E A and Russell P E, *J. Vac. Sci. Technol. B* **9** 3569 (1991).

[5] Vasile M J, Biddick C and Huggins H 1994 *Appl. Phys. Lett.* **64** 575 (1994).

[6] Akama Y, Nishimura E, Sakai A and Murakami H, *J. Vac. Sci and Technol. B* **8** 429 (1990).

[7] Wendel M, Lorenz H and Kotthaus J P, *Appl Phys. Lett.* **67** 3732 (1995).

[8] Tay A B H and Thong J T L, *Appl Phys. Lett.* **84** 5207 (2004).

[9] H. Dai, J. H., Hafner, A. G. Rinzler, D. T. Colbert, and R. E. Smalley, *Nature* **384**, 147 (1996).

[10] H. Nishijima, S. Kamo, S. Akita, Y. Nakayama, K.I. Hohmura, S.H. Yoshimura, K. Takeyasu, *Appl. Phys. Lett.* **74**, 4061 (1999).

[11] R. Stevens, C. Nguyen, A. Cassell, L. Delzeit, M. Meyyappan, and Jie Han, *Appl. Phys. Lett.* **77**, 3453 (2000).

[12] A. Hall, W. G. Matthews, R. Superfine, M. R. Falvo and S. Washburna, *Appl. Phys. Lett.* **82**, 2506 (2003).

[13] J. Tang, G. Yang, Q. Zhang, A. Parhat, B. Maynor, J. Liu, L.C. Qin and O. Zhou, *Nano Lett.* **5**, 11 (2005).

[14] J. H. Hafner, C. L. Cheung, and C. M. Lieber, *Nature* **398**, 761 (1999).

[15] C. L. Cheung, J. H. Hafner, T. W. Odom, K. Kim and C. M. Lieber, *Appl. Phys. Lett.* **76**, 3136 (2000).

[16] E. Yenilmez, Q. Wang, R. J. Chen, D. Wang and H. Dai, *Appl. Phys. Lett.* **80**, 2225 (2002).

[17] Q. Ye, A.M. Cassell, H.B. Liu, K.J. Chao, J. Han and M. Meyyappan, *Nano lett.* **4**, 1301 (2004).

[18] H. Cui, S. V. Kalinin, X. Yang, and D. H. Lowndes, *Nano lett.* **4**, 2157 (2004).

[19] V. I. Merkulov, A. V. Melechko, M. A. Guillorn, M. L. Simpson, D. H. Lowndes, J. H. Whealton, and R. J. Raridon, *Appl. Phys. Lett.* **80**, 4816 (2002).

[20] L.-H Chen, J. F. AuBuchon, A. Gapin, C. Daraio, P. Bandaru, S. Jin, D. W. Kim, I. K. Yoo and C. M. Wang, *Appl. Phys. Lett.* **85**, 5373 (2004).

[21] J. F. AuBuchon, L. H. Chen, A. I. Gapin, D. W. Kim, C. Daraio and S. Jin, *Nano lett.* **4**, 1781 (2004).

[22] M. Chhowalla, K. B. K. Teo, C. Ducati, N. L. Rupesinghe, G. A. J. Amaratunga, A. C. Ferrari, D. Roy, J. Robertson and W. I. Milne, *J. Appl. Phys.* **90**, 5308 (2001).

CHAPTER 2: FUNDAMENTALS OF ATOMIC FORCE MICROSCOPY

2.1 Instrumentation

Atomic force microscope (AFM) is a very powerful surface analysis tool which is capable of achieving high resolution of the three dimensional surface morphology of the sample. AFM was developed to overcome the drawback of scanning tunneling microscope (STM), which can only allow imaging conducting or semiconducting samples. The AFM, however, can be used not only to image conducting samples, but also non-conducting specimens, including polymers, ceramics, composites and biological samples.

The basic components of an AFM system are illustrated in Figure 2.1. The AFM consists of a micro-cantilever with a sharp probe at its end used to scan the surface of a sample, which motion is controlled by a piezoelectric scanner and a laser diode (LD)/position-sensitive detector (PSD) integrated part with a programmable software to read and feedback the voltage signals and. The cantilever is typically made by silicon or silicon nitride with a tip at the free-end. In some AFM systems, the piezoelectric scanner is used to control the motion of the probe instead of the sample stage. Besides, an optical microscope is essential for locating features on the sample surface and for monitoring the probe approach process. The AFM has to be placed on a vibration isolation table or unit since the scanning probe techniques require minimization of all sources of mechanical and electrical noise. If these types of noise are not well-controlled and reduced, the high resolution images are impossible to obtain.

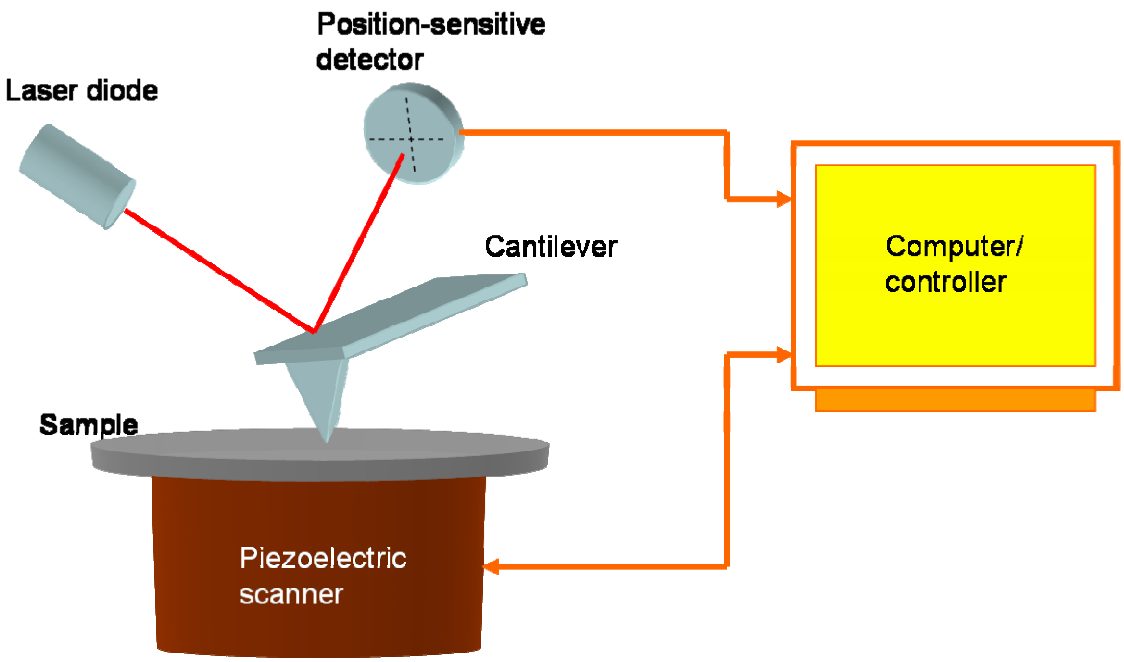

Figure 2.1 Schematic illustration of the typical components to make up an AFM system.

2.2 Principles of atomic force microscope

In an AFM operation, a constant force is maintained between the probe and sample while the probe is raster scanned across the surface. By monitoring the motion of the probe as it is scanned across the surface, a three dimensional image of the surface is constructed. The constant force is maintained by measuring the force by the optical lever technique and using a feedback control electronic circuit to control the position of the z piezoelectric ceramic.

Although the AFM can be operated without feedback control, however, if the tip were scanned at a constant height, there would be a risk that the tip would collide with the surface and cause damages on either sample surface or tip itself. Hence, in most cases a feedback control is employed to adjust the tip-to-sample distance to maintain a constant force between the probe and the sample. In the commercial AFM, the most commonly used feedback control is the optical lever technique, developed by Meyer and Amer,[1] where a laser is reflected from the backside of the AFM cantilever onto a PSD, as shown in Figure 2.1. The voltage output from the PSD is sent to the computer/controller, which converts the voltage value into a distance. Thus, the cantilever deflection can be monitored and controlled.

In Figure 2.1, the sample is mounted on a piezoelectric scanner, which dimensions can be changed by applying an electric field. A typical piezoelectric material will expand by about 1 nm per applied volt. The piezoelectric scanner can move the sample in the z direction for maintaining a constant force, and the x and y directions for scanning the sample. The resulting map of the xy area represents the topography of the sample.

Since the atomic force microscopy relies on the forces between the tip and sample, knowing how the forces change as the tip moves toward and away from the surface is important. Figure 2.2 shows a typical force vs. distance curve of the interaction between the probe tip and sample surface. The force is not measured directly, but calculated by measuring the deflection of the cantilever. When the tip is far away from the surface, the no forces act on the cantilever and no deflection occurs. As the probe tip is brought very close to the surface, it may jump into contact if it feels attractive force from the sample. Once the tip is in contact with the surface, cantilever deflection will increase as the cantilever is brought closer to the sample. If the deflection of the cantilever is sufficiently large, the cantilever will deflect away from the surface and feels repulsive force.

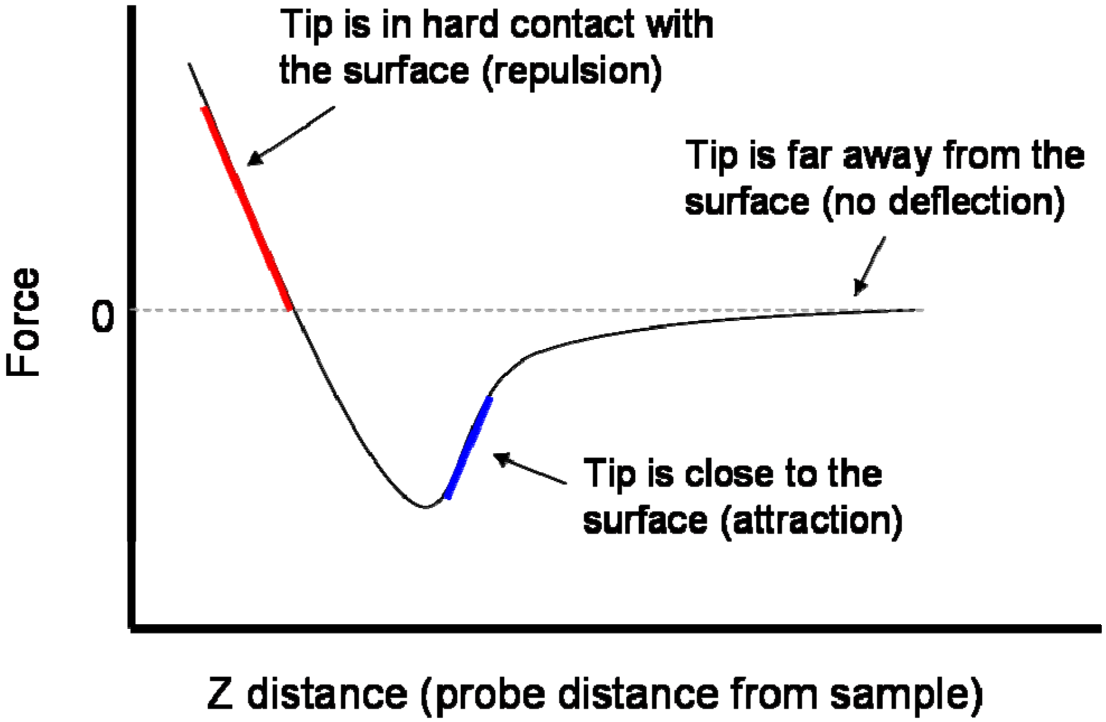

Figure 2.2 Force vs. distance curve of the interaction between the probe tip and sample surface.

2.3 Operating modes of atomic force microscope

The AFM can be operated in different modes, depending on the application. The three commonly used imaging modes are contact (also called static) mode, tapping (also called dynamic or intermittent-contact) mode and non-contact mode.

2.3.1 Contact mode

Contact mode is commonly used in AFM imaging, which is operated in the repulsive regime. As the tip is raster-scanned across the surface, it is deflected as it moves over the surface features. During contact-mode imaging, the tip is constantly adjusted to maintain a constant deflection, and therefore constant height above the surface. It is this adjustment that is displayed as data. However, the ability to track the surface in this manner is limited by the feedback circuit. Because the tip is in hard contact with the surface, the stiffness of the cantilever needs to be less that the effective force constant holding atoms together, which is on the order of 1-10 N/m. Most contact mode levers have a force constant of < 1N/m.

2.3.2 Tapping mode

When operated in air, the cantilever is oscillated at its resonant frequency and part of the oscillation extends into the repulsive regime, so that the tip intermittently touches the surface for a very small fraction of its oscillation period. High stiffness cantilevers with force constant on the order of 15-50 N/m are typically used. The advantage of tapping the surface is improved lateral resolution on soft samples. Lateral forces such as meniscus force, common in contact mode, are virtually eliminated.

2.3.3 Non-contact mode

In non-contact mode operation, a stiff cantilever is oscillated above the surface of the sample in the attractive regime, which means that the tip is very close to the surface, but not touching it. The forces between the tip and sample are quite low ($\sim 10^{-12}$

N). The detection scheme is based on measuring changes to the resonant frequency or amplitude of the cantilever. Non-contact mode is very difficult to operate in ambient conditions with the AFM.

2.4 References

[1] G. Meyer and N. M., H. Amer, *Appl. Phys. Lett.* **53**, 2400 (1988).

CHAPTER 3: FABRICATION OF CARBON NANOTUBE BASED PROBES

3.1 Introduction of carbon nanotubes

Until the mid-1980 only two forms of pure solid carbon were thought to exist: diamond and graphite. In 1985, a brand-new carbon molecule, Buckminsterfullerene C_{60}, was discovered by Harold W. Kroto, Richard E. Smalley and Robert F. Curl. Afterwards, other related molecules composed of only carbon atoms were also revealed. These carbon molecules were recognized as a new class of carbon allotropes, called the Fullerenes.

Carbon nanotubes (CNTs), which were discovered in 1991 as elongated Fullerenes are composed of graphene sheets that are rolled up into tubes. Since the discovery, CNTs have been considered to have many potential applications in various science and engineering fields because of their unique physical and chemical properties. Although most academic and popular literatures attribute the discovery CNTs to Sumio Iijima of NEC, a 2006 editorial written by Marc Monthioux and Vladimir Kuznetsov in the journal *Carbon* has described the interesting and often misstated origin of CNTs: In 1952's Russian *Journal of Physical Chemistry*, L.V. Radushkevich and V.M. Lukyanovich published Transmission Electron Microscopy (TEM) images of 50 nm diameter tubes made of carbon. It is likely that carbon nanotubes were produced before this date.

3.1.1 Structures of carbon nanotubes

The structure of CNTs has been explored by high resolution TEM and Scanning Tunneling Microscopy (STM) techniques,[5] yielding direct confirmation that the CNTs are seamless cylinders formed by the honeycomb lattice of a single layer of crystalline graphite, called a graphene sheet. In general, CNTs are divided into two types, single-walled nanotubes (SWNTs) and multi-walled nanotubes (MWNTs), as shown in Figure 3.1. SWNTs were discovered experimentally by Iijima et al. at the NEC Laboratory[6] and by Bethune and coworkers at the IBM Almaden laboratory in 1993,[6,7] two years after the discovery of MWNTs.[2] A SWNT is composed of only one grapheme sheet rolled up to form a cylindrical and seamless tube while a MWNT consists of a number of concentric tubes.

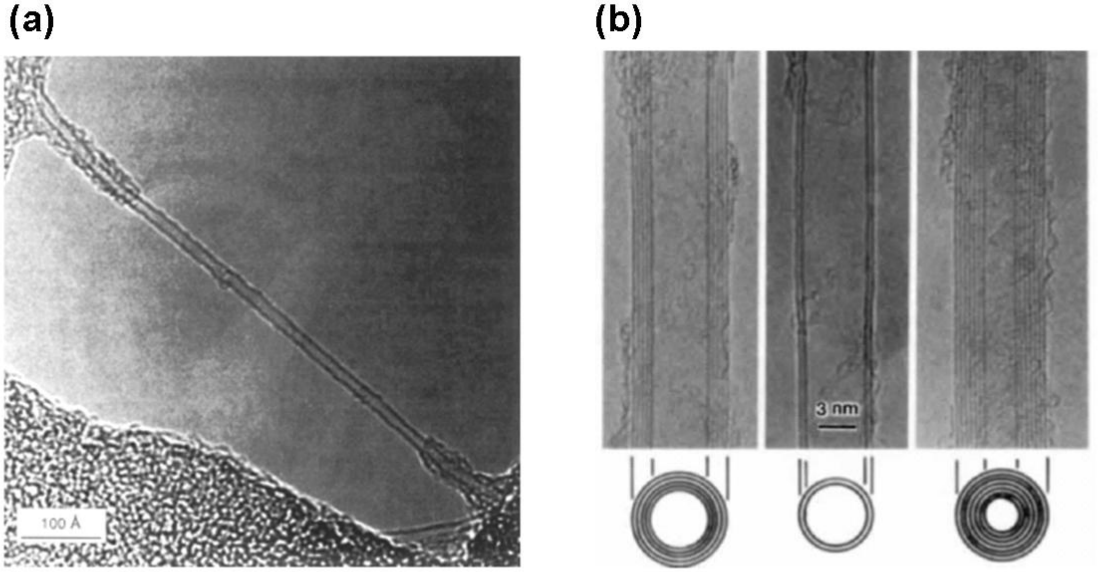

Figure 3.1 The observation of SWNTs and MWNTs by TEM. (a) TEM image of SWNTs reported by D. S. Bethune et al.[6] (b) TEM image of MWNTs reported by S. Iijima.[2]

By rolling a graphene sheet in different directions, different types of nanotubes can be formed. The graphene lattice structure can be described with the basis vectors of the graphene net, $\mathbf{a_1}$ and $\mathbf{a_2}$ (Figure 3.2). A SWNT can be characterized by a chiral vector $\mathbf{C} = n\mathbf{a_1} + m\mathbf{a_2}$ in terms of a set of two integers (n,m) corresponding to the basis vectors, as shown on Figure 3.2.[8] The chiral angle θ is defined as the angle between the chiral vector **C** and $\mathbf{a_1}$ direction ($m = 0$). Based on the chiral vector and angle, three different types of nanotubes can be generated by rolling up the graphene sheet into a cylinder: The tubes with $m = 0$ ($\theta = 0^\circ$) are commonly referred to as zigzag nanotubes and $n = m$ ($\theta = 30^\circ$) as armchair nanotubes. Other nanotubes corresponding to $0^\circ < \theta < 30^\circ$ are called (n,m) chiral nanotubes.

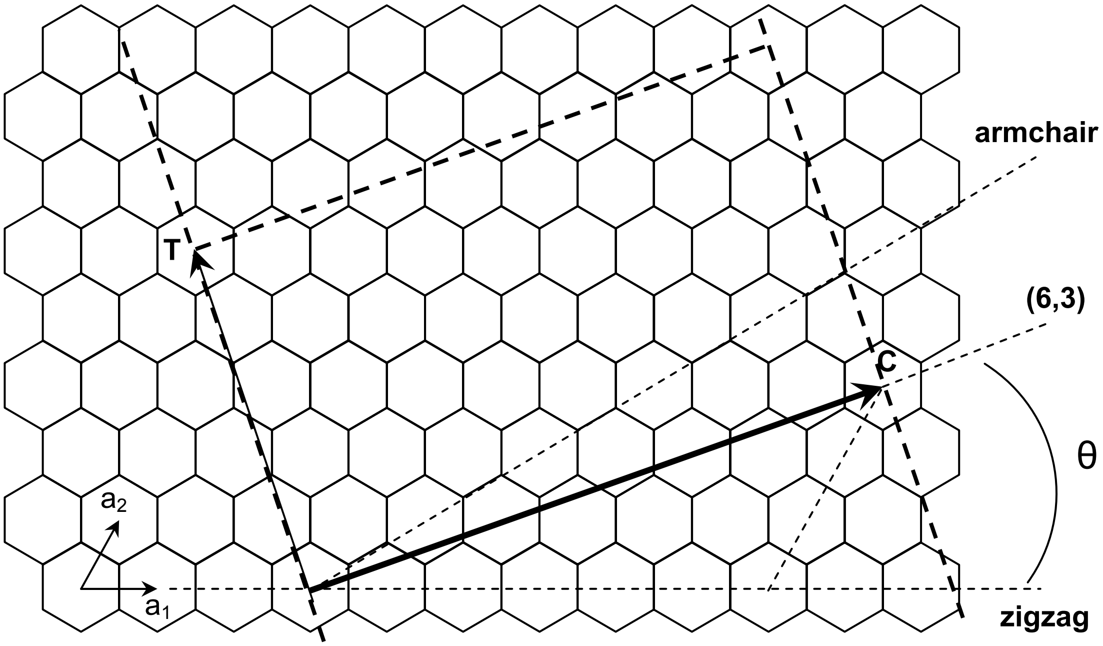

Figure 3.2 The chiral vector $\mathbf{C} = n\mathbf{a_1} + m\mathbf{a_2}$ is defined on the honeycomb lattice of a graphene sheet by unit vectors, $\mathbf{a_1}$ and $\mathbf{a_2}$ and the chiral angle with respect to the $\mathbf{a_1}$ axis, i.e. zigzag axis ($\theta = 0^\circ$). The armchair axis is 30° off from the zigzag axis. A nanotube (6,3) is formed by rolling the graphene sheet along the chiral vector **C**. Also shown the lattice vector **T** of the nanotube unit cell.

The ideal MWNTs have concentric cylindrical layers formed by rolled-up graphene sheets, as shown in Figure 3.3(a). The walls of each layer of the MWNT are parallel to the central axis ($\alpha = 0$, α is defined as an angle between the tube axis and the graphene sheet surface). In this work, The CNTs were all grown by DC-PECVD process which always produces CNTs with the stacked cone structure (as known as the herringbone or bamboo-like structures, shown in Figure 3.3b) instead of perfect tube-shaped CNTs. Figure 3.4(a) and (b) show TEM images of perfectly tube-like CNTs and herringbon-like ones. Both bamboo and herringbone-like CNTs are sometimes called carbon nanofibers (CNFs) since they are not made of perfect graphene tubes. In this dissertation, although some authors might claim otherwise, we prefer to use the term CNT to describe them.

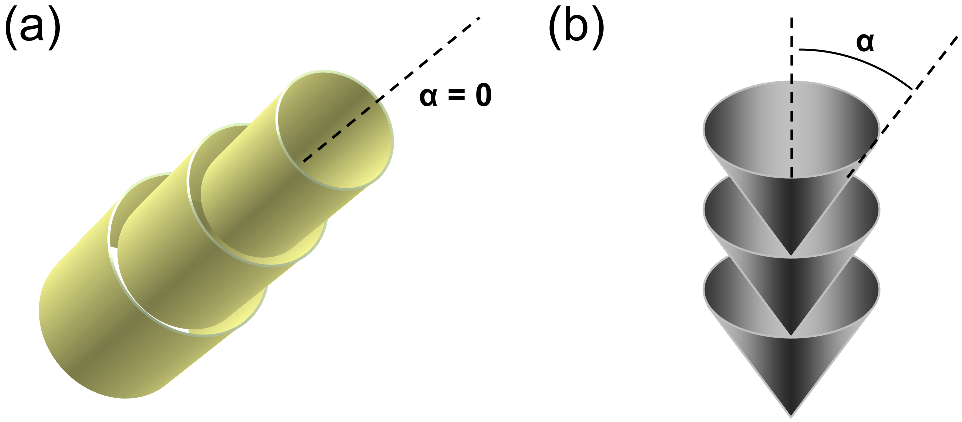

Figure 3.3 Schematic structures of (a) tube-like carbon nanotubes and (b) stacked cone nanotubes.

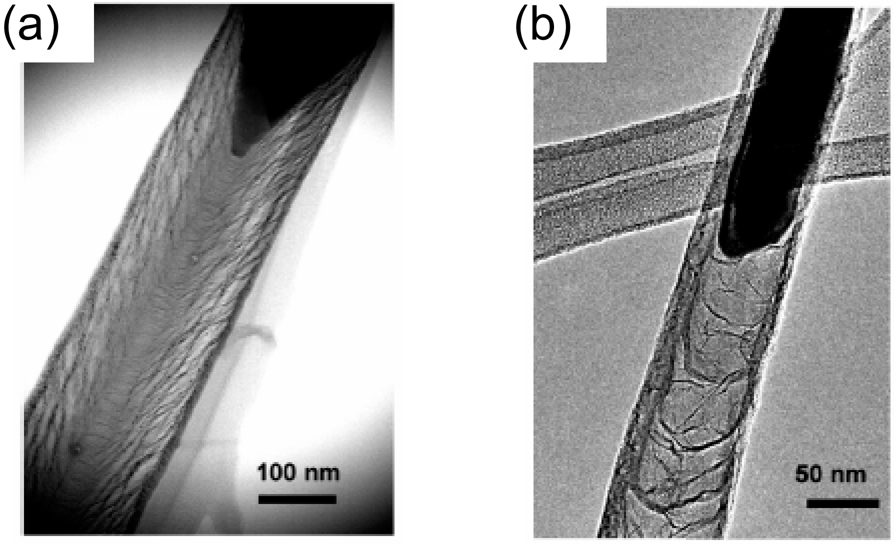

Figure 3.4 (a) TEM image of a herringbone-like carbon nanotube. (b) TEM image of a bamboo-like carbon nanotube.[9]

3.1.2 Properties of carbon nanotubes

CNTs have remarkable mechanical properties because of the strong σ bonding (carbon-carbon bonds) of the graphene sheet and, they also possess excellent electronic properties and other unique characteristics. From the previous section, we know that CNTs have many different types of structures and geometries (such as the chiral angle and diameter) which may lead to various and interesting properties. For these reasons, CNTs have attracted much academic research interest to explore these properties and develop CNT-based devices.

Electronic properties of CNTs have received a lot of attention in the past few years.[10,11] Their extremely small size and high-aspect-ratio geometry offer a great model for studying one dimensional quantum effects. Both theoretical calculations[12,13] and experimental results[14-19] have shown that CNTs possess various interesting and excellent electronic properties.

The mechanical properties of CNTs have also been studied experimentally and theoretically. Most theoretical calculations are carried out for CNTs with defect-free structures.[20,21] Table 3.1 shows the mechanical properties of carbon-based materials. From the calculations, CNTs are predicted to have exceptional mechanical properties, particularly high stiffness and axial strength, as a result of their seamless graphitic structure. The Young's modulus of perfect SWNTs is ~ 1 TPa, which is comparable to that of the diamond, the material with the highest stiffness.[20] The calculation is in agreement with experiments on average.[22,23]

Table 3.1 Mechanical properties of carbon-based materials

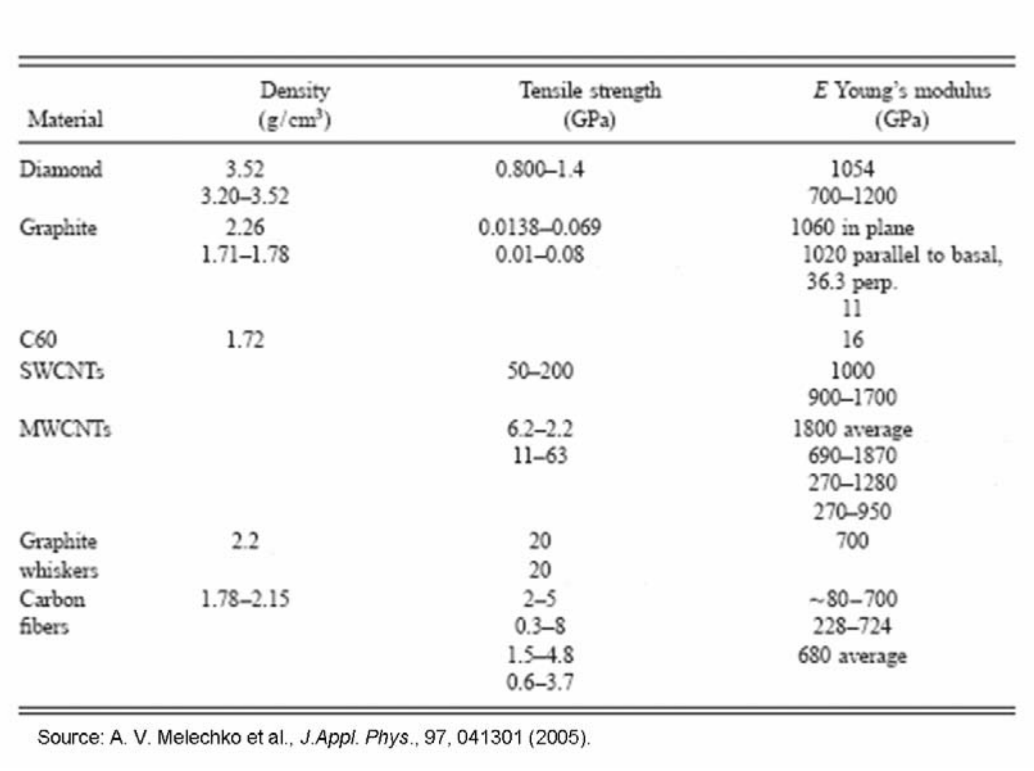

Material	Density (g/cm^3)	Tensile strength (GPa)	E Young's modulus (GPa)
Diamond	3.52	0.800–1.4	1054
	3.20–3.52		700–1200
Graphite	2.26	0.0138–0.069	1060 in plane
	1.71–1.78	0.01–0.08	1020 parallel to basal, 36.3 perp.
			11
C60	1.72		16
SWCNTs		50–200	1000
			900–1700
MWCNTs		6.2–2.2	1800 average
		11–63	690–1870
			270–1280
			270–950
Graphite whiskers	2.2	20	700
		20	
Carbon fibers	1.78–2.15	2–5	~80–700
		0.3–8	228–724
		1.5–4.8	680 average
		0.6–3.7	

Source: A. V. Melechko et al., *J.Appl. Phys.*, 97, 041301 (2005).

SWNTs are also the strongest known material with a specific tensile strength as high as 100 times that of steel.[24]. Theoretically, the Young's modulus of MWNTs takes the highest value of a SWNT plus contributions from coaxial intertube coupling. Thus, the Young's modulus for MWNT is higher than a SWNT.[25] Experimentally, however, the mechanical properties of MWNTs are not as good as those for SWNTs due to the difficulties of making them defect free.

3.1.3 Synthesis methods of carbon nanotubes

There are various growth methods for carbon nanotubes, such as arc discharge,[2,26] laser ablation,[1,7] thermal chemical vapor deposition (TCVD),[27-29] and plasma enhanced chemical vapor deposition (PECVD).[30-32] While arc discharge and laser ablation are very efficient methods for producing high-quality nanotubes in large quantities, the by-products, including fullerenes, graphitic polyhedrons and amorphous carbon, are always created during the processes. Thus, complex purification procedures for obtaining CNT materials are required.[33] Also, these methods do not offer good control over the spatial arrangement of the produced CNTs.

Recently, CVD methods have been widely used to grow CNTs because it allows controlled synthesis of CNTs with selected catalyst patterns. While TCVD approaches can potentially lead to wafer scale production of CNTs, only PECVD can offer good control of the number, orientation and length of CNTs during synthesis. Due to its highly controllable process, PECVD is the best way for growth of CNT AFM probes (See Ref. 34 for a review of PECVD growth of CNTs).

3.1.4 CVD growth mechanism of carbon nanotubes

The CVD based growth process involves heating a catalyst material on a substrate to high temperatures in a chamber and flowing a hydrocarbon gas through the chamber for a period of time. The main difference between TCVD and PECVD process is that in TCVD thermal energy is used to activate the hydrocarbon gas, whereas in PECVD the molecules are activated by electron impact. The gas activation takes place in nonequilibrium plasma, generally referred to as a glow discharge. The catalyst materials are usually transition-metal nanoparticles spread or patterned on a sample surface.

There are two different growth modes that have been observed for the catalytic growth of CNTs. In base growth mode, shown in Figure 3.5(a), the catalyst particle adheres to the substrate while the CNT is grown up above it. In tip growth mode, the catalyst particle stays on the top end of the nanotube where the CNT growth occurs, as illustrated in Figure 3.5(b). Tip growth mode is better for fabricating long CNTs because carbon vapor species interact more efficiently with the catalysts. It has been proposed that the growth mode depends on the interaction of the catalyst with its support.[35]

Figure 3.6 shows a schematic illustration of the growth mechanism of CNTs by CVD. Tip growth mode was used as an example, which is mostly observed in the PECVD process. The general nanotube growth model, called the vapor-liquid-solid (VLS) model, involves absorption and decomposition of hydrocarbon molecules at the surface of the metal catalyst particle, and dissolution and saturation of carbon atoms in the catalyst particle. Carbon atoms from decomposition of hydrocarbon molecules diffuse through the bulk of the catalyst particle or along the surface of the catalyst particle. After the catalyst particle becomes supersaturated with carbon, the precipitation of carbon from the catalyst particle results in the formation of graphene planes. The catalyst particle shape and inclined planes shown here are typical of those observed when Ni is used as the catalyst particle in a DC-PECVD process.

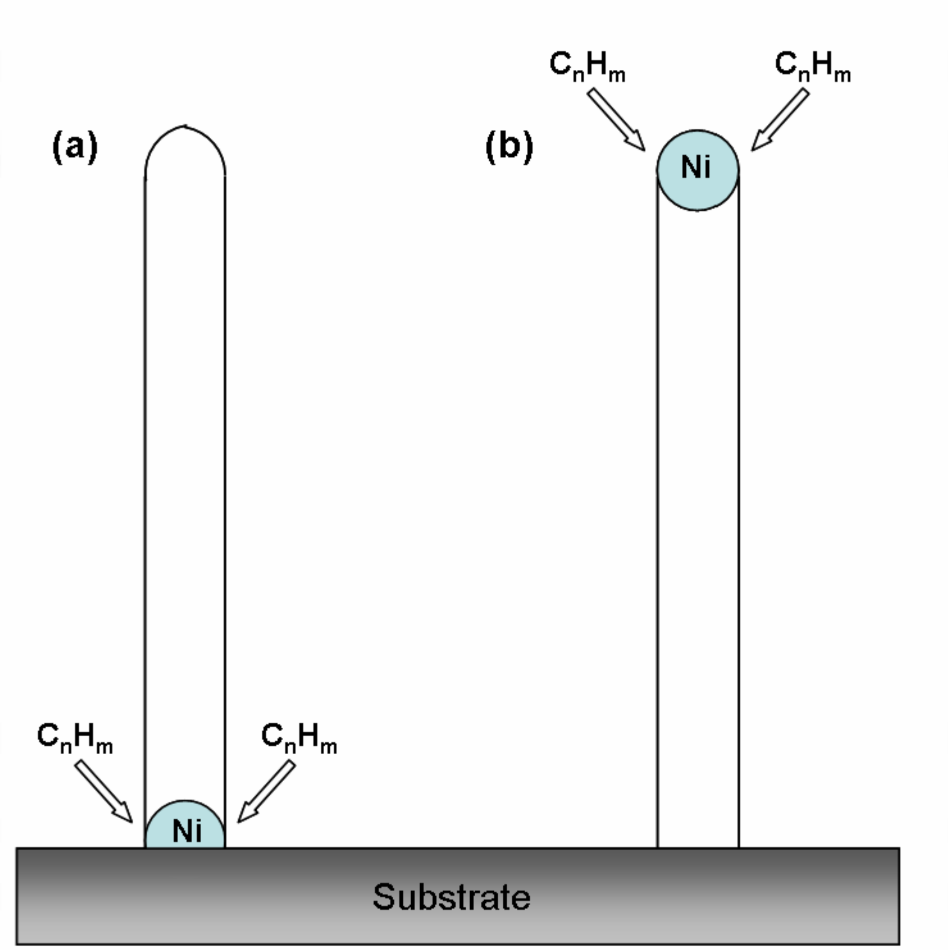

Figure 3.5 Two general growth modes of nanotubes by chemical vapor deposition process. (a) Base growth mode. (b) Tip growth mode.

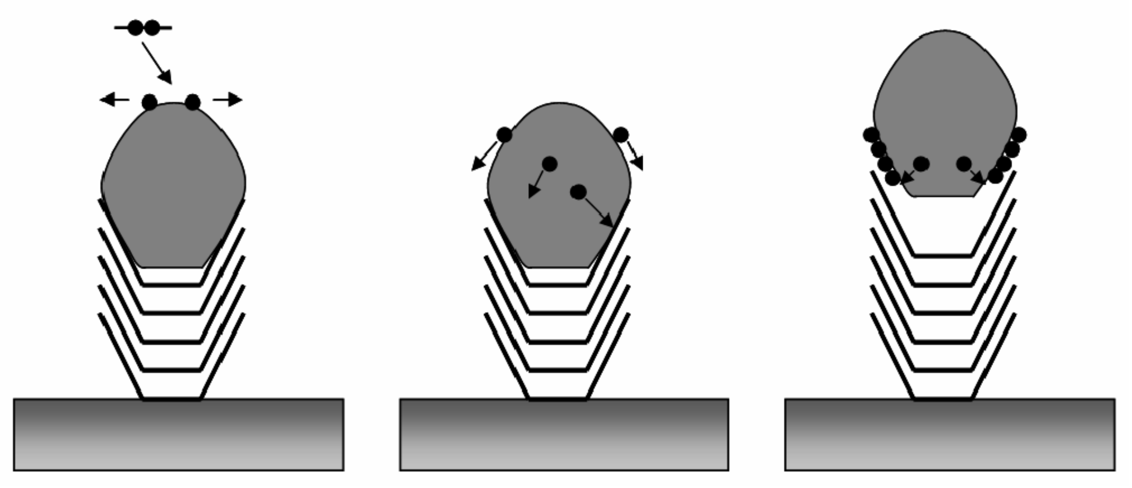

Figure 3.6 Schematics of the growth mechanism of carbon nanotubes. (a) Adsorption and decomposition of the reactant hydrocarbon molecule on the surface of catalyst, (b) dissolution and diffusion of carbon species through or around the metal particle, and (c) precipitation of carbon from the catalyst particle and formation of graphene layers.

3.1.5 Applications of carbon nanotubes

Carbon nanotubes have extraordinary electrical conductivity, heat conductivity and mechanical properties. Since their discovery, several demonstrations have suggested potential applications for nanotubes, such as electron field emitters for vacuum microelectronic devices,[36,37] nanoprobes for SPM imaging,[38] field effect transistors,[39,40] chemical sensors[41] and transparent electrodes for organic solar cells.[42] Recently, aligned CNT arrays have been studied in IC packaging as electrical interconnections,[43] as well as thermal interface materials to take heat off the IC chips.[44] Due to their high electrical and thermal conductivities, CNTs seem to be very promising for these applications. Some of the above applications could become marketable, while most still require further modification and optimization.

3.2 Fabrication procedures of carbon nanotube probes

The fabrication process used in this sutdy is schematically illustrated in Figrue 3.7. First, the top surface of the cantilever (NSC/tipless, MikroMasch USA) was coated with ~10 nm thick Ni film by e-beam evaporation. For EBID of carbon dots, a JEOL IC845 scanning electron microscope (SEM) with the NPGS software (J. C. Nabity lithography system) was used. The acceleration voltage was 30 kV, and the beam current was 50 pA. The carbon dot deposition time was varied between 8 to 30 s depending on the intended size of the dot. No special carbonaceous precursor molecules were introduced as the residual carbon-containing molecules naturally presenting in the chamber was sufficient for EBID processing to form amorphous carbon dots on the cantilever surface. A single carbon dot with a selected diameter of ~400 nm was deposited near the front end edge of the cantilever by EBID as illustrated in Figure 3.7(b). The carbon dot serves as a convenient etch mask for chemical etching. The Ni film was then etched away by using a mixture of $[H_3PO_4]:[HNO_3]:[CH_3COOH]:[H_2O] = 1:1:1:2$ except the portion underneath the mask. The removal of carbon dot mask after the catalyst patterning was performed with oxygen reactive ion etch (RIE) for 1 min, which exposed the Ni island as illustrated in Figure 3.7(c). The cantilever with the Ni island was then transferred to the DC-PECVD system for subsequent growth of the CNT, Figure 3.7(d). The growth of the CNT probe was carried out at 700˚C for 10-20 min using a mixture of NH_3 and C_2H_2 gas (ratio 4:1) at 3 mtorr pressure. An applied electric field was utilized to guide the growth of the nanotube along the desired direction. In this fabrication technique, catalyst patterning and PECVD growth of CNTs are the key procedures, which will be discussed in the following sections.

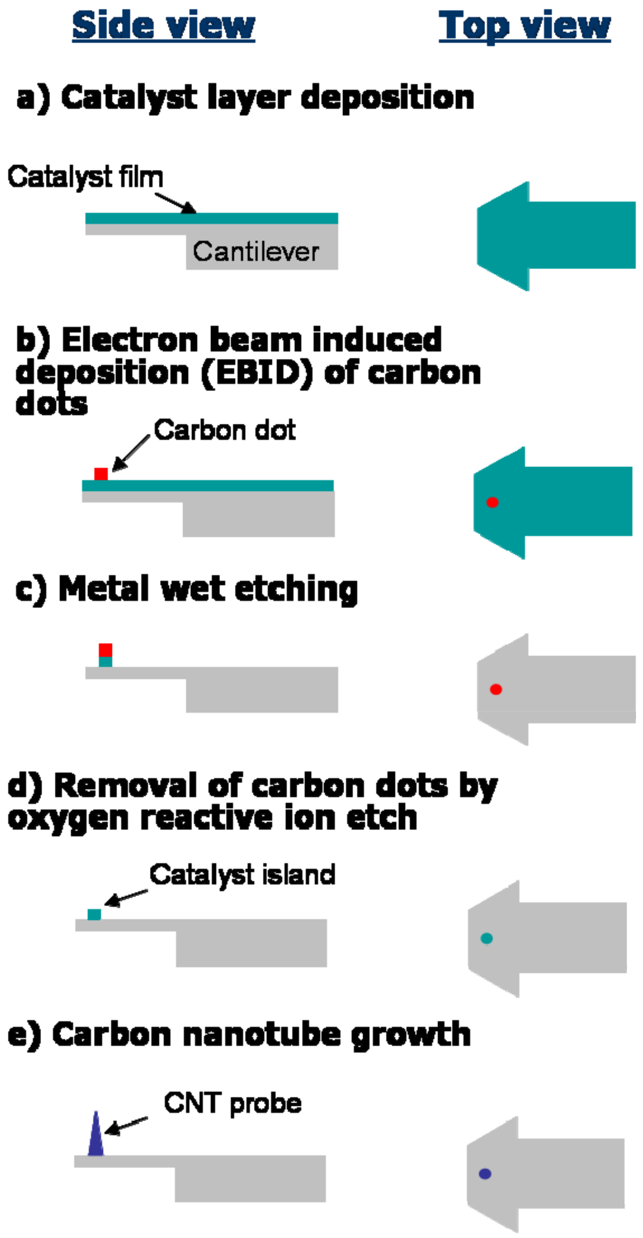

Figure 3.7 Schematic illustration of the resist-free fabrication technique for a single CNT based AFM probe. (a) Catalyst deposition by e-beam evaporation. (b) E-beam induced deposition of a carbon dot mask. (c) Metal wet etching and removal of carbon dot. (d) PECVD growth of a CNT probe.

3.3 Catalyst pattering on cantilevers

3.3.1 Disadvantages of conventional lithographic techniques

One of the key processes for CVD-grown CNT probe fabrication is catalyst patterning which decides the position, number and diameter of the probe. Electrophoretically deposited[45] or spin coated[46] colloidal catalyst particles on Si pyramid tips can not provide a reliable control on the position and number of catalyst particles.

Recently, two approaches have been reported to fabricate multiwall nanotube probes on tipless cantilevers.[47,48] The catalyst pattering in both approaches were preceded by typical e-beam lithography and lift-off of spin-coated polymethyl methacrylate (PMMA) layer. However, uniform spin coating of a PMMA or resist layer requires a relatively large and planar surface because step coverage of the resist is poor on the highly elevated or deeply etched structures. Therefore, a spin coated PMMA layer can not be uniformly conformal on the relatively small piece of tipless cantilever or on the Si pyramid tip. In one of these reports,[47] patterned catalyst dots were formed before the fabrication of the cantilevers, but the catalyst had to be protected by PECVD-deposited Si_3N_4 layer in order for the catalyst dots to survive and keep catalytic activity throughout the subsequent microfabrication steps. In the other report,[48] the e-beam lithography steps had to be used twice to pattern a single catalyst dot on the tipless cantilever in order to remove extra Ni catalyst on the cantilever.

3.3.2 Electron beam induced deposition (EBID)

Due to the limitation of the conventional resist coating technique, in this study, a simple and novel electron beam induced deposition (EBID) technique was introduced and developed for catalyst pattering on the end of the cantilever. EBID is commonly observed during electron microscope examination. The earliest observation was reported by Watson in 1947 who found that carbon black particles appeared to increase in size on electron microscope specimens under electron bombardent.[49] Similar phenomena were observed and reported by other researchers, and the sources of specimen contamination were investigated.[50-54]

The contamination was believed to be the result of interaction between the electron beam and organic molecules adsorbed on the bombarded surface. Several models were proposed to explain this phenomenon.[52,55] Early research work on EBID focused on reducing its effect in contaminating the sample surface during electron microscopy studies. Later, EBID was used to make insulating thin films,[56] repair photomasks,[57] and construct three-dimensional nanoscale structures.[58,59]

The principle of EBID is illustrated in Figure 3.8. In a high vacuum condition, there are still some residual organic or hydrocarbon molecules inside the chamber, which are adsorbed on the substrate surface. When an electron beam is focused on the substrate surface, the hydrocarbon molecules adsorbed in and near to the irradiated area dissociate into the nonvolatile deposit (mostly composed of amorphous carbon) and volatile fragments as a result of complex e-beam-induced surface reactions. Different precursor gas molecules, such as organometallic compounds, can be introduced into the chamber for making patterns of metallic deposits.

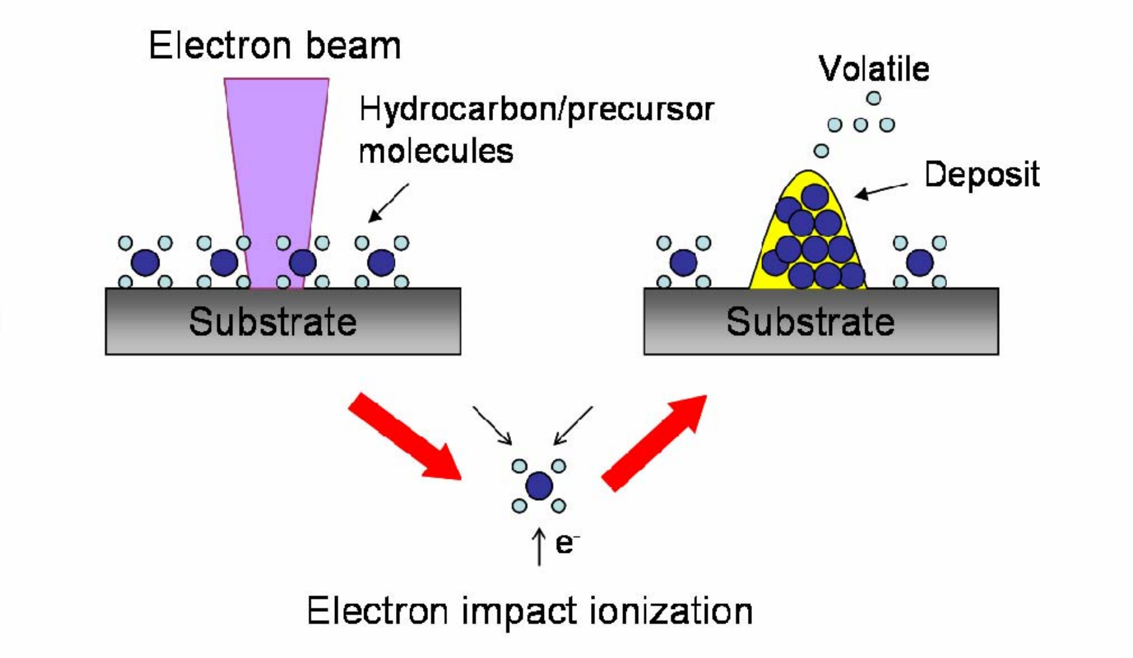

Figure 3.8 Schematic illustration of the EBID process. The residual hydrocarbon gas or an intentionally supplied precursor gas is continuously absorbed to the substrate. An electron beam is focused on the substrate. The electrons are dissociating the adsorbed molecules and a deposit is formed on the substrate. The volatile components are evacuated from the deposition chamber.

3.3.3 Catalyst islands made by EBID process

EBID is a simple and fast technique to make patterns and deposit materials simultaneously without using any e-beam resist. Its resist-free characteristic makes EBID a good choice for fabrication of patterns on the edge of the substrate, at the top of the terrace, or inside the trench. Broers et al. were the first to use EBID patterns as a dry etching mask to fabricate metal lines.[60] In this study, carbon dot made by EBID was used for catalyst patterning as a wet-etching mask.

Figure 3.9(a) shows a carbon dot of 400 nm deposited on the tipless cantilever by EBID. While the use of EBID carbon patterns have been demonstrated as dry etching masks,[60] there has been no report for their use as wet etching masks to the best of our knowledge. Thus, the chemical etchability of the carbon dots was investigated in various acids and other chemicals such as HCl, HF, HNO_3, H_2O_2 and acetone, and it is shown that the carbon dots are very stable and remained adherent on the substrate after immersing into these chemicals.

The carbon dots have a unique advantage in that while they are resistant to chemical etching, they are easily removable by oxygen RIE. Also, I found that the oxygen RIE process does not affect the Ni film and reduce its catalytic activity for CNT nucleation and growth. Figure 3.9(b) shows the Ni catalyst dot on the tipless cantilever after wet etching and removal of the carbon dot.

The diameter of the Ni dot can be additionally controlled by adjustment of the wet etch time due to the sidewall etch. As shown in Figure 3.9(b), a Ni dot of 300-nm-diameter can be obtained with a carbon mask of 400-nm-diameter after wet etching process. In general, the sidewall etch rate is much slower than the normal etch rate. The periphery of the Ni dot is somewhat non-regular, but it will not affect CNT growth because the Ni dot will shrink and become a more or less circular Ni island after heating up to 700 ˚C.

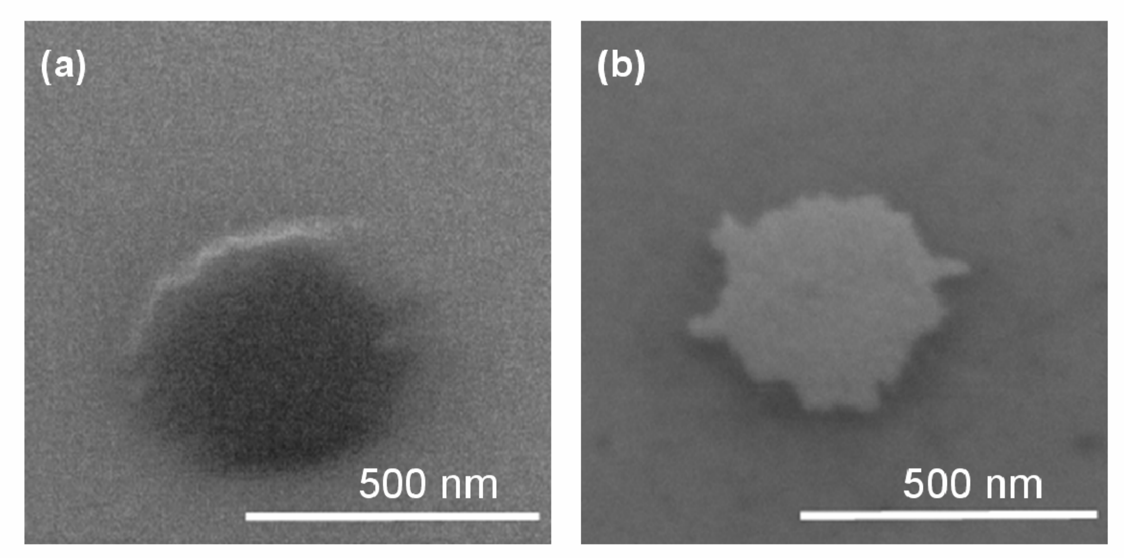

Figure 3.9 (a) SEM image of a 400 nm EBID carbon dot on the tipless cantilever. (b) SEM image of a 300 nm Ni island on the tipless cantilever after wet etching and removal of carbon dot.

3.4 Growth of CNT based AFM probes by DC-PECVD

In this work, a homemade DC-PECVD system was used for growth of CNT probes on AFM cantilever beams. In PECVD, the impact from ions and especially electrons activates the molecules in the feed gas. The presence of the plasma reduces the activation energy for the growth of CNTs and allows for the deposition to take place at lower temperatures than those required for thermal CVD.

A schematic illustration of the DC-PECVD process for CNT growth is shown in Figure 3.10. The cantilever with an EBID patterned catalyst dot is placed on the cathode which is heated by a heater underneath. An anode is placed above the cathode and sample. With a controlled supply of feed gas with a certain flow ratio, a negative bias is applied to the cathode and with the right combination of pressure, temperature, and applied bias, a dc glow discharge can occur, and a plasma sheath will form over the substrate. Within this sheath, a strong electric field is formed and its direction is perpendicular to the top surface of the cathode, which can be utilized to grow vertically aligned CNTs.

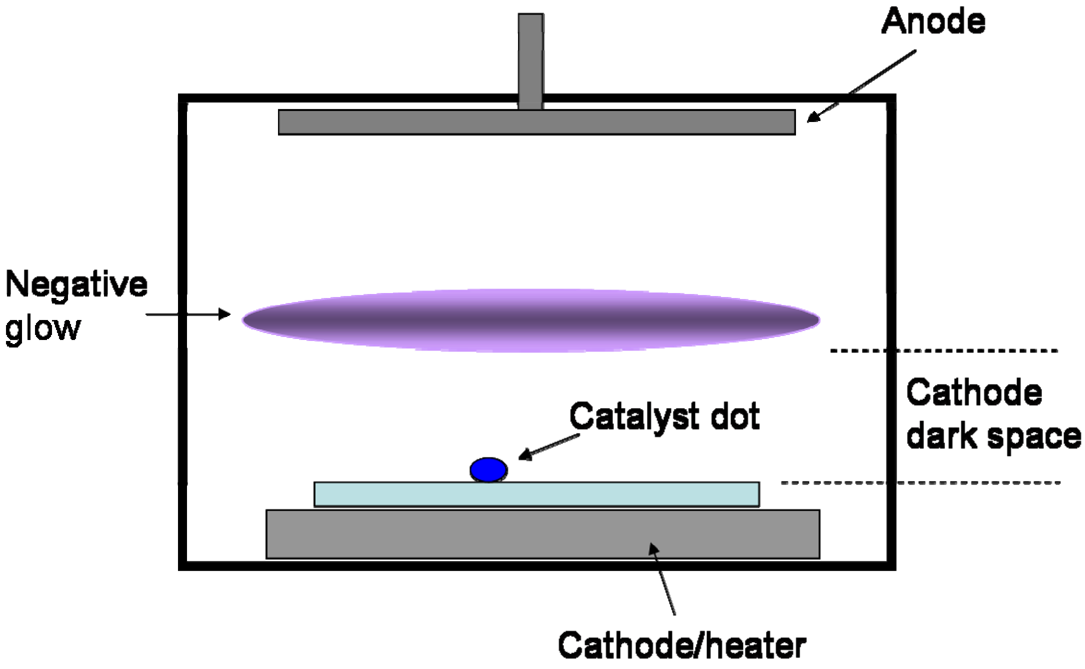

Figure 3.10 Schematic illustration of the DC-PECVD process for CNT growth.

3.4.1 Growth of a single carbon nanotube

In order to grow a single CNT probe, the diameter and thickness of an EBID defined catalyst dot has to be optimized. In this study, the thickness of Ni catalyst film was fixed at 10 nm. Thus, the size of patterned catalyst dot is crucial in determining if single or multiple nanotubes form. Figure 3.10 shows SEM images of growth of CNTs from EBID patterned catalyst dots with various sizes. As shown in Figure 3.10(c), a single CNT can be grown with a catalyst dot of 250 nm in diameter.

Previous experimental studies on CNT growth indicate that the diameter of the 10 nm thick Ni catalyst island should be kept smaller than ~300 nm to avoid the undesirable nucleation and growth of multiple CNTs.

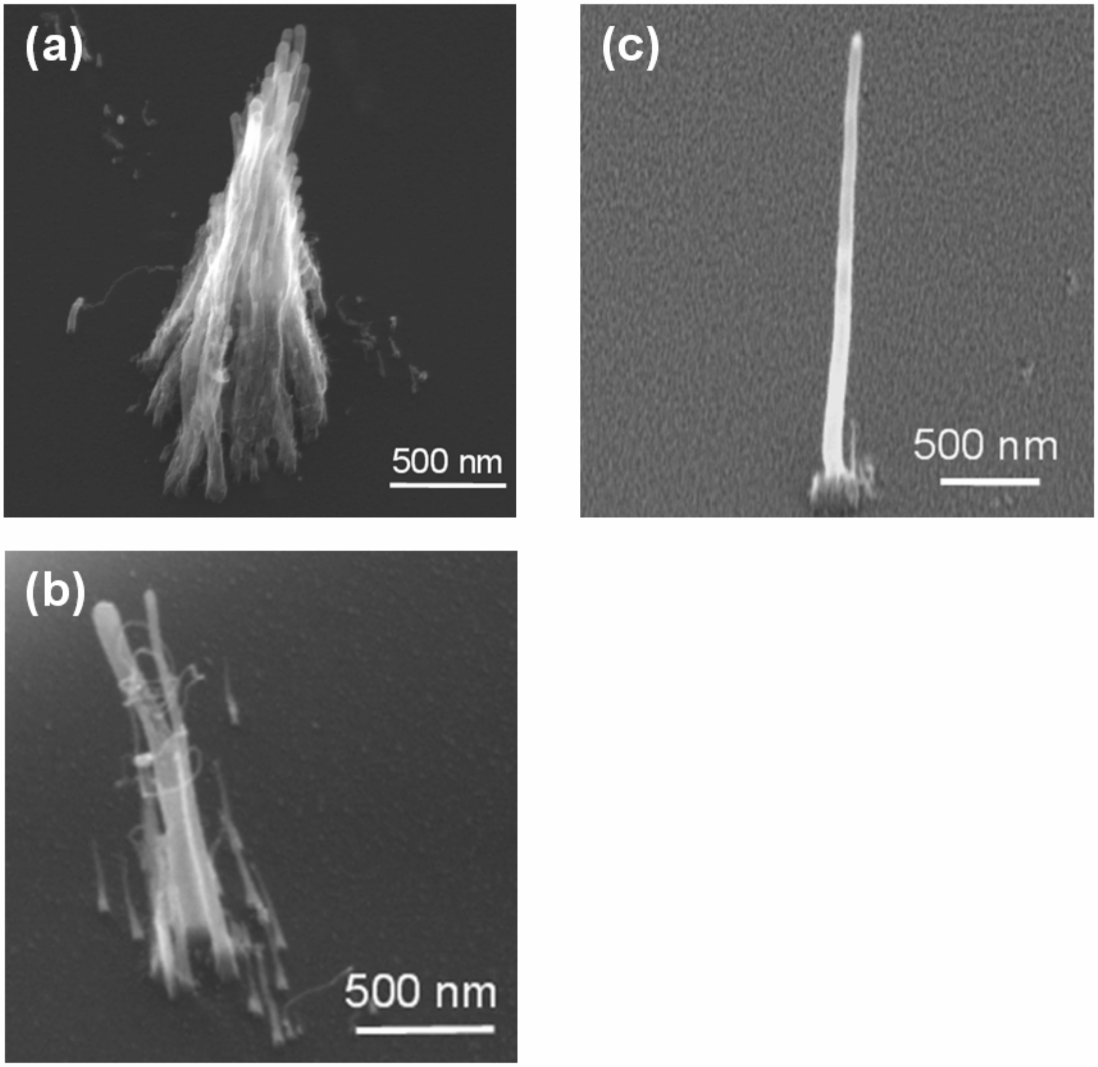

Figure 3.11 Growth of CNTs from the circular catalyst pattern with the diameter of (a) 750 nm, (b) 500 nm and (c) 250 nm.

Transmission electron microscopy was performed on a JEOL 3010 transmission electron microscope (TEM) operated at 300 kV. TEM images of CNTs grown using DC-PECVD with 450 V dc bias are shown in Figure 3.12. Figure 3.12(a) shows the equi-diameter CNTs with Ni catalyst particles on top of them. It can be seen that there is a thin amorphous carbon layer covered the surface of catalyst particles and CNTs after growth. Figure 3.12(b) is a high resolution TEM image to show the detailed structure of CNTs. It is clearly shown that our PECVD-grown CNTs possess the bamboo-like structure.

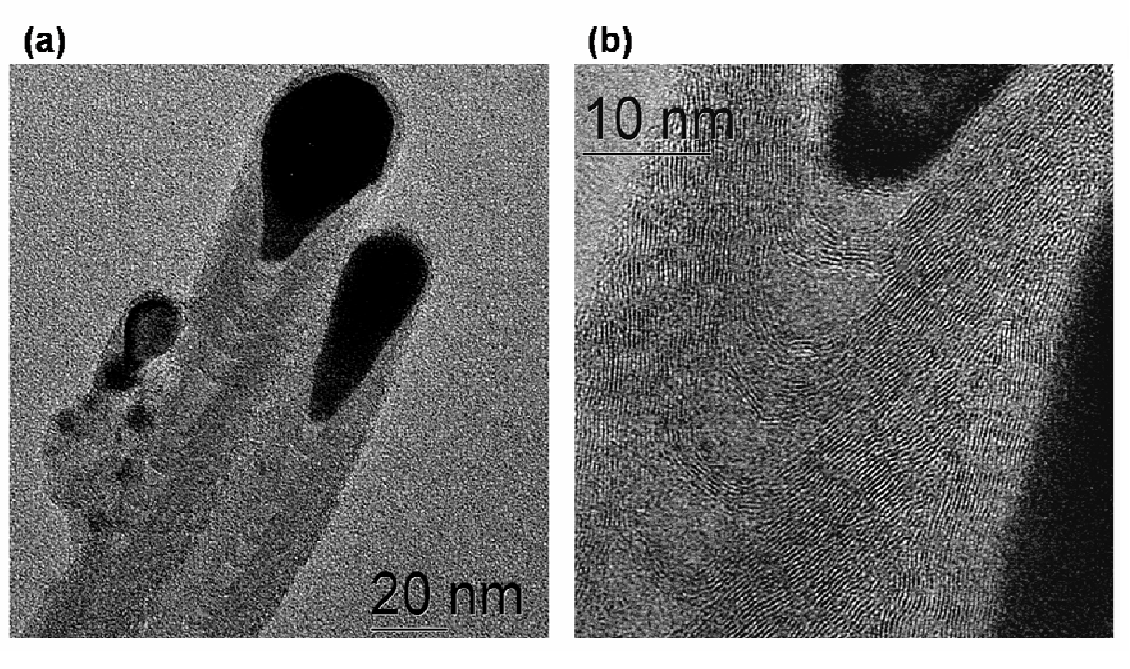

Figure 3.12 (a) TEM image of carbon nanotubes grown using PECVD with 450 V bias. (b) High resolution TEM image to show the detailed bamboo-like structure of carbon nanotubes.

3.4.2 Geometry-controlled growth

From our previous study, the morphology of CNTs can be controlled by adjusting the applied bias in DC-PECVD system.[61] At a low applied voltage of 450V, the size of catalyst particles does not change during growth and the resultant CNTs are equi-diameter nanotubes as shown in Figure 3.13(a) and (b). When the applied voltage is increased, e.g., 600V, the diameter of the catalyst particle on the tip can be gradually reduced due to plasma etching (sputtering) effect, as indicated in Figure 3.13 (c) and (d). The gradually diminishing catalyst size causes the nanotube diameter to change with growth time, resulting in a nanocone configuration and eventual complete elimination of the catalyst particle at the CNT tip, which is the key mechanism to obtain a very sharp tip. The lateral growth and broadening of the nanocones is attributed to be enhanced by the incorporation of redeposited Si which is sputtered away from the substrate surface. This point is supported by the previous study and EDX analysis in TEM. In these experiments, all growth parameters including the temperature and feed gas ratio were kept constant except the applied dc bias.

By using this technique, CNTs with sharp tips and mechanically stable cone bases can be fabricated, which are desired for applications of AFM imaging. Hence, this growth technique was then applied to fabricate CNT AFM probes. Shown in Figure 3.14(a)-(c) are the SEM images of a single CNT probe grown with a Ni catalyst island patterned by EBID method on a Si tipless cantilever at a dc bias voltage of 450 V, 500 V and 550 V, respectively, for 10 min. At the lower bias of 450 V, slender, a straight and equi-diameter CNT with ~70 nm diameters were grown vertically aligned as shown in Figure 3.14(a). The Ni catalyst particle on the top of the CNT tip is about the size of the CNT diameter. When the bias is raised up to 500 V, the CNT probe (Figure 3.14b) shows the tendency toward transition to a conical shape, and the size of catalyst particle is apparently becoming smaller due to the sputtering effect as the growth process continues. Compared to the 500 V condition, when applying 550V bias in10 min growth time, the catalyst particle was totally etched away and a CNT probe with a sharp tip was obtained, as shown in Figure 3.14(c).

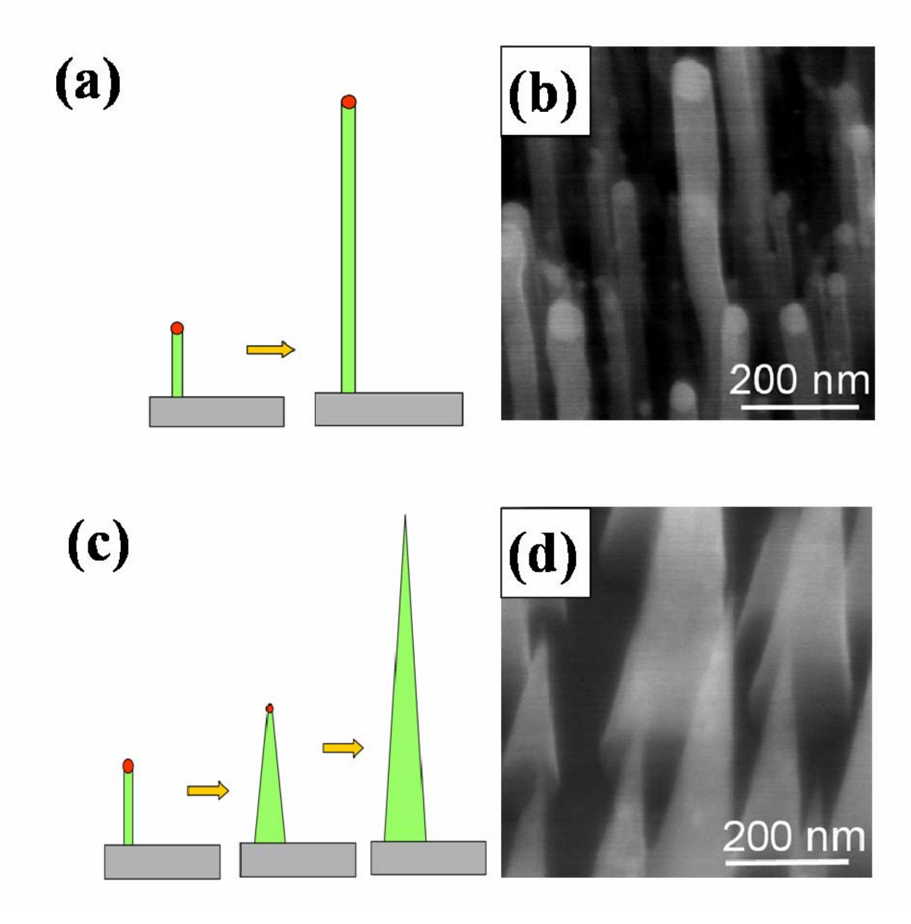

Figure 3.13 (a) Schematic illustration of equi-diameter carbon nanotube growth. (b) SEM image of equi-diameter CNTs grown on Si substrate at a dc bias of 450 V for 20 min. (c) Schematic illustration of gradual reduction of catalyst particle at the CNT tip by sputtering and accompanying reduction in CNT diameter. (d) SEM image of conical CNTs with the catalyst particles completely removed at 600 V for 20min.

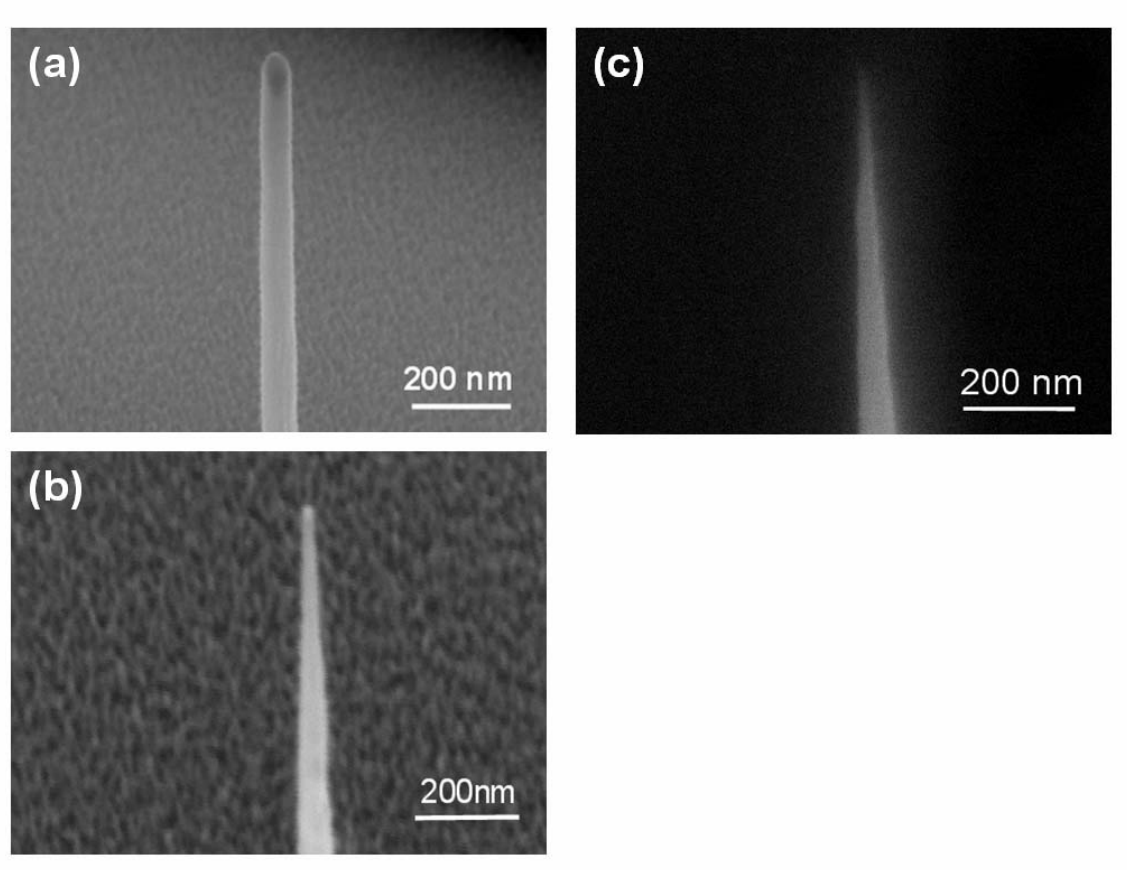

Figure 3.14 SEM images of CNT probes grown on a Ni catalyst dot made by EBID patterning method at a dc bias of (a) 450 V, (b) 500 V and (c) 550 V, respectively, for 10 min.

Figures 3.15(a) and (b) show the SEM images of a CNT probe (marked by an arrow) grown on a tipless cantilever. In Figure 3.15(a), a single CNT probe grown near the edge of a tipless cantilever is shown. Figure 3.15(b), a higher magnification SEM micrograph, shows a CNT with ~2.5 μm height, 200 nm base diameters, and a cone angle <5°. The inset in Figure 3.15(b) is an example TEM image of CNC tip which shows the tip radius of curvature of only a few nanometers.

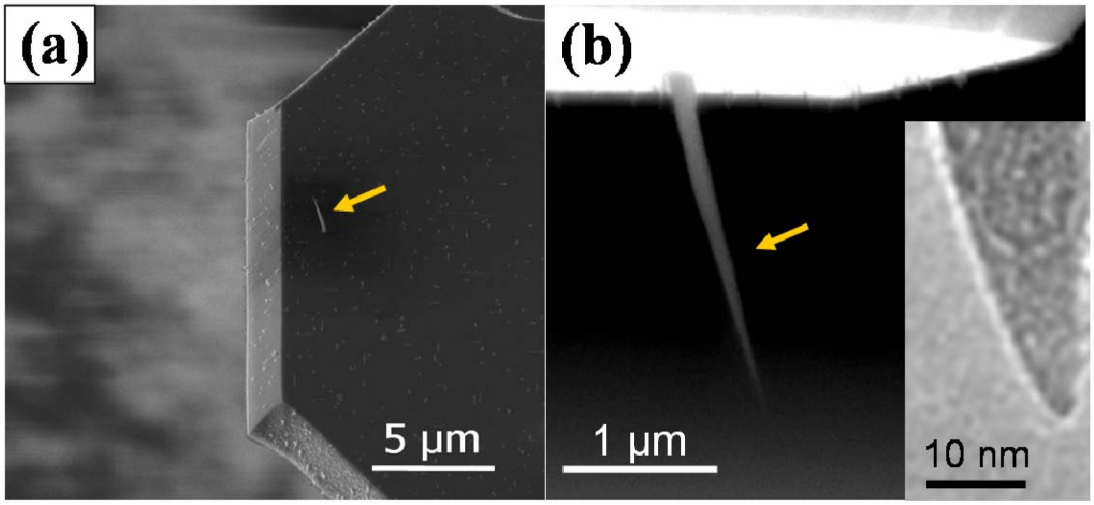

Figure 3.15 (a) SEM image of a single CNT probe grown near on the edge of a cantilever (low-magnification, 30 degree tilted view). (b) Side view SEM image of the CNT probe. Inset: TEM image of the CNT tip.

3.4.3 Direction-controlled growth

During normal AFM operations, the AFM cantilever is titled approximately 11° with respect to the surface normal direction of the sample for reducing the interaction between the cantilever beam and test sample. Thus, the growth direction of CNT probes needs to be well-controlled in order to compensate the operation tilt angle of the AFM cantilever, so that the probe itself is close to being vertical for stable imaging.

The correlation between the alignment of CNTs and the growth mode (base or tip) has been studied in the PECVD growth process.[62] In the case of tip growth mode, the catalyst particle follows the direction of the electric-field lines present in the plasma sheath. Thus, vertically aligned CNTs can be obtained by using PECVD growth on a flat substrate since the field direction is usually perpendicular to the flat substrate. In contrast, it has been shown that base-type CNTs tend to grow in random orientations.

The alignment of CNTs by electric fields has been demonstrated by several groups.[30, 63-65] Merkulov et al. show that he field direction can be changed by placing the substrate close to the edges of the substrate holder, and CNTs can be grown along variety of angles other than perpendicular to the substrate surface.[63] The application of both dc and ac fields in a thermal CVD process was shown to align SWNTs and grow them suspended above a substrate.[64] From our previous study,[65] the growth direction of CNTs can be controlled by adding an additional metal piece close to the sample as an extended cathode part, which can be used to adjust the electric field direction within the dc plasma sheath.

The CNT probe is grown near the free-end of the cantilever, so that the CNT growth direction is titled from the normal direction since electric field close to the cantilever end is not perpendicular to the cantilever surface. Figure 3.16 shows a simulation of field lines on a cantilever beam within a plasma sheath by using FlexPDE5 software (PDE Solutions, Inc.). The simulation was done with the assumption of a vacuum inside the chamber. The field line direction near the cantilever end is ~ 12° with respect to the normal direction of the cantilever surface, which is approximately equal to the tilt angle of the cantilever in the AFM operation. From Figure 3.15(b), the PECVD-grown CNT probe is ~ 13° titled away from the perpendicular, which matches the simulation results very well. Thus, no electric field adjustment is needed to obtain desirable tilt CNT probes during growth.

It should be noted that the CNT probe can be made intentionally tilted by manipulating the electric field direction during CVD growth by placing an additional metal piece close to the cantilever, as described in ref. 65. Figure 3.17 shows some examples of the CNT probes grown at different tilt angles with the cantilevers.

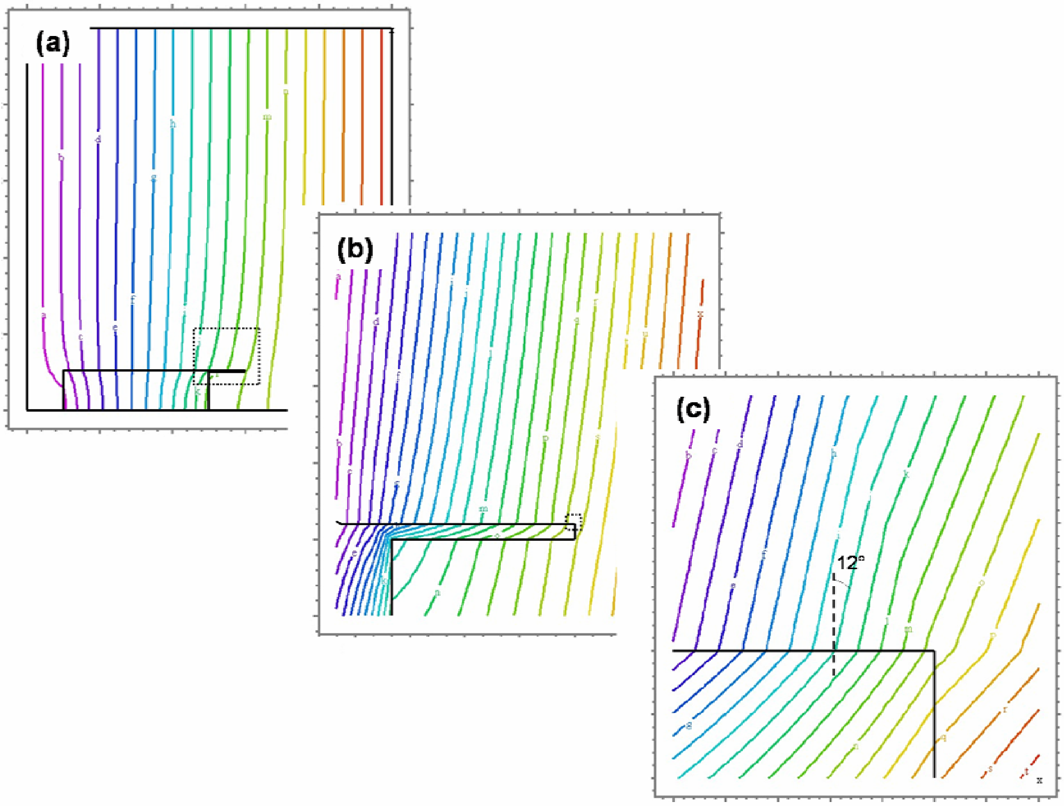

Figure 3.16 Plots of the simulated electric field lines between the anode and cathode and around the cantilever end with the assumption of a vacuum between the electrodes. Progressively enlarged areas of the cantilever part in (a) are shown in (b) and (c).

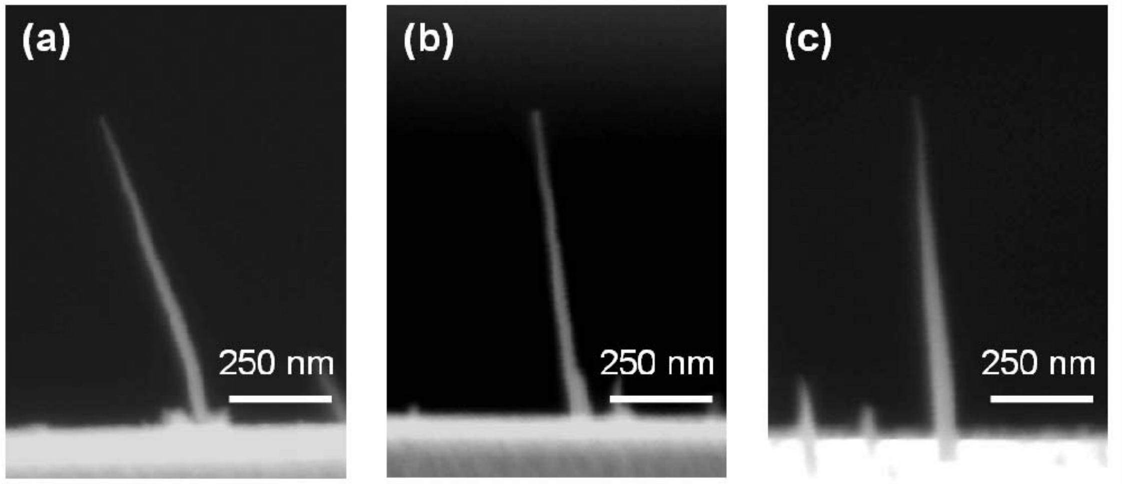

Figure 3.17 SEM images of CNT probes grown using electric-field-guided PECVD method with a titled angle of (a) 20°, (b) 10° and (c) 5°.

3.5 Acknowledgments

The parts of the following papers were selected as the content of this study: "Extremely Sharp Carbon Nanocone Probes for Atomic Force Microscopy Imaging", I.-C. Chen, L.-H. Chen, X.-R. Ye, C. Daraio, S. Jin, C. A. Orme, A. Quist and R. Lal, Applied Physics Letters 88, 153102 (2006), "Fabrication of high-aspect-ratio carbon nanocone probes by electron beam induced deposition patterning", I.-C. Chen, L.-H. Chen, C. A. Orme, A. Quist, R. Lal and S. Jin, Nanotechnology 17, 4322 (2006), "Control of curvature in highly compliant probe cantilevers during carbon nanotube growth", I.-C. Chen, L.-H. Chen, C. A. Orme and S. Jin, Nano Letters (in press) and "Iron-platinum coated carbon nanocone probes on tipless cantilevers for high resolution magnetic force imaging", I.-C. Chen, L.-H. Chen, A. I. Gapin, S. Jin, L. Yuan and S.-H. Liou, Nanotechnology (Submitted). The dissertation author was the primary investigator and author of these papers.

3.6 References

[1] H. W. Kroto, J. R. Heath, S. C. Obrien, R. F. Curl, and R. E. Smalley, *Nature (London)* **318**, 162 (1985).

[2] S. Iijima, *Nature (London)* **354**, 56 (1991).

[3] M. Monthioux and V. Kuznetsov, *Carbon* **44**, 1621 (2006).

[4] L.V. Radushkevich and V.M. Lukyanovich, *Zurn Fisic Chim* **26,** 88 (1952).

[5] C. H. Olk and J. P. Heremans, *J. Mater. Res.* **9**, 259 (1994).

[6] S. Iijima, T. Ichihashi, *Nature* (*London*) **363**, 603 (1993).

[7] D. S. Bethune, C. H. Kiang, M. S. de Vries, G. Gorman, R. Savoy, J. Vazquez,R. Beyers, *Nature* (*London*) **363**, 605 (1993).

[8] M. Dresselhaus, G. Dresselhaus and P. Eklund, *Science of Fullerenes and Carbon Nanotubes,* Academic Press, San Diego (1996).

[9] A. V. Melechko, V. I. Merkulov, T. E. MacKnight, M. A. Guillom, K. L. Klein, D. H. Lowndes, and M. L. Simpson, *J. Appl. Phys.* **97**, 041301 (2005).

[10] C. Dekker, *Phys. Today* **52**, 22 (1999).

[11] J. Nygard, D. H. Cobden, M. Bockrath, P. L. McEuen, P. E. Lindelof, *Appl.Phys. A* **69**, 297 (1999).

[12] N. Hamada, S. Sawada and A. Oshiyama, *Phys. Rev. Lett.* **68**, 1579 (1992).

[13] J. M. Mintmire, B. I. Dunlap and C. T. White, *Phys. Rev. Lett.* **68**, 631 (1992).

[14] M. Bockrath et al., *Science.* **275**, 1922 (1997).

[15] S. J. Tans et al., *Nature.* **386**, 474 (1997).

[16] S. Frank et al., *Science.* **280**, 1744 (1998).

[17] J.W.G. Wildoer et al., *Nature.* **391**, 59 (1998).

[18] T. W. Odom et al., *Nature.* **391**, 62 (1998).

[19] Z. Yao et al., *Nature.* **402**, 274 (1999).

[20] J. P. Lu., *Phys. Rev. Lett.* **79**, 1297 (1997).

[21] A. Garg, J. Han and S. B. Sinnott, *Phys. Rev. Lett.* **81**, 2260 (1998).

[22] M.M. J. Treacy, T. W. Ebbesen and J. M. Gibson, *Nature* **381**, 678 (1996).

[23] E. W. Wong, P. E. Sheehan, and C. M. Lieber, *Science* **277**, 1971 (1997).

[24] R. S. Ruoff, D. Qian and W. K. Liu, *C. R. Phys.* **4**, 993 (2003).

[25] J. Lu and J. Han, *Int. J. High Speed Electron. Sys.*, **9**, 101 (1998).

[26] W. Kratschmer, L. D. Lamb, K. Fostiropoulos and D. R. Huffman, *Nature* (London) **347**, 354 (1990).

[27]A. M. Cassell, J. A. Raymakers, J. Kong and H. J. Dai, *J. Phys. Chem. B* **103**, 6484 (1999).

[28] W. Z. Li, S. S. Xie, L. X. Qian, B. H. Chang, B. S. Zou, W. Y. Zhou, R. A. Zhao and G. Wang, *Science* **274**, 1701 (1996).

[29] A. Moisala, A. G. Nasibulin and E. I. Kauppinen, *J. Phys.: Condens. Matter* **15**, S3011 (2003).

[30] C. Bower , W. Zhu , S. Jin and O Zhou, *Appl. Phys. Lett.***77** 830 (2000).

[31] C. Bower, O Zhou, W. Zhu, D. J. Werder and S. Jin, *Appl.Phys. Lett.* **77** 2767 (2000).

[32] V. I. Merkulov, D. H. Lowndes, Y. Y. Wei, G. Eres and E. Voelkl, *Appl. Phys. Lett.* **76** 3555 (2000).

[33] J. Liu et al., *Science.* **280**, 1253 (1998).

[34] M. Meyyappan, L. Delzeit, A. Cassell1 and D. Hash, *Plasma Sources Sci. Technol.* **12** 205 (2003).

[35] R. T. K. Baker, *Carbon* **27**, 315 (1989).

[36] W. Zhu, C. Bower, O. Zhou, G. Kochanski, S. Jin, *Appl. Phys. Lett.* **75**, 873 (1999).

[37] C. Bower, W. Zhu, D. Shalom, D. Lopez, L. –H. Chen, P. L. Gammel, S. Jin, *Appl. Phys. Lett.* **80**, 3820 (2002).

[38].H. Dai, J. H., Hafner, A. G. Rinzler, D. T. Colbert, and R. E. Smalley, *Nature* **384**, 147 (1996).

[39] M. Radosavljevic, J. Appenzeller, P. Avouris and J. Knoch, *Appl.Phys. Lett.* **84** 3693 (2004).

[40] B.M. Kim, T. Brintlinger, E. Cobas, H. Zheng, M. Fuhrer, Z. Yu, R. Droopad, J. Ramdani and K. Eisenbeiser, *Appl.Phys. Lett.* **84** 1946 (2004).

[41] E.S. Snow, F.K. Perkins, E.J. Houser, S.C. Badescu and T.L. Reinecke, *Science* **307** 1942 (2005).

[42] M. W. Rowell, M. A. Topinka, M. D. McGehee, H. J. Prall, G. Dennler, N. S. Sariciftci, L. B. Hu and G. Gruner, *Appl. Phys. Lett.* **88**, 233506 (2006).

[43] J. Li, Q. Ye, A. Cassell, H. T. Ng, R. Stevens, J. Han and M. Meyyappan, *Appl.Phys. Lett.* **82** 2491 (2003).

[44] L. Ekstrand, Z. Mo, Y. Zhang and J. Liu, *5th International Conference on Polymers and Adhesives in Microelectronics and Photonics*, *Polytronic*, 185 (2005).

[45] J.H. Hafner, C. L. Cheung and C. M. Lieber, *J. Am. Chem. Soc.* **121** 9750 (1999).

[46] E. Yenilmez, Q. Wang, R. J. Chen, D. Wang and H. Dai, *Appl. Phys. Lett.* **80** 2225 (2002).

[47] Q. Ye, A.M. Cassell, H.B. Liu, K.J. Chao, J. Han and M. Meyyappan, *Nano lett.* **4**, 1301 (2004).

[48] H. Cui, S. V. Kalinin, X. Yang, and D. H. Lowndes, *Nano lett.* **4**, 2157 (2004).

[49] J. H. L. Watson, *J. Appl. Phys.* **18**, 153 (1947).

[50] V. E. Cosslett, *J. Appl. Phys.* **18**, 844 (1947).

[51] J. Hillier, *J. Appl. Phys.* **19**, 226 (1948).

[52] A. E. Ennos, Br. *J. Appl. Phys.* **4**, 101 (1953).

[53] K. M. Poole, *Proc. Phys. Soc. London, Sect. B* **66**, 542 (1953).

[54] A. E. Ennos, Br. *J. Appl. Phys.* **5**, 27 (1954).

[55] R. K. Hart, T. F. Kassner, and J. K. Maurin, *Philos. Mag.* **21**, 453 (1970).

[56] R. W. Christy, *J. Appl. Phys.* **31,** 1680 (1960).

[57] H. W. P. Koops, R. Weiel, D. P. Kern, and T. H. Baum, *J. Vac. Sci. Technol. B* **6**, 477 (1988).

[58] Y. M. Lau, P. C. Chee, J. T. L. Thong, and V. Ng, *J. Vac. Sci. Technol. A* **20**, 1295 (2002).

[59] H. W. P. Koops, J. Kretz, M. Rudolph, and M. Weber, *J. Vac. Sci. Technol. B* **11**, 2386 (1993).

[60] A. N. Broers, W. W. Molzen, J. J. Cuomo, and N. D. Wittels, *Appl. Phys. Lett.* **29**, 596 (1976).

[61] L.-H Chen, J. F. AuBuchon, A. Gapin, C. Daraio, P. Bandaru, S. Jin, D. W. Kim, I. K. Yoo and C. M. Wang, *Appl. Phys. Lett.* **85**, 5373 (2004).

[62] V. I. Merkulov, A. V. Melechko, M. A. Guillorn, D. H. Lowndes, and M. L. Simpson, *Appl. Phys. Lett.* **79**, 2970 (2001).

[63] V. I. Merkulov, A. V. Melechko, M. A. Guillorn, M. L. Simpson, D. H. Lowndes, J. H. Whealton, and R. J. Raridon, *Appl. Phys. Lett.* **80**, 4816 s2002d.

[64] A. Ural, Y. Li, H. Dai, *Appl. Phys. Lett.* **81**, 3464 (2002).

[65] J. F. AuBuchon, L. H. Chen, A. I. Gapin, D. W. Kim, C. Daraio and S. Jin, *Nano lett.* **4**, 1781 (2004).

CHAPTER 4: CONTROL OF CANTILEVER BENDING DURING GROWTH

4.1 Introduction

Although CNT AFM probes have been fabricated using PECVD growth and used to demonstrate tapping-mode AFM images, the direct growth of a CNT probe on a thin and highly flexible cantilever by PECVD for contact-mode imaging has not been reported. Unlike the tapping-mode AFM cantilever beam, which is usually > 2 μm thick and < 125 μm long, the contact-mode AFM cantilever beam is thinner (~1 μm) and longer (> 250 μm) in order to image soft or fragile materials. Plasma-induced surface stresses in such fabrication processes, however, tend to cause serious bending of these cantilevers, which makes the CNT probe unsuitable for AFM measurements. Here, we report a new tunable CNT growth technique that controls cantilever bending during deposition, thereby enabling the creation of either flat or deliberately curved AFM cantilevers containing a CNT probe. By introducing hydrogen gas to the (acetylene + ammonia) feed gas during CNT growth and adjusting the ammonia to hydrogen flow ratio, the cantilever surface stress can be altered from compressive to tensile stress, thereby controlling the degree of cantilever bending. The CNT probes grown under these conditions have high aspect ratios and are robust. Such CNT probes can be useful for bio-imaging involving DNA and other delicate biological features.

4.2 Plasma-induced damage and stress

4.2.1 Definition of surface stress

Surface stress is one of the most important properties of the solid surface, which has huge influence on the mechanical, electrical and optical properties of the materials, especially for thin films. The surface stress is often caused by strains at film interfaces, from surface defects, surface disorder, surface reconstruction or bonding configuration.[1]

Surface stress can be defined by analogy with the stress behavior in thin films on a substrate. Figure 4.1 shows the two situations of surface tress. The thin film can contract (defined as a tensile surface stress by which the surface atoms are pulling together) thus bending the cantilever upward, or expand (a compressive surface stress by which the surface atoms or species are pushing one another apart) thus bending the cantilever downward.

Surface stress can be seen as the change in the bulk stress tensor near the surface or an interface. As shown in Figure 4.2, the bulk stress tensor $\tau_{ij}(z)$ has the variation in the vicinity of the surface, and surface stress is defined as the change of the bulk stress tensor, which can be expressed as the integral:[1]

$$\tau_{ij}^{(s)} = \int_{-\infty}^{\infty} (\tau_{ij}(z) - \tau_{ij}^{(b)})dz \quad \text{(N/m)} \qquad (4.1)$$

where $\tau_{ij}^{(s)}$ and $\tau_{ij}^{(b)}$ are the surface stress and bulk stress of the solid respectively. According to the equation (4.1), the unit for surface stress is force per unit length (N/m), as opposed to force per unit area for bulk stress. This definition, along with the elasticity theory, allows for the experimental determination of the change in surface stress, for example, through the bending of a cantilever beam.

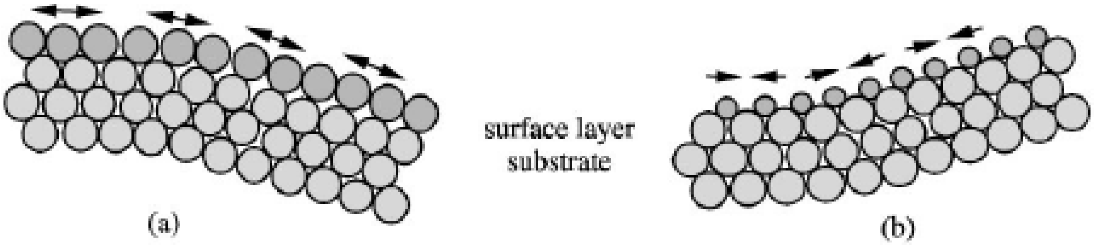

Figure 4.1 Schematic illustrations of (a) compressive surface stress and (b) tensile surface stress.[2]

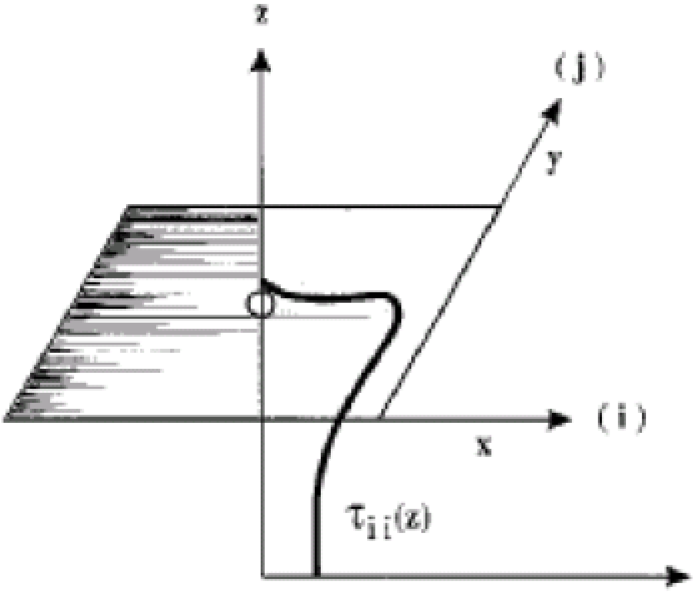

Figure 4.2 Schematic illustration of the variation of bulk stress $\tau_{ij}(z)$ near the surface (bold solid line) which defines the surface stress according to equation (4.1). The indices i and j denote the components of the stress tensor in the x and y direction, respectively.[1]

4.2.2 Introduction of plasma-induced damage and stress

The surface stress has been investigated extensively for many years. It is well known that the undesirable surface stress is generally induced in ion-assisted fabrication processes, such as ion implantation,[3] reactive ion etching[4] and PECVD growth of thin films.[5] During these ion-assisted fabrication processes, the defects can be introduced by energetic ion bombardment, as well as the reactions between the substrate and the ions. With high energetic ion bombardment, the surface of the substrate may be turned from crystalline to amorphous structures. With low energetic ion bombardment, the ion species could etch or react with the sample surface at the same time, and thus the ion species could bind into the lattice or occupy the interstitial sites. In either case, the defect layer is formed on the top of the surface, which introduces surface stresses and could change the surface morphology. Such defects can also increase scattering of mobile charges and reduce carrier lifetimes within the material.

4.3 Surface stress of AFM cantilevers induced during PECVD growth of CNTs

4.3.1 Cantilever bending due to surface stress

Cantilevers are presently the most widely used micromechanical structures in many engineering areas. Cantilevers can be a very sensitive sensor for measurements of surface stress. Koch and Abermann[6] demonstrated that the change of the surface stress induced by the deposition of a single monolayer on one side of the cantilever can be detected by measuring the bending of the cantilever. The bending can also be measured with sufficient sensitivity by deflection of the beam of a laser using a position sensitive detector, as used in AFM measurements.

The bending radius of curvature is directly proportional to changes of the differential surface stress. If the surface stress on one side increases, that side tends to contract and the other side would extend. Hence, changes of the surface stress on both sides cause the cantilever to bend. The radius of curvature, R, is given by[7]

$$\frac{1}{R} = 6\frac{1-\nu}{Et^2}(\Delta\sigma_1 - \Delta\sigma_2) \qquad (4.2)$$

E is the Young's modulus of the cantilever material, ν denotes the Poisson ratio and t is the thickness of the cantilever. $\Delta\sigma_1$ and $\Delta\sigma_2$ are the surface stress changes of the top and bottom side respectively.

During PECVD growth of CNTs, the plasma density is assumed to be constant across the whole cantilever, and thus the uniform plasma-induced surface stress is obtained. For uniform surface stress and isotropic cantilever material, the resulting bending over the whole length is circular with a constant radius of curvature R. Figure 4.3 shows that a cantilever beam is clamped on one side on which there is no deflection and zero slope. In the case of circular bending, the deflection d at the free end of the cantilever is:

$$d = R - \sqrt{R^2 - L^2} \qquad (4.3)$$

where L is the length of the cantilever.

When the deflection is not very severe (R >> L), the deflection d can be expressed by using the binomial series as approximately,

$$d \approx \frac{L^2}{2R} \qquad (4.4)$$

Combining equation (4.2) and (4.4), the total surface stress σ_t is given by,

$$\sigma_t = \Delta\sigma_1 - \Delta\sigma_2 = \frac{Et^2}{3(1-\nu)L^2}d \quad \text{(N/m)} \qquad (4.5)$$

This equation (4.5) is so called Stoney's formula.

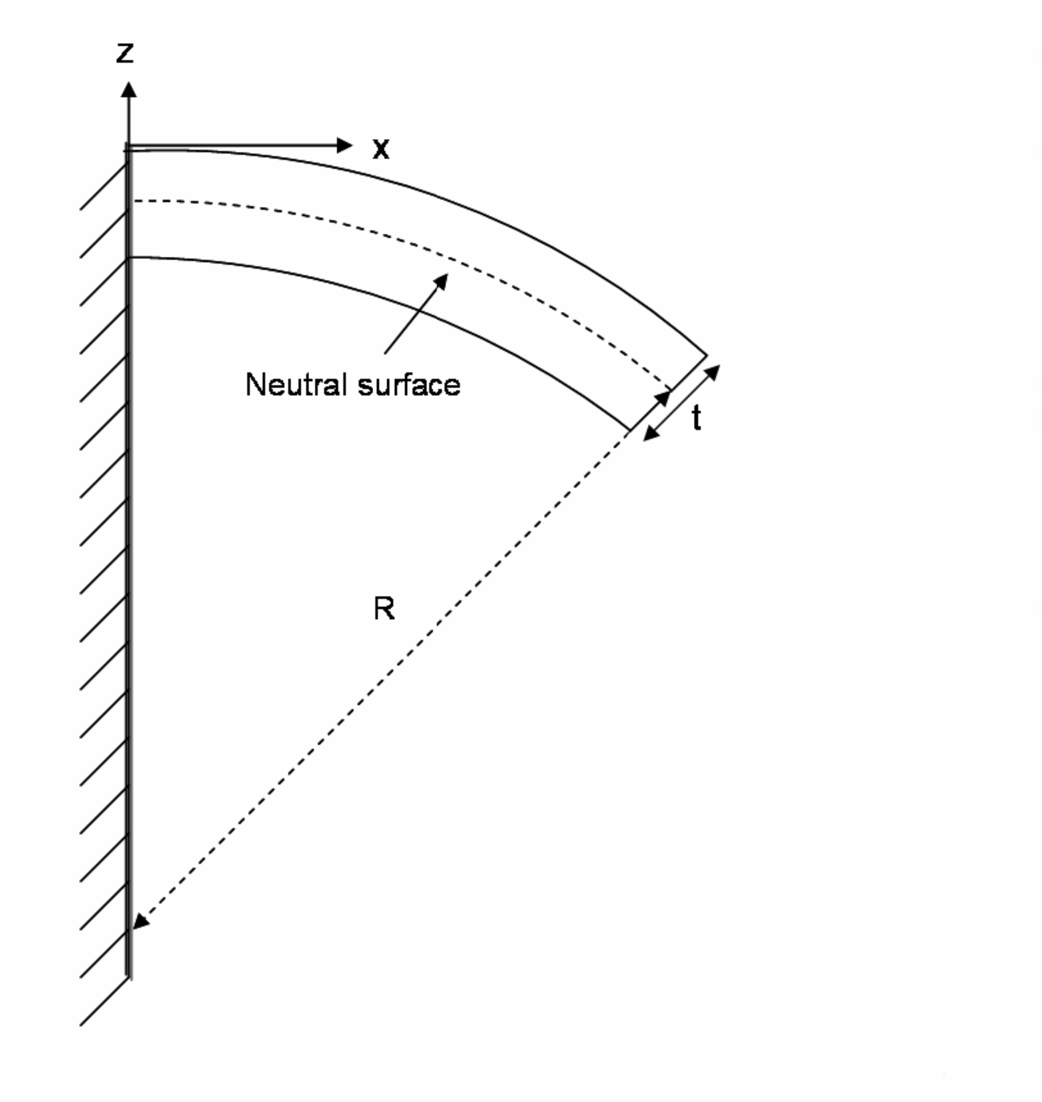

Figure 4.3 Schematic illustration of a bending cantilever of thickness t. For uniform surface stress and isotropic material, the resulting bending over the whole length is circular with a constant radius of curvature R.

4.3.2 AFM cantilever bending during PECVD growth and its effect

For surface metrology of delicate surfaces of soft materials such as living cells, protein molecules, DNA, fragile cell membranes or soft polymer nanostructures, low stiffness AFM probe cantilevers with spring constants < 0.1 N/m, which allow low imaging forces, are desirable to minimize structural damage during scanning. The plasma-induced stresses and damages introduced during PECVD growth of nanotubes, however, result in severely bent cantilevers when thin, low stiffness cantilever are utilized as a substrate. If the bend is sufficiently large, the AFM laser spot focused at their end will be deflected off of the position sensitive detector rendering the cantilevers unusable for AFM measurements.

An example of such an undesirable cantilever bending during CNT growth is shown in Figure 4.4. The probe chip in the figure contains three 1 μm-thick silicon tipless cantilevers with different lengths (250, 300 and 350 μm). It is seen that all three CNT-containing cantilevers are significantly bent upward after PECVD growth of CNTs using a feed gas mixture of acetylene (C_2H_2) and ammonia (NH_3) gas, a commonly used recipe for CNT growth.

Although AFM tapping-mode cantilevers are rather thick and possess higher force constant (> 10 N/m, generally), slight bending can still be observed on some kinds of the cantilevers from our experiments. In general, the slight cantilever bending would not affect normal AFM measurements. However, for some critical and accurate measurements, such as critical dimension measurements, the slight cantilever bending can lead to severely misleading images.

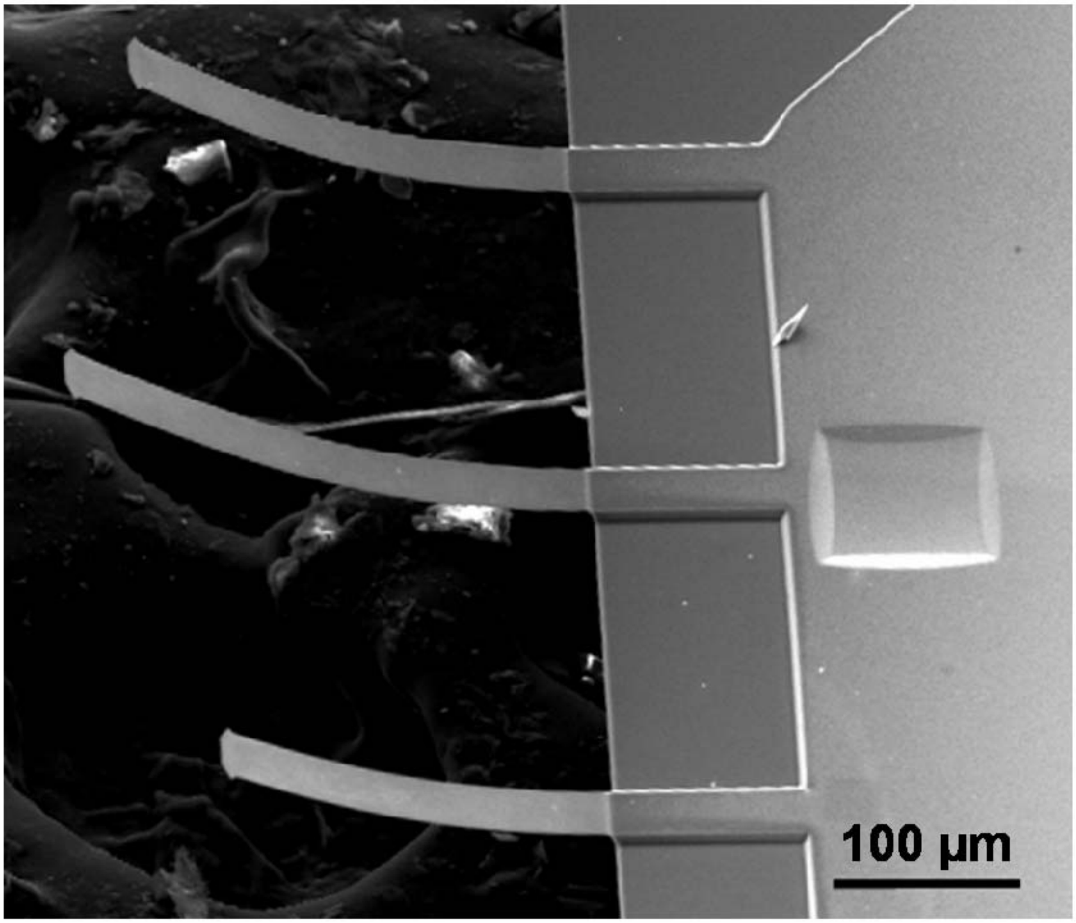

Figure 4.4 SEM image of bent cantilevers after PECVD growth of carbon nanotubes.

4.4 Controlling surface stress of cantilevers during PECVD growth of CNTs

4.4.1 Tensile surface stress of cantilevers induced by ammonia plasma

The CNT probes on tipless cantilevers were fabricated using the EBID patterning technique and DC-PECVD growth method, as described in Chapter 3. The applied dc bias between the cathode and anode is 500 V during PECVD growth. Si tipless cantilever chips (CSC12/Tipless, MikroMasch USA) were used for CNT probe fabrication. The length of the selected cantilevers was ~350 μm. The spring constant was ~0.03 N/m, about three orders of magnitude more compliant than the standard tapping-mode AFM cantilevers.

As pointed out in the previous section, the bending of low stiffness cantilevers during CNT probe fabrication is attributed to the change in surface stresses introduced during the PECVD process. A number of experiments have shown that the profile of low energy (< 1 KeV) ion induced damages can extend tens or even hundreds of times deeper than the nominal ion penetration range for the given acceleration energy (within ~5 nm for most of ions) predicted by Monte Carlo simulation techniques.[8-10] The primary mechanisms for extended defect profiles are radiation enhanced diffusion[9] and channeling.[10] Thus, the NH_3-C_2H_2 mixed plasma, which was turned on with 500 V dc bias, is expected to interact with or induce damages on the Si substrate, especially at the relatively high CNT growth temperature of 700 ˚C, which can enhance thermal diffusion of ions and their interaction rate with Si substrate.

Shown in Figure 4.5 are comparative, cross-sectional cantilever images for three different CNT growth conditions using different feed gas composition. Figure 4.5(a) shows the cantilever bending after 10 min PECVD growth of CNTs using NH_3 and C_2H_2 gases at flow ratio 6:1. It is seen from Figure 4.5(a) that the surface stress on the top surface of the cantilever is tensile and the upward bending deflection in the cantilever is huge (as much as 120 μm), almost a third of the cantilever length of ~350 μm.

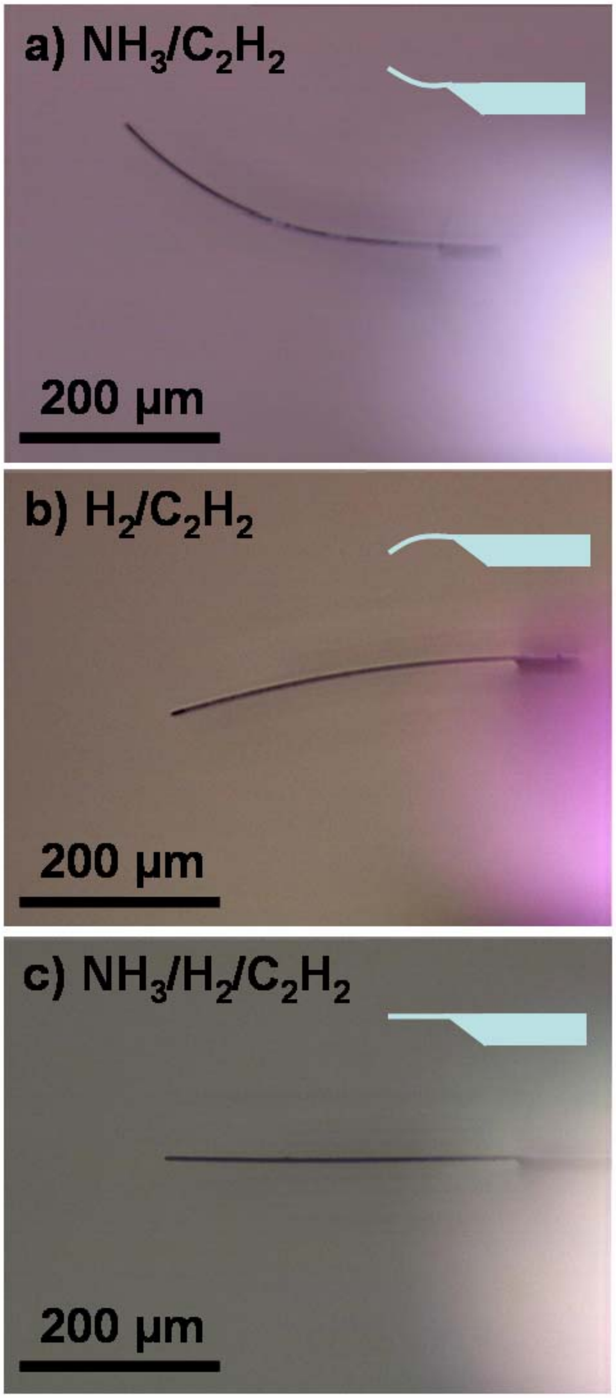

Figure 4.5 Optical microscope images of cantilevers after plasma treatments with C_2H_2 gas and (a) NH_3 gas (R=1). (b) H_2 gas (R=0). (c) Mixed NH_3- H_2 (R=0.5). R is the flow ratio of $NH_3/(NH_3+H_2)$ during PECVD growth of CNTs.

In order to investigate what kinds of plasma-induced damages and surface reactions happened during PECVD growth and caused the surface stress, the change of surface chemistry on the plasma-treated cantilevers was identified by the Fourier transform infrared spectroscopy (FTIR) spectra, which was carried out using a Nicolet Magna 550 spectrometer. Auger electron spectroscopy (AES) and secondary ion mass spectroscopy (SIMS) were used to determine the concentration depth profile of various elements.

An AES depth profile of a Si tipless cantilever before PECVD process was performed to monitor silicon, carbon, oxygen, and nitrogen components on the surface of the cantilever, as shown in Figure 4.6. The Auger exciting energy of the electron beam was 10 keV. It is worth noting that there is no nitrogen signal detectable. Because no effort was made to clean the cantilevers or to remove the native oxide present on the cantilever surfaces before CNT growth, some carbon and oxygen species were detected close to the cantilever surface due to the carbon and oxygen contamination on the cantilever surface.

Oxygen may be originated from the native oxide on the silicon surface which may grow during the exposure in the air or water rinsing process. Carbon may originate from the organic contaminants which come from the cantilever fabrication process or exposing to the air. Compared with the oxygen distribution, the Auger signal of carbon has higher concentration near the surface and deeper depth distribution, as shown in Figure 4.6.

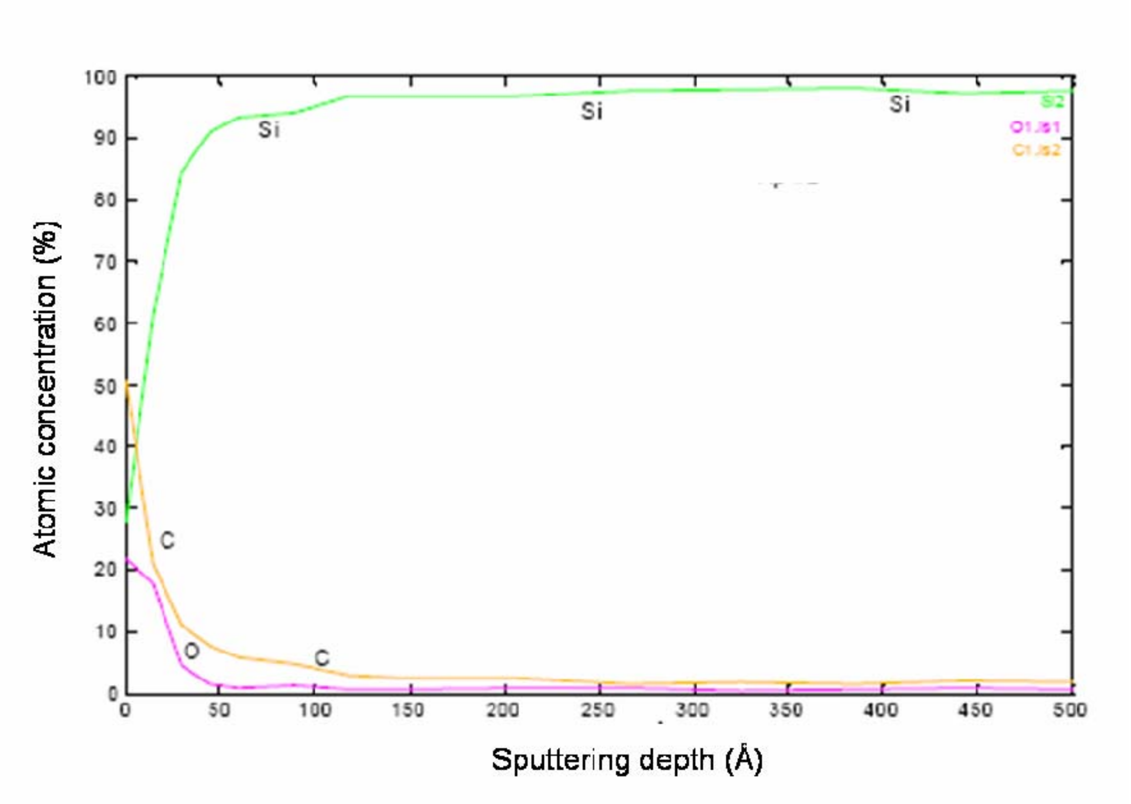

Figure 4.6 AES depth profiles of Si, C, O and N elements obtained from a Si cantilever before the PECVD processing.

The SIMS depth profile measurement was performed on the Si cantilever, shown in Figure 4.7, which was used for PECVD growth of CNTs by using NH_3 and C_2H_2 gases at flow ratio 6:1. Compared with the composition of the cantilever surface before PECVD process, the nitrogen atom concentration not only rises up near the cantilever surface, but also is higher than the concentration of oxygen and carbon, as shown in Figure 4.7. Unlike high energy ion implantation process, the nitrogen concentration has a peak value of 1.68×10^{22} atoms/cm^3 near the surface and then decreases gradually along the penetration depth. It can also be observed that the diffuse depth of nitrogen into the Si substrate is more than 50 nm, much deeper than the TRIM calculation.[11] Thus, the effect of diffusion on the nitrogen distribution curve at high temperatures is significant. It is apparent that the thermal-radiation-enhanced diffusion has resulted in penetration of nitrogen atoms into the substrate. Although the concentration profiles of oxygen and carbon also become a little broader due to growth of the native oxide and diffusion, the higher and broader concentration of nitrogen species is considered as the main factor causing the surface stress.

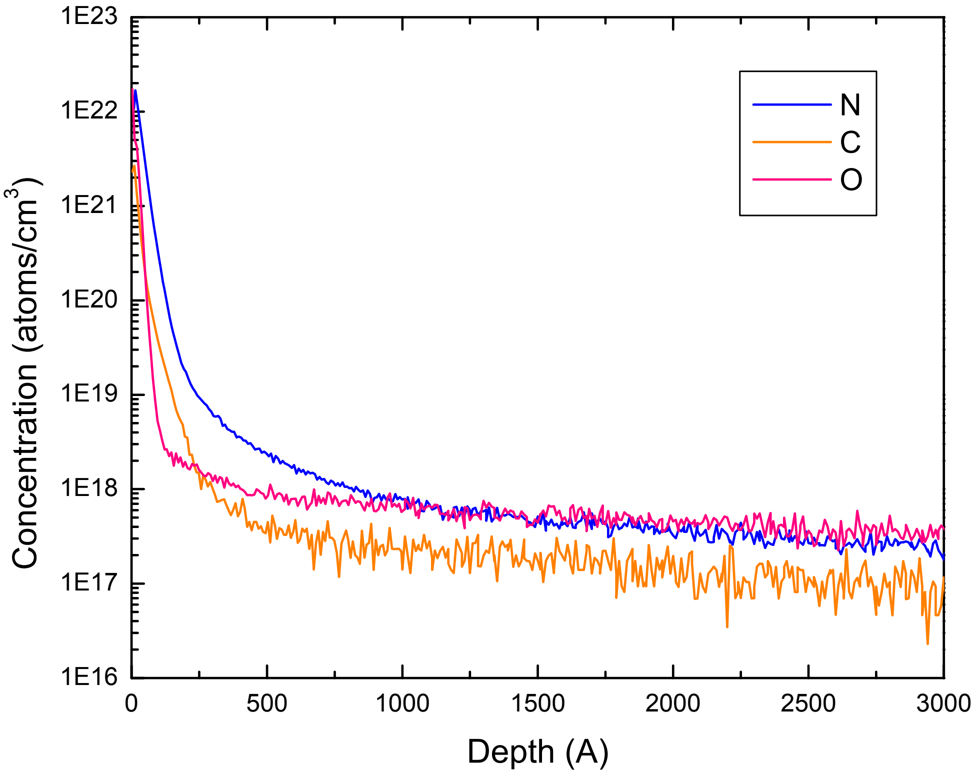

Figure 4.7 SIMS depth profiles of C, O and N elements obtained from a Si cantilever after the PECVD processing.

In order to further investigate the surface chemistry, FTIR measurements were performed on Si samples with 1 cm × 1 cm area with various plasma treatment conditions. The base signal of a non plasma-treated silicon spectrum was subtracted from the data. In the FTIR spectrum of the sample after NH_3-C_2H_2 plasma process, Figure 4.8(a), a large peak is seen near 840 cm^{-1}, which is attributed to the vibrations of the Si-N stretching bonds. The large deflection of the cantilever is most likely caused by ion-induced modification of the Si sub-surface, which can form a defect layer dominated by nitrogen species. It has been reported that NH_3 plasmas were used for nitridation of silicon.[12,13] The growth rate of silicon nitride (Si_3N_4) is very slow (~ 5.5 nm/hr with RF power at a higher temperature of 950 °C) because of the high density of the Si_3N_4 layer.[13] In our case, however, plasma damage may be more dominant because a high bias voltage was directly applied to the substrate , which differs from Ref. 12 and 13. Thus, it is likely that both plasma damage (lattice defect layer) and perhaps some surface reconstruction (non-stoichoimetric nitride formation) contribute to the induced stress in our samples.

The Si-C band at 790 cm^{-1} in the FTIR spectrum of Figure 4.8 is not obvious because the formation of SiC requires a higher temperature with longer annealing time. In addition, NH_3 plasmas can etch away carbohydrate radicals adsorbed on the substrate surface and reduce the interaction between the surface and radicals. Therefore, nitrogen-related damage during CNT growth from the presence of NH_3 feed gas is considered to have a more pronounced effect on the cantilever bending than the C_2H_2 component of the feed gas.

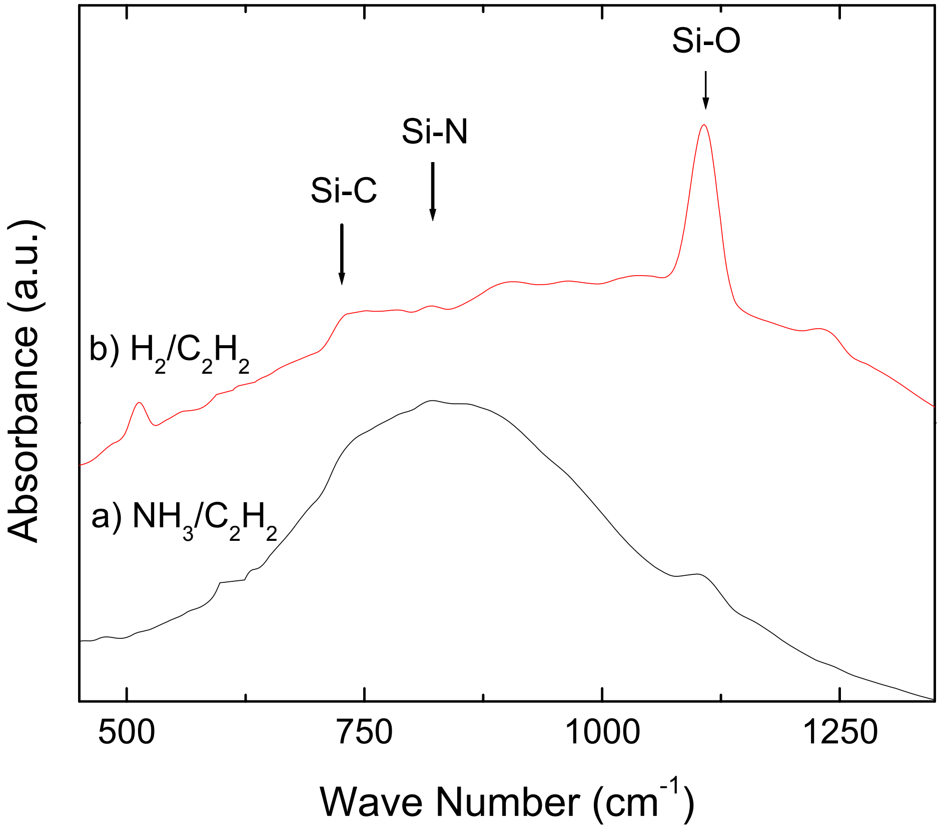

Figure 4.8 FTIR spectra of the silicon substrate. (a) After plasma treatment with C_2H_2 and NH_3 gas (R=1). (b) After plasma treatment with C_2H_2 and H_2 gas (R=0).

4.4.2 Changing Surface stress by introducing another carrier gas

In order to balance the undesirable tensile surface stress of the Si cantilevers induced by NH_3-C_2H_2 plasma, we employed an approach of introducing another type of gas that could induce a stress with an opposite sign (i.e., compressive stress), and yet still enable the CNT growth with desirable configuration. The SiO_2 film grown by thermal oxidation on Si wafers[14] as well as by oxygen plasma oxidation[15] has been observed to induce a compressive stress. Although oxygen plasma can induce compressive stress to compensate the undesirable tensile stress caused by NH_3 plasma, it is not desirable for use in our case because of oxidative etching of CNTs that occurs.

The next choice of gas to be employed in our CNT growth system was hydrogen. It has been reported that a thin SiO_2 layer can still be formed after hydrogen plasma treatment of a porous silicon substrate due to the residual oxygen in the plasma system.[16] It has also been reported that hydrogen implantation may enhance oxygen accumulation at the buried layer,[17] which may induce compressive stress. As hydrogen can be used as a carrier gas for PECVD growth of CNTs, we attempted to apply plasma treatment on the low stiffness Si cantilever using mixed H_2-C_2H_2 gases. The results of this experiment indicate that the H_2-C_2H_2 plasma treatment indeed introduces a compressive stress, thus enabling the downward bending of the cantilever during CNT growth as shown in Figure 4.5(b).

From the FTIR spectrum, Figure 4.8(b), the peak at 1107 cm^{-1} becomes much stronger, which is attributed to interstitial Si-O-Si asymmetric stretch mode with oxygen in interstitial sites of bulk Si. However, there is no obvious Si-O-Si stretching band corresponding to SiO_2 (around 1070 cm^{-1}), which implies that SiO_2 was not quite formed during our plasma treatment. Hence, the observed downward bending Si cantilever is likely caused by interstitial oxygen after the H_2-C_2H_2 plasma treatment. Such interstitial oxygen can put the surrounding Si lattice under a compressive stress.[18] It is thought that the source of oxygen in our PECVD system is most likely from the residual oxygen since the base pressure in the CVD chamber is not very low. The possible reason for the lack of observed SiO_2 is that plasma oxidation from the residual oxygen may be counterbalanced by the reduction reaction in the hydrogen plasma. Further research is needed to elucidate the exact mechanism of surface stress during the plasma treatments.

To determine whether the C_2H_2 gas used for CNT growth has any effect on the surface stresses and cantilever bending, plasma experiments were carried out at the same temperature but without C_2H_2 gas. The results indicate that a similar level of cantilever bending is obtained without using C_2H_2 gas, which implies that NH_3 and H_2 are the main controlling factors that influence the surface stress of the cantilever.

4.4.3 From compressive to tensile stress: tunning flow ratio during PECVD

From the results of the previous section, we know that the surface stress of cantilevers can be adjusted by introducing H_2 into the NH_3+C_2H_2 feed gas for CNT growth. Thus, by adjusting the NH_3-H_2 flow ratio (R) which was defined as $NH_3/(NH_3+H_2)$, different bending profiles of a cantilever can be obtained. Here, the bending of the cantilevers after the plasma processing has been systematically studied as a function of the NH_3/H_2 flow ratio and the length of the cantilevers.

The magnitudes of deflections at the free ends of the cantilevers were measured by an optical profiler (Veeco Wyko NT1100), which can provide high resolution 3D surface measurement, from sub-nanometer roughness to millimeter-high steps. Figure 4.9 shows an example of the deflection measurement of cantilever beams using the optical profiler. The deflection of each cantilever was recorded by taking the average height of the free end of the cantilever with the fixed end of the cantilever as the reference surface. The measured data was also compared with that obtained from measuring the deflection from side-view SEM images of the cantilever. The data from both measurements are similar and consistent.

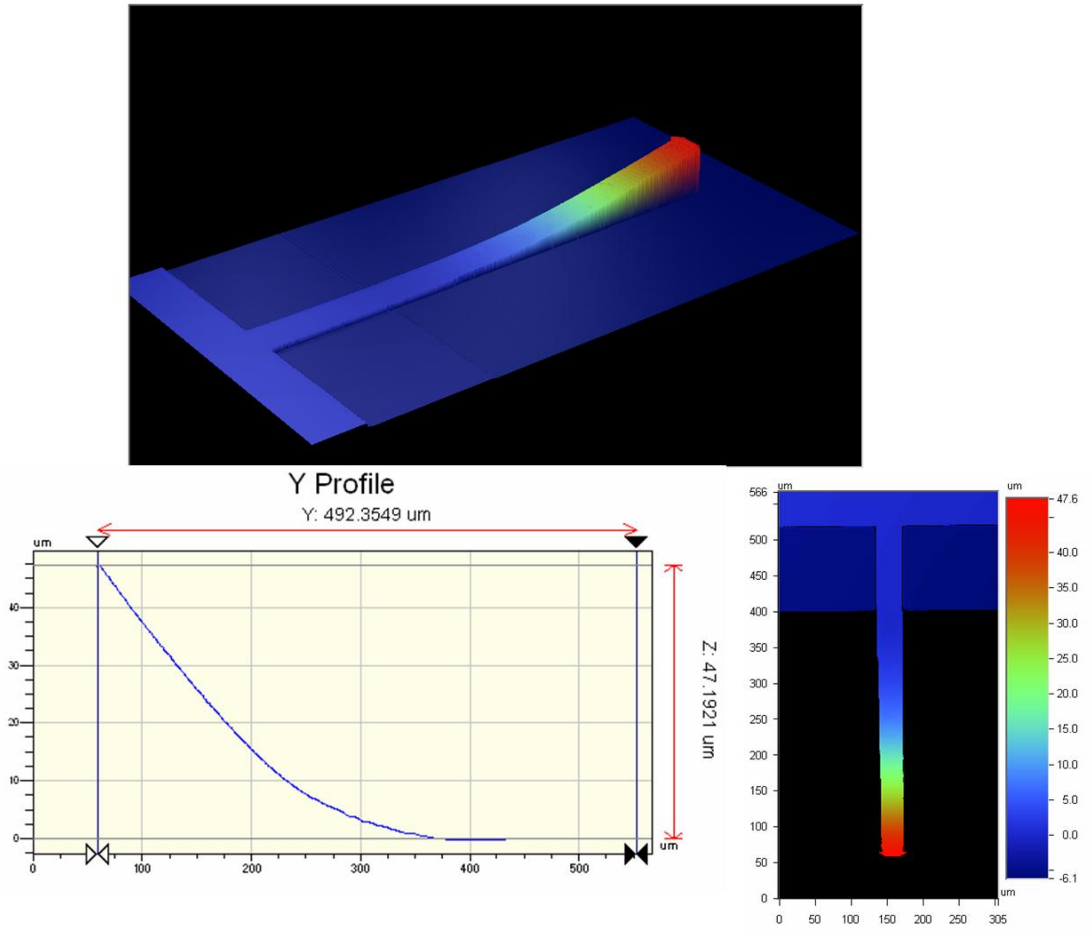

Figure 4.9 Example of the measurement result of the cantilever deflection by a Veeco Wyko NT1100 optical profiler.

Figure 4.10 illustrates deflection profiles vs. gas flow ratio (R) from optical profiling measurements. The positive deflection represents the cantilever surface under tensile stress. By decreasing the gas flow ratio R, the stress condition is changed from tensile to compressive stress. For R=1 (only NH_3 and C_2H_2), a large upward bending of ~120 µm is obtained, while for R=0 (only H_2 and C_2H_2), a large downward bending of ~70 µm is observed as shown in Figure 4.10(a). A stress-free cantilever with essentially flat geometry can be obtained within a window of R value between 0.45 and 0.55. Figure 4.5(c) displays a nearly flat cantilever beam obtained after PECVD growth of a CNT probe employing a gas ratio of R=0.5.

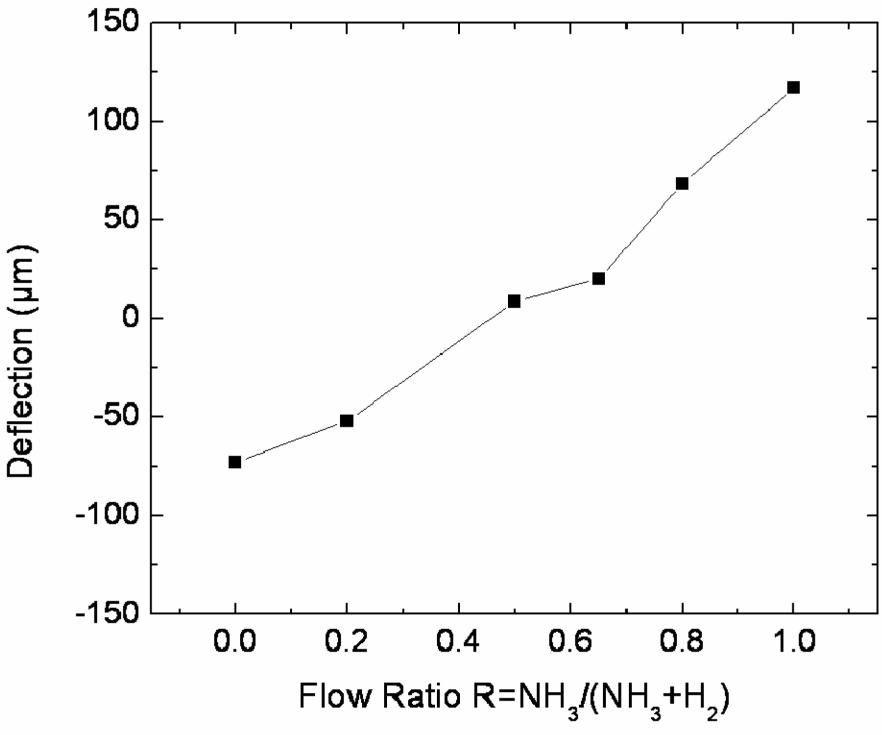

Figure 4.10 Magnitude of the cantilever deflection vs. NH_3- H_2 flow ratio R during nanotube growth.

4.5 CNT probes grown on low stiffness cantilevers

Figure 4.11 shows the SEM image of an AFM probe containing a single, high-aspect-ratio CNT probe grown on a tipless cantilever. The balanced feed gas ratio of R~0.5 discussed above was utilized to avoid undesirable curvature and obtain a flat cantilever of Figure 4.5(c). The inset in Figure 4.11 is a higher magnification SEM micrograph (taken with 45° tilt) of the CNT tip. The height of the CNT was ~2.5 μm and the base diameter was ~250 nm. The cone-shaped probe geometry is desirable, as the wider base provides mechanical rigidity and adhesion strength, while the much sharper tip produces high-resolution imaging without encountering the thermal vibration problem often seen in very thin diameter probes.

Figure 4.12 shows the resonance frequency of the cantilever before and after PECVD growth of a CNT probe with flow ratio R=0.5. The deviation of the resonance frequency is rather small, less than 1 kHz, which means the mechanical properties of the cantilever do not change much after PECVD growth using the (NH_3+H_2) mixed gas together with C_2H_2 gas. The small change in the resonance frequency might have been caused by the plasma-damaged layer or the slight increase in the cantilever mass after PECVD growth of CNTs.

4.6 Acknowledgments

The parts of the following papers were selected as the content of this study: “Extremely Sharp Carbon Nanocone Probes for Atomic Force Microscopy Imaging”, I.-C. Chen, L.-H. Chen, X.-R. Ye, C. Daraio, S. Jin, C. A. Orme, A. Quist and R. Lal, Applied Physics Letters 88, 153102 (2006), “Fabrication of high-aspect-ratio carbon

nanocone probes by electron beam induced deposition patterning", I.-C. Chen, L.-H. Chen, C. A. Orme, A. Quist, R. Lal and S. Jin, Nanotechnology 17, 4322 (2006), "Control of curvature in highly compliant probe cantilevers during carbon nanotube growth", I.-C. Chen, L.-H. Chen, C. A. Orme and S. Jin, Nano Letters (in press) and "Iron-platinum coated carbon nanocone probes on tipless cantilevers for high resolution magnetic force imaging", I.-C. Chen, L.-H. Chen, A. I. Gapin, S. Jin, L. Yuan and S.-H. Liou, Nanotechnology (Submitted). The dissertation author was the primary investigator and author of these papers.

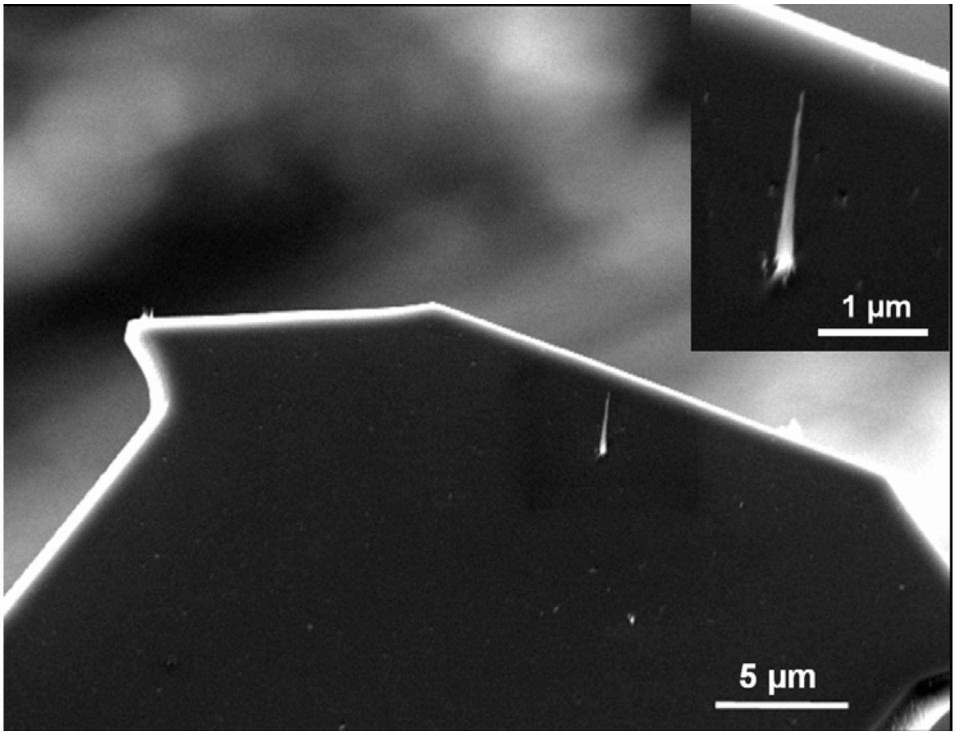

Figure 4.11 SEM image of a single CNT probe grown near the edge of a low stiffness cantilever (45° tilted view). Inset: higher-magnification image of the CNT probe.

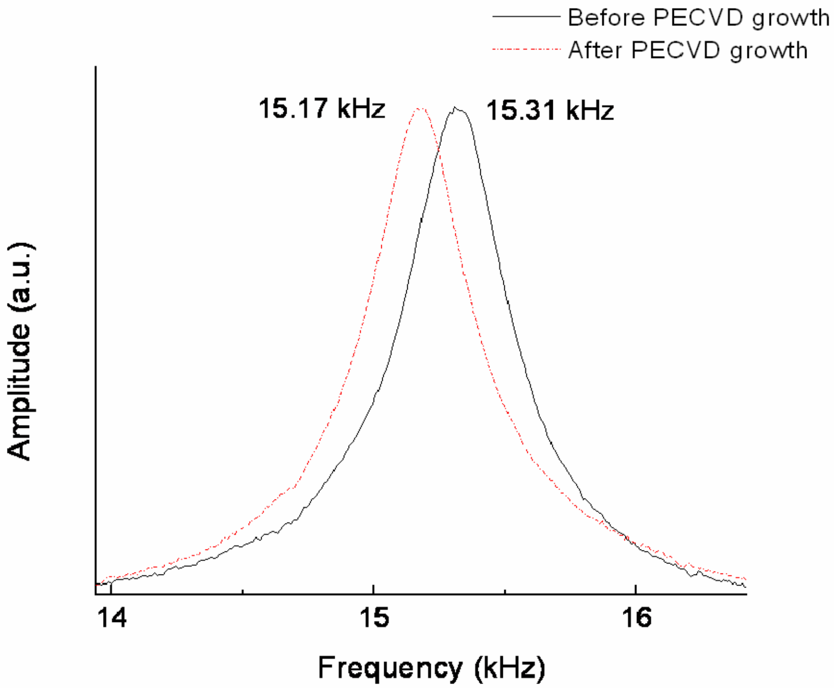

Figure 4.12 Resonance frequency of the low stiffness cantilever before vs. after PECVD growth of a CNT probe.

4.7 References

[1] H. Ibach, *Surf. Sci. Rep.* **29**, 193 (1997).

[2] A. M. Kroto, S. J. O'shea and M. E. Welland, *Ultramicroscopy* **82**, 23 (2000).

[3] P. J. Burnett and T. F. Page, *J. Mater. Sci.* **20**, 4624 (1985).

[4] K. Otte, G. Lippold, F. Frost, A. Schindler, F. Bigl, M. V. Yakushev and R. D. Tomlinson, *J. Vac. Sci. Technol. A* **17**, 19 (1999).

[5] M. Belyansky, N. Klymko, A. Madan, A. Mallikarjunan, Y. Li, A. Chakravarti, S. Deshpande, A. Domenicucci, S. Bedell, E. Adams, J. Coffin, L. Tai, S-P. Sun, J. Widodo and C-W Lai, *Mater. Res. Soc. Symp. Proc.* **863**, 97 (2005).

[6] R. Koch and R. Abermann, *Thin Solid Films* **129** 63 (1985).

[7] G.G. Stoney, *Proc. R. Soc. London, Ser. A* **82** 172 (1909).

[8] D. L. Green, E. L. Hu, and N. G. Stoffel, *J. Vac. Sci. Technol.* **B 12**, 3311 (1994).

[9] C.-H. Chen, D. L. Green, and E. L. Hu, *Appl. Phys. Lett.* **69**, 58 (1996).

[10] M. Rahman, *J. Appl. Phys.*, **82** 2215 (1997).

[11] .J. F. Ziegler, J. P. Biersack, and U. Littmark, *The Stopping and Ranges of Ions in Solids* (Pergamon), New York (1984).

[12] T. Ito, I. Kato, T. Nozaki, T. Nakamura and H. Ishikawa, *Appl. Phys.Lett.* **38** 370 (1981).

[13] S. S. Wong and W. G. Oldham, IEEE Electron Device Lett. **EDL-5,** 175 (1984).

[14] E. Kobeda and E.A. Irene, *J. Vac. Sci. Technol. B* **6**, 574 (1988).

[15] A. N. Itakura, T. Narushima, M. Kitajima, K. Teraishi, A. Yamada, and A. Miyamoto, *Appl. Surf. Sci.* **159–160**, 62 (2000).

[16] U. Grunling, S. C. Gujrathi, S. Poulin, Y. Diawara and A. Yelon, *J. Appl. Phys.* **75**, 8075 (1994).

[17] R. Job, A. G. Ulyashin, W. R. Fahrner, A. I. Ivanov and L. Palmetshofer, *Appl. Phys. A* **72**, 325 (2001).

[18] L. Wei, Y. Tabuki, H. Kondo, S. Tanigawa, R. Nagai and E. Takeda, *J. Appl. Phys.* **70**, 7543 (1991).

CHAPTER 5: HIGH RESOLUITON AFM IMAGING USING CNT PROBES

5.1 Introduction

To demonstrate the advantage and performance of sharp and high-aspect-ratio CNT probes, AFM imaging on several different samples was evaluated and the imaging performance of the commercially conventional tip vs. the CNT tip was compared. Both tapping-mode and contact-mode AFM imaging were performed in air, as well as in liquid environment. In addition, iron-platinum-coated CNT probes were applied for MFM (magnetic force microscopy) applications. They were compared to iron-platinum coated silicon probes by performing magnetic force imaging on magnetic recording media with linear recording densities from 700 to 900 kilo flux changes per inch (kfci).

5.2 Tapping-mode imaging

5.2.1 Tapping-mode imaging in air for copper film surface

The performance of the CNT probe was evaluated in tapping mode using a Dimension 3100 AFM with Nanoscope IIIa controller (VEECO Instruments) for imaging in air. The surface of a copper film (~300 nm thick) sputter deposited on the Si substrate surface was imaged by using a CNT probe, as shown in Figure 5.1(a). The image clearly shows a well-defined and rounded grain structure. The smallest structure imaged is in the regime of a few nanometers. The sharper grain boundaries and image quality were well revealed due to the sharpness of the CNT tip. Compared with the image taken by the CNT probe, the image produced by a conventional Si probe, shown in Figure 5.1(b), shows less clear grains and grain boundaries, especially inside the groove regions.

The section analysis of a zoom-in Cu grain image acquired by the CNT probe was performed by using Nanoscope software image processing. The white line marked in Figure 5.2(b) was chosen to show the line-profile of the Cu AFM image. The cut section shown in Figure 5.2(a) and a three-dimensional image in Figure 5.2(c) clearly indicate that the CNT tip can analyze the groove regions of Cu grains with nano-scale resolution.

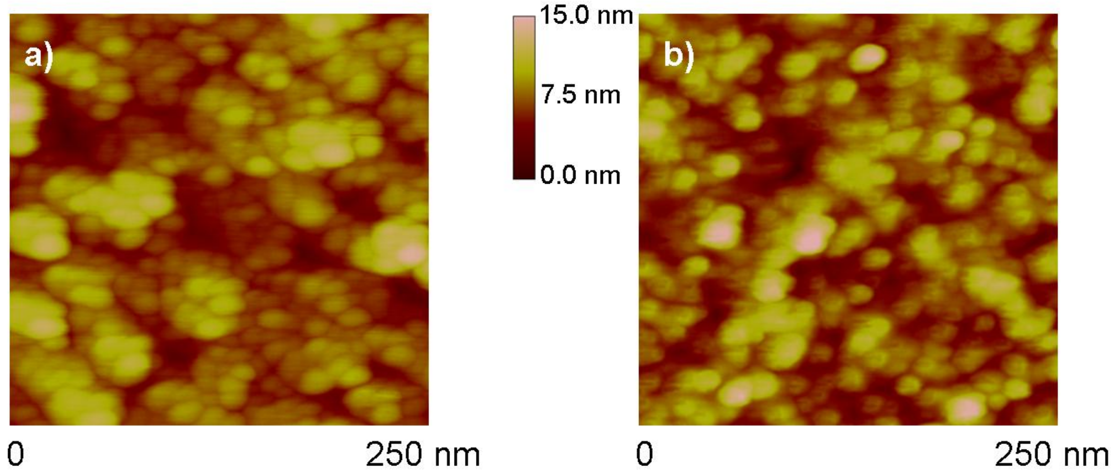

Figure 5.1 AFM tapping-mode images of a copper thin film on the silicon substrate using (a) A CNC probe. (b) A commercial Si probe.

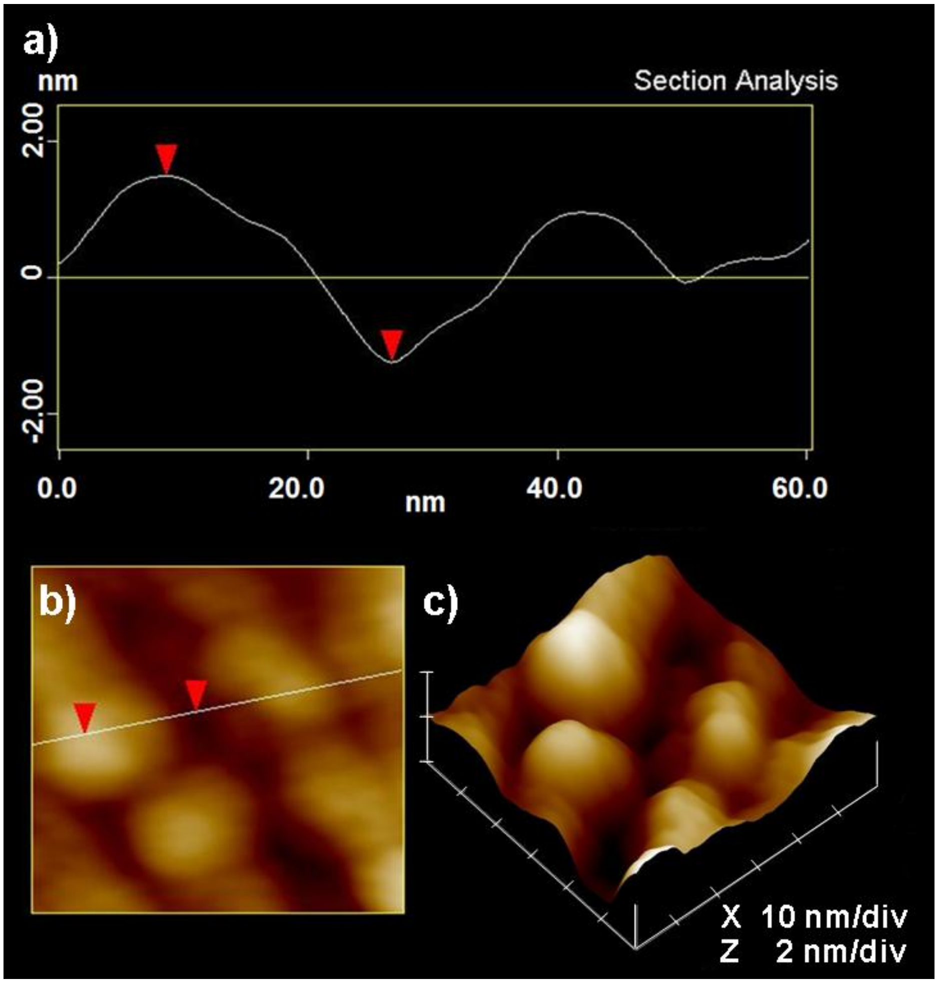

Figure 5.2 (a) Section analysis of the zoom-in Cu grain AFM image. (b) A zoom-in Cu grain AFM image. (White line was chosen to show the line-profile.) (c) The three dimensional image of image (b).

5.2.2 Tapping-mode imaging in air for high-aspect-ratio patterns

To demonstrate the advantage of a CNT probe on imaging a high-aspect-ratio structure, a 500 nm deep PMMA (polymethyl methacrylate) resist pattern (300 nm line/space) on a Si substrate was evaluated and the imaging performance of the conventional Si probe vs. the CNT probe was compared. The image acquired with a Si probe, Figure 5.3(a), shows a misleading image pattern due to the tip convolution of the pyramidal tip. The CNT probe on the other hand reveals the much more actual geometry of the pattern including the configuration of the vertical walls, implying that the CNT probe is able to trace the contour of the deep profile pattern, as presented in Figure 5.3(b).

Further section analysis of the AFM images taken by Si and CNT tips is shown in Figure 5.4. The scan direction of imaging the PMMA trench pattern is zero degree, i.e. paralleling to longitudinal direction of the cantilever. For the commercial Si probe, the front and back angle of a Si pyramidal probe (TESP, Veeco probes) are ~ 25° and 12° respectively. Since the mounted probe chip is tilted around 12° during imaging, the imaged right sidewall slope of 55° ~ 56° and a left sidewall slope of 86° ~ 88° of the pattern actually matches those of the Si pyramid shape itself, as shown in Figure 5.4(a) and (c). From a calculation of geometry, the Si pyramid tip can not possibly reach the bottom of PMMA pattern. The experimental results also confirmed this, as Figure 5.4(c) shows a 430 nm high line profile of the PMMA trench which height is 500 nm in reality.

On the other hand, the conical CNT probe used for imaging is 2.5 μm long with ~ 5° cone angle and 200 nm base width. As predicted, the line profile of the same pattern acquired with the CNT tip shows near vertical slopes of 86° ~ 88° on both sidewall, shown in Figure 5.4(b) and (d). The commercial Si probes possess pyramidal shape with different side, front and back angles, which always result in imaging artifacts. The orientation angle of mechanically-attached or thermal CVD grown CNT probes is difficult to control, and thus causes image distortion. Because of the symmetrical conical shape and well-controlled growth direction during the PECVD process, our CNT probe can produce correct images in any scanning direction, unlike commercial Si probes or mechanically-attached or thermal CVD grown CNT probes. When the MWNT tips are of great length (>1 μm) and attached to high stiffness microcantilevers, mechanical buckling of the CNT is often encountered and imaging artefacts are introduced. The data demonstrates that our conical CNT probe is mechanically stable, and is strong enough to trace the abrupt step structure without introducing artifacts or breaking the tip.

As the experimental results shown in both this and the previous sections, the conical CNT probes which possess sharp tips and high-aspect-ratio geometry yield high resolution AFM images of nano-scale features and deep trenches. This kind of conical CNT probe combines the advantages of the sharp tips of SWNTs with the high stiffness of large diameter MWNTs.

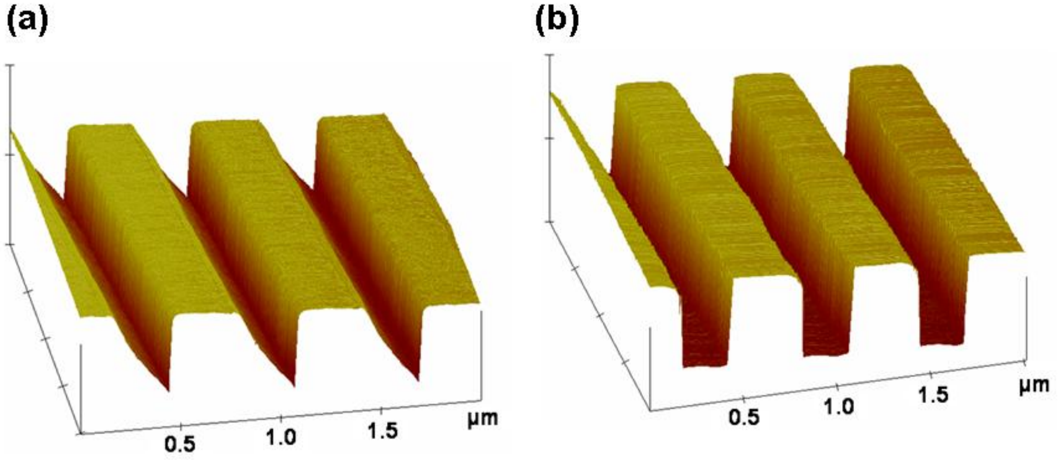

Figure 5.3 (a) AFM image of a PMMA line pattern by a conventional Si pyramid tip. (b) Image of the same PMMA pattern by a CNT tip.

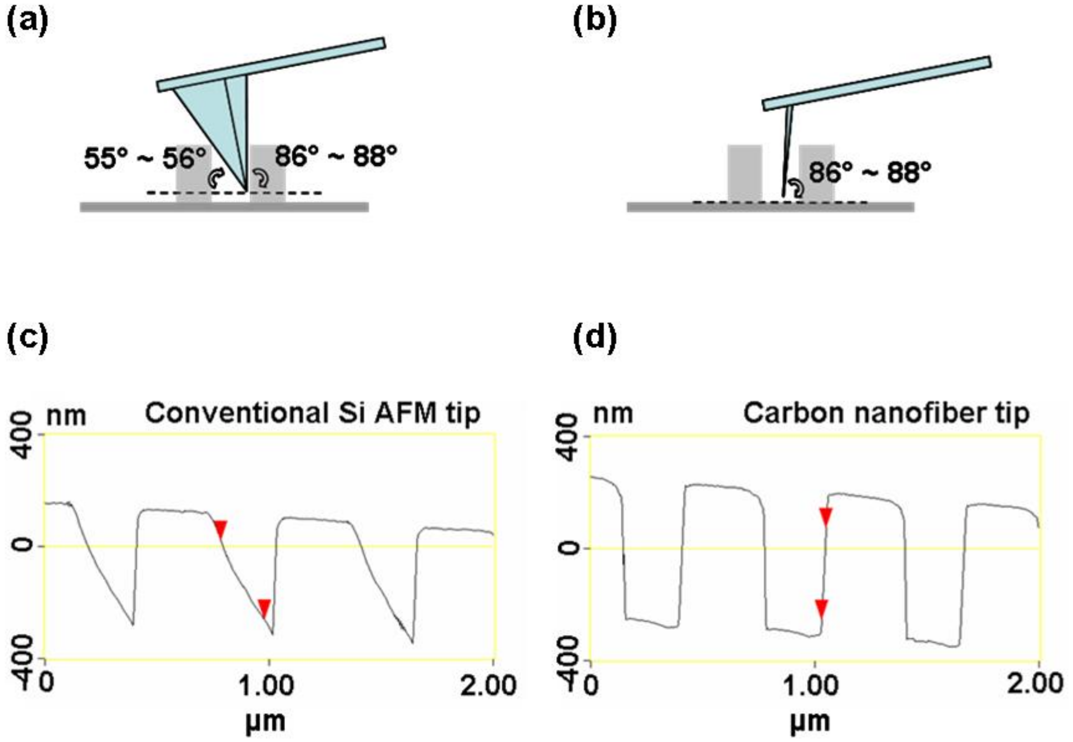

Figure 5.4 (a) Schematic of a Si probe scanning on a PMMA pattern. (b) Schematic of a CNT probe scanning on a PMMA pattern. (c) The height profile of Figure 5.3(a). (d) The height profile of Figure 5.3(b).

5.2.3 Tapping-mode imaging in liquid for stripped gold film surface

It has been reported that CNT probes are unable to obtain the stable images when operating in liquid. One possible reason is that a large acoustic vibration has to be applied to generate the cantilever oscillation, and thus causes serious disturbance to the CNT tip.[1] In order to test if the conical CNT probe is capable of reliably performing topographical imaging in liquid, we examined a template-stripped gold film placed in de-ionized water using a conventional fluid cell with Multimode AFM system (Veeco Instruments). The Au film had been exposed to the air for over one month without any treatment before using. In this experiment, a cantilever with a spring constant of ~ 3 N/m was chosen for CNT growth. Figure 5.5 shows a schematic diagram of AFM imaging in liquid with a conventional fluid cell. As shown in Figure 5.6(a), a clear image was acquired with the whole cantilever immersed in DI water. Compared with the image acquired by the Si probe, Figure 5.6(b), the CNT probe exhibits a better resolution. To the best of our knowledge, this is the first time that successful and reliable AFM imaging in liquid was performed using a CNT-related AFM probe in a conventional fluid cell. The better image resolution is possibly due to the larger base width of our conical CNT probes, which make the CNT probes more stable and diminish the disturbance by the surrounding liquid. However, more experiments have to be carried out to test the resolution of the CNT probe for AFM imaging in liquid.

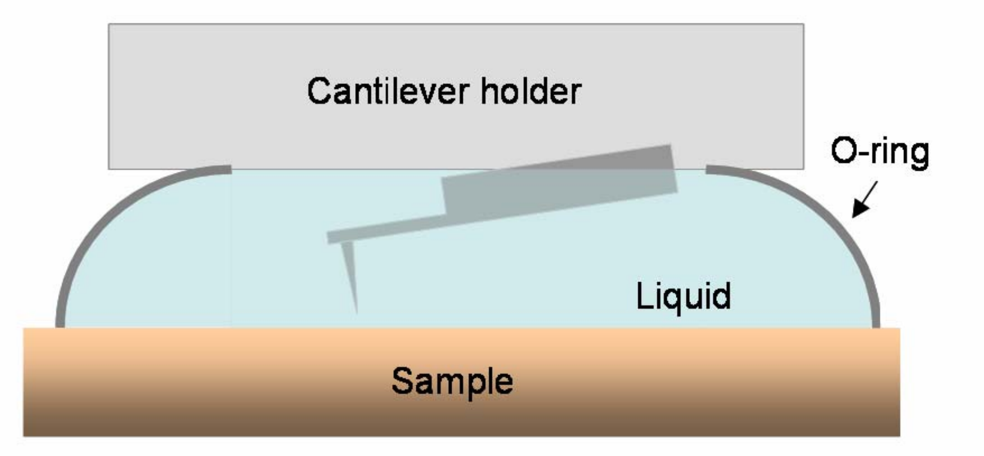

Figure 5.5 Schematic illustration of AFM operation in liquid with a conventional fluid cell.

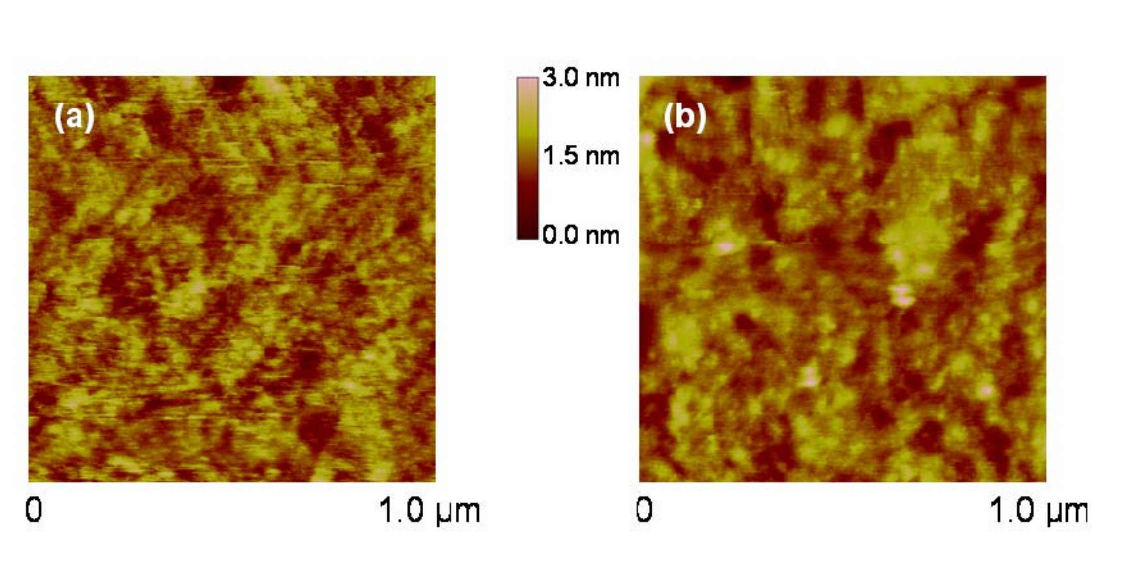

Figure 5.6 AFM tapping-mode images of a template-stripped gold film on the mica substrate in DI water using **(**a) A CNT probe, (b) A commercial Si probe.

5.3 Contact-mode imaging

5.3.1 Adhesive force between the tip and sample

Contact-mode AFM imaging where the AFM tip scans the sample in close contact with the surface is commonly used. The force on the tip is repulsive with a mean value of 10 $^{-9}$ N. Problems with contact mode are caused by excessive tracking forces applied by the probe to the sample. The effects can be reduced by minimizing the tracking force of the probe on the sample, but there are practical limits to the magnitude of the force that can be controlled during operation in ambient environments. Under ambient conditions, a thin water layer of 10-30 monolayers thick is present on the substrate surface. When the probe approaches and touches this layer, a meniscus forms between the probe tip and the substrate surface (as shown in a schematic illustration of Figure 5.7a), and thus a strong capillary force is generated. Due to such capillary condensation, the adhesive force between the tip and sample governs the force of the AFM tip, which reduces image resolution and induces image artifacts in AFM applications.

In order to obtain more reliable and accurate images in ambient conditions, a hydrophobic AFM tip is desirable, which can effectively reduce the adhesive force of the water. As indicated in Figure 5.7(b), when imaging with a hydrophobic tip, water will move near the point of contact between the tip and the sample surface, and thus the adhesion force becomes relatively weak. The commercial contact-mode probes made of hydrophilic silicon nitride could contribute strongly to the adhesion force. Several groups have tried to cover silicon nitride probes with a hydrophobic layer to improve the imaging performance.[2,3] However, these hydrophobic films may be worn down after long time scanning or increase the tip diameter and change the tip shape. Hence, the hydrophobic nature of CNT graphene sidewalls makes CNTs potentially good AFM tips for contact-mode imaging.

Figure 5.8 shows the optical microscope images of a 1 μL water droplet on the surface of a silicon nitride and CNT film. The CNT film was directly grown on a Ni coated Si substrate by DC-PECVD process. It has been reported that cleaned silicon nitride surfaces are much more hydrophilic than untreated one. The contact angle between the water and the untreated silicon nitride surface is around 70˚, as shown in Figure 5.8(a). As is evident from Figure 5.8(b), the contact angle between the water droplet and the CNT film surface is around 120˚, which indicates the CNT film is much more hydrophobic.

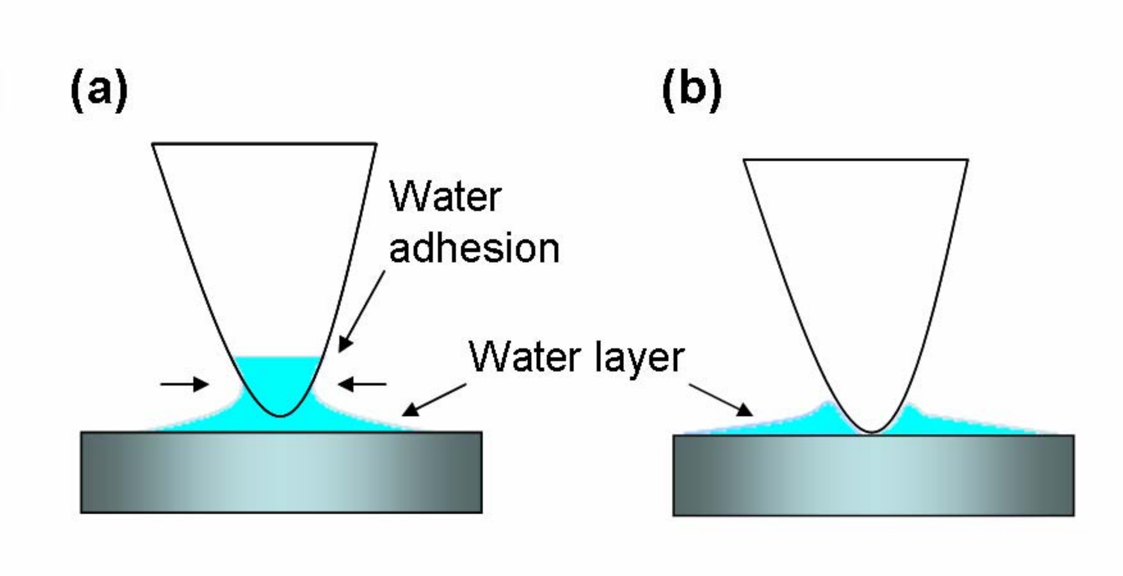

Figure 5.7 Schematic illustration of meniscus formation between the water layer and (a) A hydrophilic tip and (b) a hydrophobic tip.

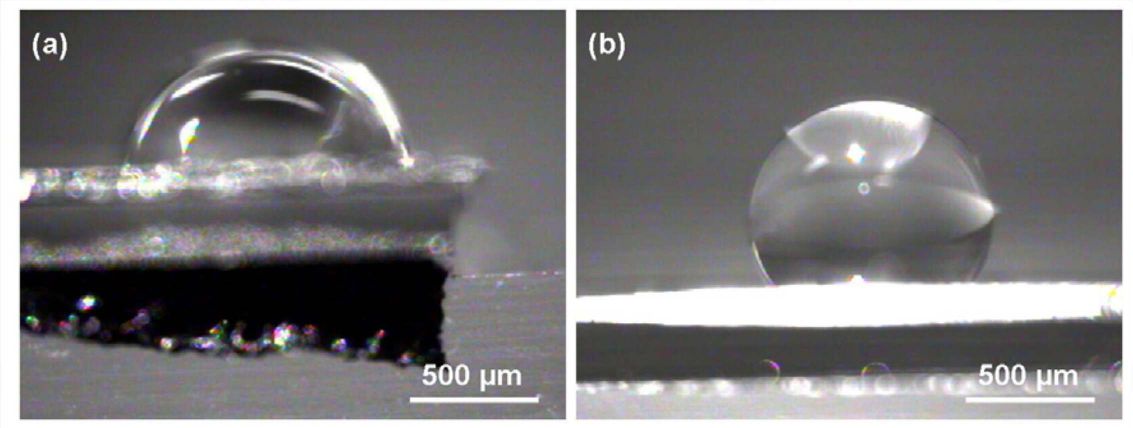

Figure 5.8 Optical microscope images of 1 µL water droplet placed on (a) A silicon nitride surface, (b) a CNT film surface.

In order to compare the adhesion force using a conventional silicon nitride probe and the CNT probe during AFM imaging, force-distance curve measurements were carried out on a silicon oxide surface in air. Force-distance curves are used to measure the vertical force that the tip applies to the sample surface. Thus, the measurements can reveal the attractive meniscus force as the piezo-scanner lowers and pulls up the tip. In the force-distance measurements, the tip is lowered to contact the surface, and then moved away from the surface, as shown in Figure 5.9.

The force-distance curves measured on a silicon oxide surface in air using a silicon nitride probe and CNT probe are shown in Figure 5.10 (a) and (b) respectively. The horizontal axis corresponds to the displacement of the tip, and the vertical axis represents the interaction force, which is converted from the change in cantilever deflection voltage. The tip approaching/separating steps of (a)–(d) marked in Figure 5.10 (a) are correspond to those in Figure 5.9 (a)–(d) respectively.

As the approaching force-distance curve (black) shown in Figure 5.10(a), the silicon nitride tip approaches the sample and is in contact with the surface at point 1 which is set as the zero displacement point. When the tip was pulled away from the surface, it does not leave the sample surface at point 1 until moving up ~ 40 nm at point 2 where the applied force of the cantilever overcomes the adhesive force. The adhesive force between the silicon nitride tip and the silicon oxide surface is around 4.7 nN.

Figure 5.10(b) shows a force-distance curve performed using a CNT probe. Due to the hydrophobic surface of CNTs, less adhesive force between the tip and the sample surface is expected. As indicated in Figure 5.10(b), the adhesive force is only 0.85 nN, less than one fifth of that of the silicon nitride probes. From the force-distance measurements, the single hydrophobic CNT probe was confirmed to effectively reduce the adhesive force. Hence, the CNT probe may be a good choice for contact-mode AFM imaging in air or high humidity conditions where the image distorts due to the water meniscus.

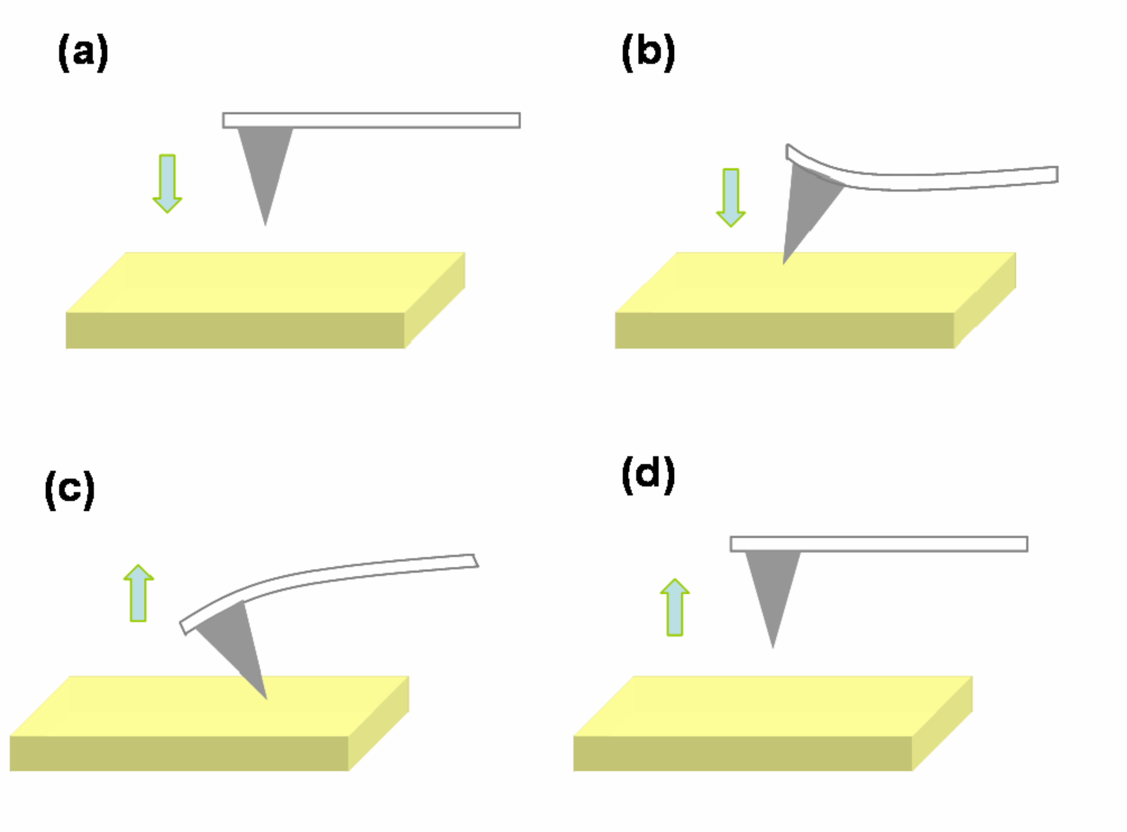

Figure 5.9 Schematic illustrations of steps of force-distance measurements. (a) The cantilever is undeflected when approaching the sample surface. (b) The cantilever is deflected away from the surface when touching the surface. The cantilever deflection is approximately linear as the tip continuously moves down. (c) As the tip is pulled away from the surface, the cantilever is bent towards the surface due to the attractive force of the water meniscus. (d) The cantilever springs free as the piezo-scanner retracts enough to a certain point.

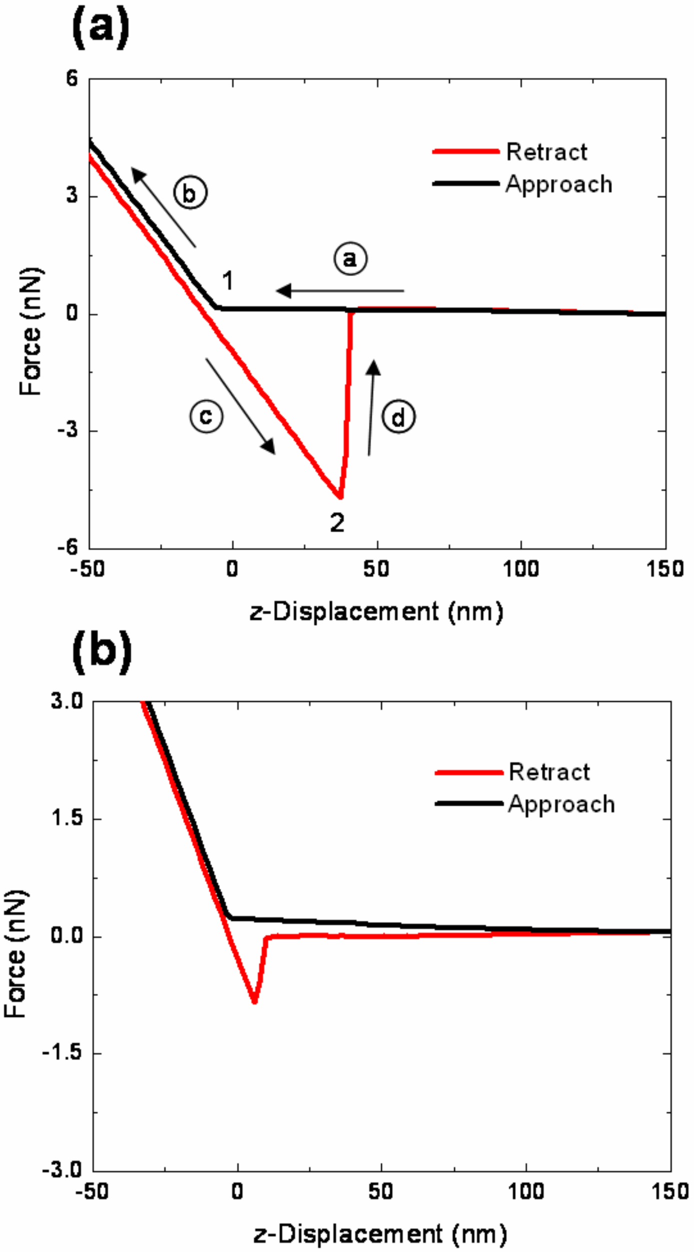

Figure 5.10 Force-distance curves measured on a silicon oxide surface in air with (a) a silicon nitride probe, (b) a CNT probe.

5.3.2 Contact-mode imaging on bimolecular samples

In order to test whether CNT probes can obtain contact-mode AFM images with better resolution, the imaging performance of the CNT probe was evaluated in air using a Dimension 3100 AFM. For surface metrology of biological samples, low stiffness AFM probe cantilevers, which allow low imaging forces, are desirable to minimize structural damage during scanning. As described in Chapter 4, by using a tunable PECVD growth technique, the surface stress of the low stiffness cantilevers can be controlled, and thus CNTs can be grown on flat and low stiffness cantilevers for contact-mode AFM imaging.

A cantilever with a spring constant of ~ 0.1 N/m was chosen for the measurements. The surface morphology of a bovine serum albumin (BSA) film on a freshly cleaved mica surface was examined using our CNT probes and compared with images taken by commercial silicon nitride contact-mode probes (NP series probes, Veeco), as shown in Figure 5.11(a) and (b). The BSA film was prepared by putting freshly cleaved mica into 0.1% BSA solution in phosphate buffered saline (PBS) and incubating for 20 min under 4 °C, and then drying in air. The blurred AFM image acquired by silicon nitride probe reveals that the probe can not trace the surface contour very well, as shown in Figure 5.11(b). As is evident from Figure 5.11(a), the CNT probe produces a clearer image with better lateral resolution than the silicon nitride probe. The improved image quality is revealed presumably due to the sharpness of the CNT tip and its hydrophobic surface, which can reduce the capillary force during imaging resulting in more accurate.

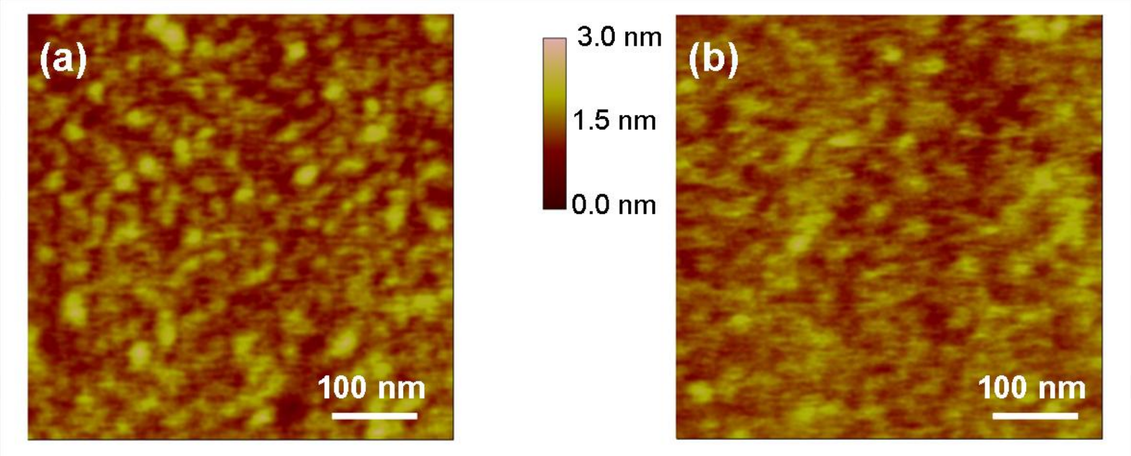

Figure 5.11 (a) AFM image of a bovine serum albumin (BSA) film by a CNT tip. (b) AFM image of the same BSA film by a commercial silicon nitride tip.

5.3.3 Contact-mode imaging on trench patterns

Another comparison between a CNT probe and a commercial silicon probe has been made by imaging an array of polymethyl methacrylate (PMMA) polymer resist pattern (600 nm trench line width, 250 nm spacing, and 350 nm thickness) on a Si substrate as shown in Fig. 5.12(a) and (b). Because of its high-aspect-ratio geometry, our CNT probe more accurately reveals the geometry of the PMMA patterns. On the other hand, the silicon nitride probe shows a misleading image due to the tip convolution from the pyramidal tip. As to the wear characteristics of CNT probes, we have shown the image quality, when operating in tapping-mode, is not degraded after 7 hours of continuous scanning on a silicon nitride film, which implies that the CNT probe is very durable. Further experiments are required to determine the durability of CNT probes operated in contact-mode.

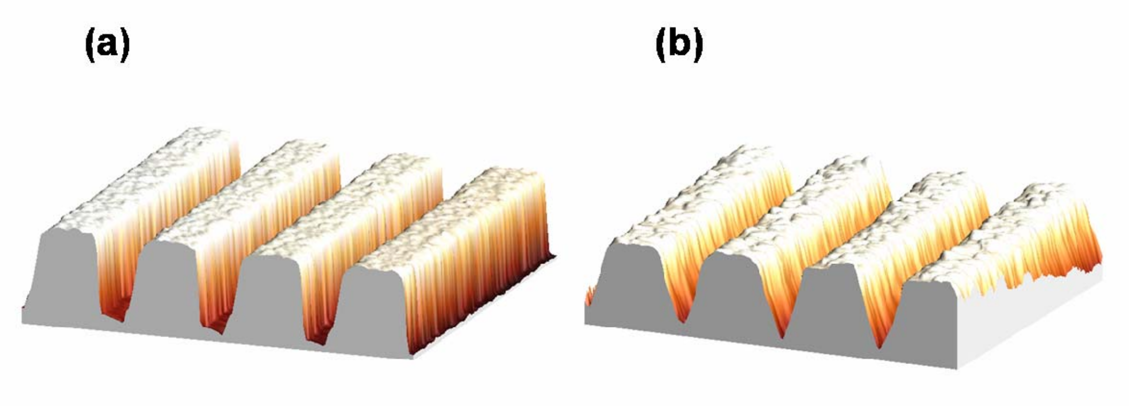

Figure 5.12 Contact-mode AFM images of a PMMA pattern taken by (a) a CNT probe and (b) a silicon nitride probe.

5.3.4 Application of a CNT array

In order to evaluate the mechanical sturdiness and adhesion strength of the CNT probe, a 10 by 10 periodic array of the CNT probes, Figure 5.13(a), was prepared by EBID patterning and DC-PECVD growth process, as described in Chapter 3. This bed-of-nail type CNT array was subjected to an AFM contact-mode imaging by a standard Si as well as a silicon nitride probe. As shown in Figure 5.13(b), the obtained image actually represents a detailed analysis of the three-dimensional shape of the silicon nitride pyramid probe itself due to the high-aspect ratio geometry and sharp tip of the CNT probes. In the contact-mode imaging, CNT probes did not show any obvious sign of breakage as confirmed by SEM examination afterwards. These results also confirm the strong adhesion of the CNT to the cantilever as well as the mechanical toughness of the CNT probe itself. The data in Figure 5.13(b) also shows an intriguing possibility of using the bed-of-nails CNT array for characterization/testing of other probes such as Si and silicon nitride pyramid tips, for example, as a means of screening probes with unsatisfactory tip sharpness or mechanical weakness.

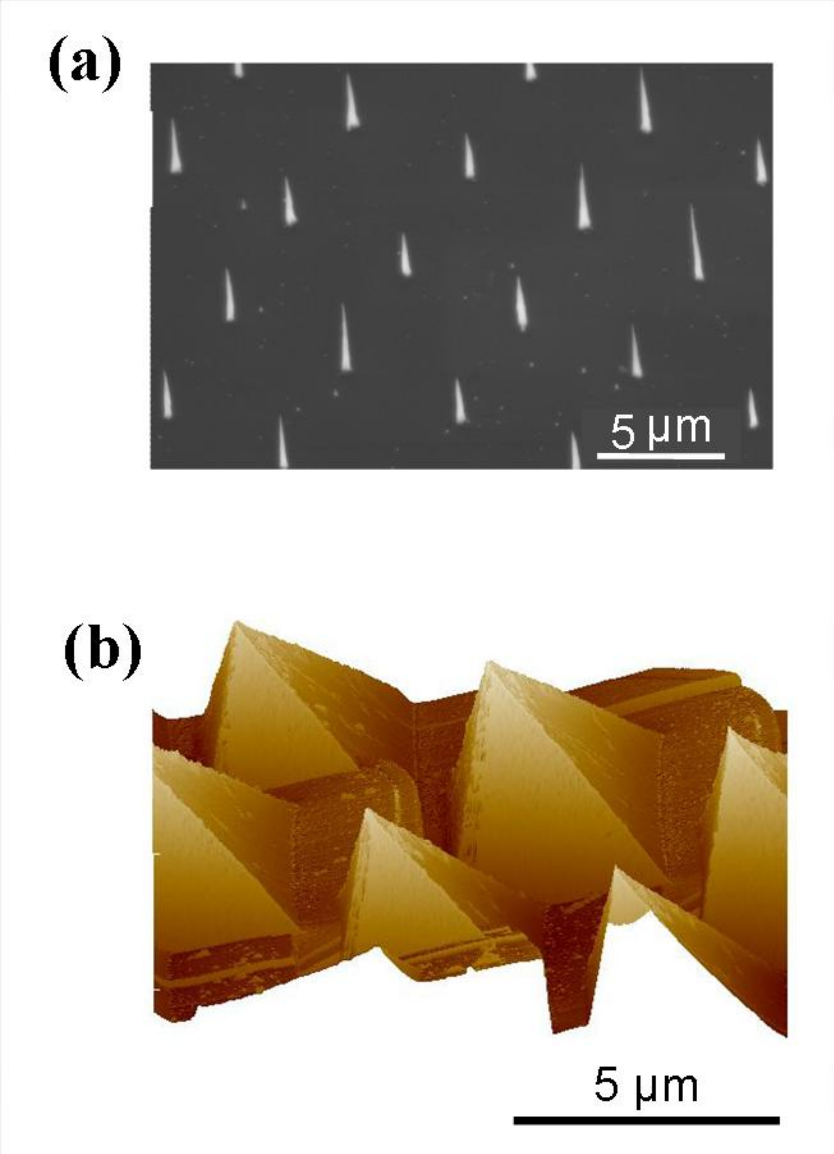

Figure 5.13 (a) SEM image of a periodic array of conical CNT probes fabricated by using the carbon-dot mask process. (b) Contact-mode AFM image of the CNT array acquired by a silicon nitride probe.

5.4 Durability of carbon nanotube probes

In order to test the mechanical durability of the CNT tip, a continuous scanning operation on a silicon nitride film (~ 5nm thick) sputtered on a Si substrate was carried out and the AFM image quality was evaluated as a function of operation time. Figure 5.14(a) and (b) shows the image of the silicon nitride film acquired after scanning for 30 min and 7 hours. In order to avoid the possible wearing of the sample, these two images were scanned on different area of the same film. As seen in Figure 5.14, the lateral resolution of the obtained AFM image was not noticeably changed even after 7 hours of operation. It was confirmed by comparing the grain size, roughness and height with analysis software for Nanoscope IIIa. By comparison, the Si based tips wore out rather easily and produced AFM images markedly deteriorated after a few hours of continuous operation.

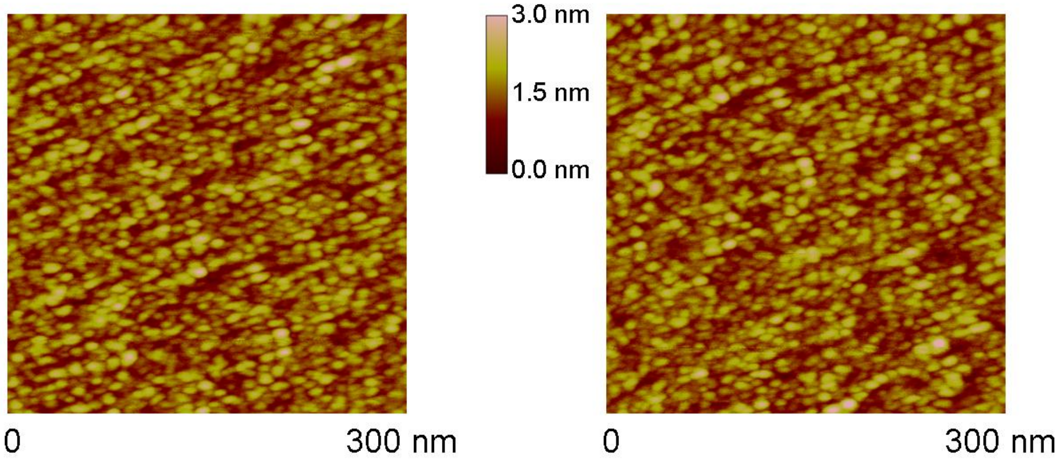

Figure 5.14 AFM tapping-mode images of a silicon nitride film on the Si substrate using a CNT probe. (a) Image acquired after 30 min scanning. (b) Image acquired after 7 hour scanning.

5.5 Application of metal-coated CNT probes in magnetic force microscopy

5.5.1 Introduction

Since the development of magnetic force microscopy (MFM) in 1987,[4,5] it has been widely used for study of magnetic recording media as well as other magnetic nanostructures. A conventional MFM probe which possesses a pyramidal tip is made of silicon with a ferromagnetic thin film coating. Due to its relative blunt and low aspect ratio tip, the image resolution is notably limited. To obtain images with a higher resolution, there have been several techniques developed for reducing the physical size of the magnetic material of the tip, such as focused ion beam (FIB) milled tips,[6,7] electron beam deposition (EBD) tips, [8,9] stencil-deposited metal dot on an AFM tip.[10] Recently, CNTs have been fabricated for MFM imaging either by mechanical attachment[11-13] or direct growth on commercial Si pyramid tips.[14] An iron catalyst-capped CNT attached to a pyramidal Si tip has been applied to show the similar image quality compared with conventional Si MFM probes.[11] Magnetic-metal-coated CNT tips which demonstrated 10-20 nm lateral resolution have been fabricated by sputtering magnetic films on CNTs either grown on a Si pyramid tip using thermal CVD[14] or mounted[12] on Si cantilevers. An iron-filled CNT has also been produced to acquire MFM images.[13]

In this study, we have investigated the performance of CNT MFM probes directly fabricated on tipless cantilevers using DC-PECVD process followed by coating and annealing of a high coercivity Iron-platinum film. The probe fabrication process is amenable for integration into conventional semiconductor process for mass production. The CNT probe tip possesses high-aspect-ratio geometry which can reduce magnetic volume on the tip, hence increase the spatial resolution of MFM images, and is also allowed to acquire topographical and MFM images inside deep structures.

5.5.2 Principles of magnetic force microscopy

MFM is one of the extended AFM imaging techniques that can map the spatial distribution of magnetism by measuring the magnetic interaction between a magnetic tip and sample. Since the magnetic interaction force depends on the distance between the tip and the sample, it is necessary to separate the MFM imaging from the topography. Hence, MFM imaging is executed by a two-pass method. Figure 5.15 shows the schematic illustrations of MFM measurements. In the first pass, the surface topography is measured in tapping-mode or contact-mode. As shown in Figure 5.15(b), in the second pass, the tip is lifted to a user defined height from the sample surface and scanned by using the stored topography obtained from the first pass, while maintaining a constant height separation.

In the MFM imaging, two basic detection modes can be applied which are sensitive to two different types of interaction. The static (or DC) mode detects the magnetic force acting on the tip whereas the dynamic (or AC) mode measures the force derivative. The comparisons of the static and dynamic mode through either theoretical calculations or experiments indicate that the dynamic mode is favorable for high resolution MFM imaging. Thus, the dynamic mode was chosen in this study.

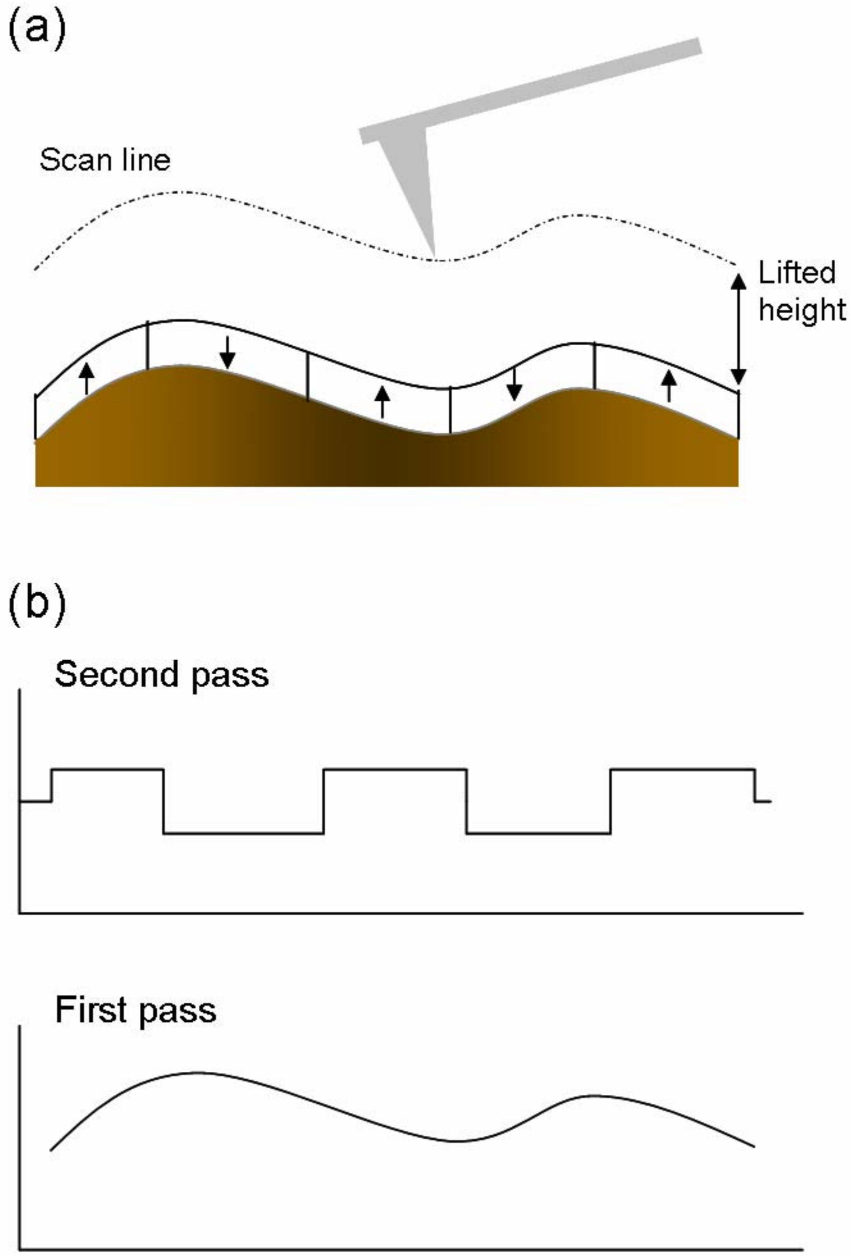

Figure 5.15 Schematic illustrations of magnetic force microscopy measurements.

In the dynamic mode, the cantilever is oscillated at or close to its resonance frequency. The cantilever can be treated as a harmonic oscillator which have the resonance frequency f,[15]

$$f = \frac{1}{2\pi}\sqrt{\frac{C_{eff}}{m}} \quad \text{(Hz)}$$

where m is the effective mass[16] of tip and cantilever. The effective cantilever constant C_{eff} is given by

$$C_{eff} = C - \frac{\partial F}{\partial z} \quad \text{(N/m)}$$

where c is the cantilever constant. When the tip is in the close proximity to the sample surface, the forces acting on the magnetic tip change when the distance between tip and sample is changed. This can be described by a force derivative $\partial F/\partial z$. This force derivative on the tip acts on the cantilever just like an additional cantilever constant. For low amplitudes, $\partial F/\partial z$ can be assumed as a constant, so that the cantilever with the tip interacting with the sample can still be treated as a harmonic oscillator:

$$f = \frac{1}{2\pi}\sqrt{\frac{C - \partial F / \partial z}{m}} \quad \text{(Hz)}$$

The equation can be re-written as the following form which can show that a force derivative $\partial F/\partial z$ changes the resonant frequency of the cantilever to

$$f = f_0\sqrt{1 - \frac{\partial F / \partial z}{C}} \quad \text{(Hz)}$$

with f_0 the free resonance frequency of the cantilever in the case of no tip-sample interaction.

The magnetic potential E between the tip and the sample is given by

$$E = \mu_o \int \vec{M}_{tip} \cdot \vec{H}_{sample} dV_{tip} \quad \text{(Joule)}$$

where $\mathbf{M}_{tip}$ is the magnetization of the tip, $\mathbf{H}_{sample}$ is the stray field of the sample and V_{tip} is the volume of the magnetic part of the tip. The force **F** acting on a MFM tip can thus be expressed by

$$\vec{F} = -\nabla E = -\mu_o \int \nabla(\vec{M}_{tip} \cdot \vec{H}_{sample}) dV_{tip} \quad \text{(N)}$$

5.5.3 Advantages of high-aspect-ratio probes

Since the magnetic interaction is long range, therefore, a major part of the tip is responsible for MFM imaging. As can be found in magnetic recording readback, the MFM response shows an exponential decay e^{-kz} with increasing tip sample separation.[15] Thus, the interaction decreases with increasing distance, and one can take into consideration only the effective portion of the tip of length, ignoring the effect of its remaining part, as shown in Figure 5.16. One of the most critical parts of the MFM is the probe, which may affect the image resolution and contrast through the tip shape or its magnetic part.[17,18]

As indicated in Figure 5.16(a), a magnetic film coated probe with a high-aspect-ratio geometry and sharp tip can have smaller volume of the magnetic material contributing to the interaction, and thus high spatial resolution MFM images can be obtained. On the other hand, for the probe with larger cone angle, the stray field from the magnetic material on the sidewalls has much more contribution in the signal and reduces the resolution, as shown in Figure 5.16(b). As to the properties of the magnetic material on the probe, the magnetization distribution over the volume of its magnetic part can be an important factor.[19,20]

As were noted above, the requirements for high-resolution MFM probes are a well-defined magnetization direction and small stray fields. In this study, a FePt coated CNT probes were developed for high resolution MFM imaging. The high aspect ratio geometry and the sharp tip of the CNT probes can effectively reduce the stray field and also allow a better topographic imaging. A well-defined magnetization direction is achieved by coating with a highly coercive FePt magnetic film, which also assures that the magnetization direction of the tip remains undisturbed by high stray field samples.

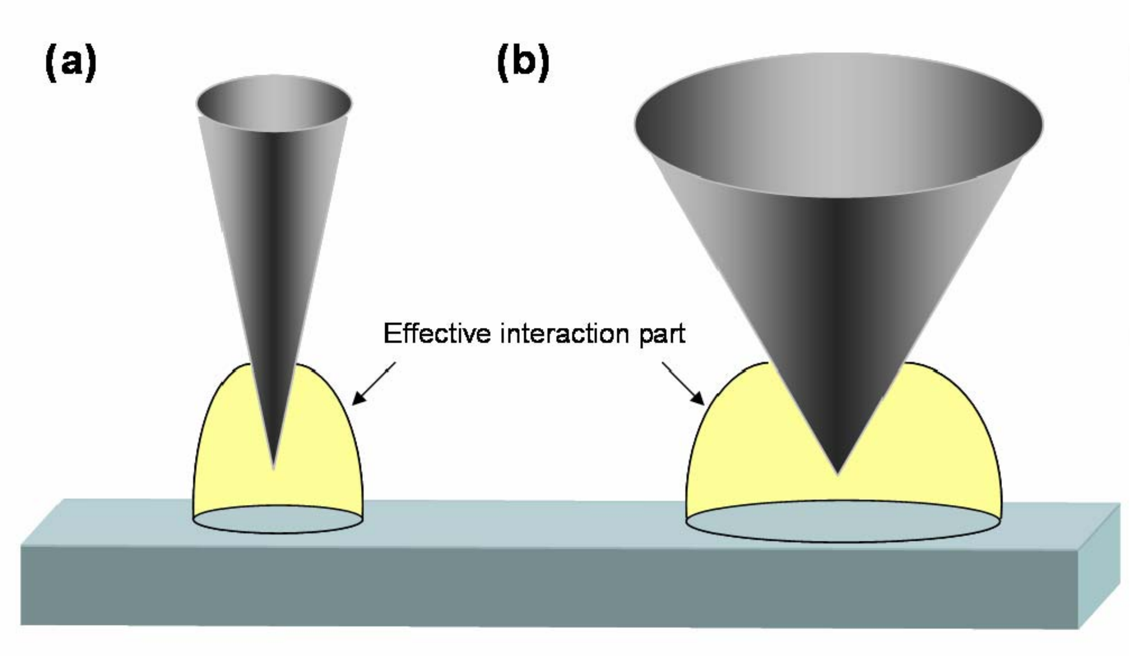

Figure 5.16 Schematic illustrations of the effective portions of magnetic interaction in MFM measurements with (a) a tip with a small cone angle and (b) a tip with a large cone angle.

5.5.4 Imaging magnetic recording media with metal-coated CNT probes

The CNT probes on tipless cantilevers were fabricated using EBID patterning technique and DC-PECVD growth method. The detailed process of CNT probes were described in Chapter 3. The FePt film of 30 nm thickness was sputtered onto the grown CNT probe and annealed at 650°C for 2 hr to form tetragonal $L1_0$ phase. The spring constant and resonance frequency of the selected cantilevers utilized in this study are about 42 N/m and 330 kHz, respectively. The fabricated CNT probe was evaluated on MFM imaging under ambient conditions by using a Digital Instruments D3000 AFM operated in tapping/lift mode with Nanoscope IIIa controller.

A single, as-grown CNT probe at the edge of a tipless cantilever is shown in Figure 5.17. By controlling the electric field direction during the PECVD growth, the CNC was intentionally grown ~13˚ tilted from the cantilever surface normal in order to compensate the operation tilted angle of the cantilever. The tip radius of the as-grown CNT probe is ~5 nm. After deposition and annealing of FePt film, FePt nanoparticles were formed on the CNT probe. The tip radius of the coated CNT probe becomes ~25 nm, as shown in the inset of Figure 5.17. The magnetization direction of the FePt particles on the tip can be well controlled and maintained due to the high magnetic anisotropy of $L1_0$ FePt phase. It has been reported that the magnetic materials within 250 nm away from the sample contribute strongly to the signal.[14] Since the length of the CNT probe is long enough (>2 μm), the interaction between the magnetic film on the cantilever and the test sample is negligible compared to the interaction between the tip and the sample.

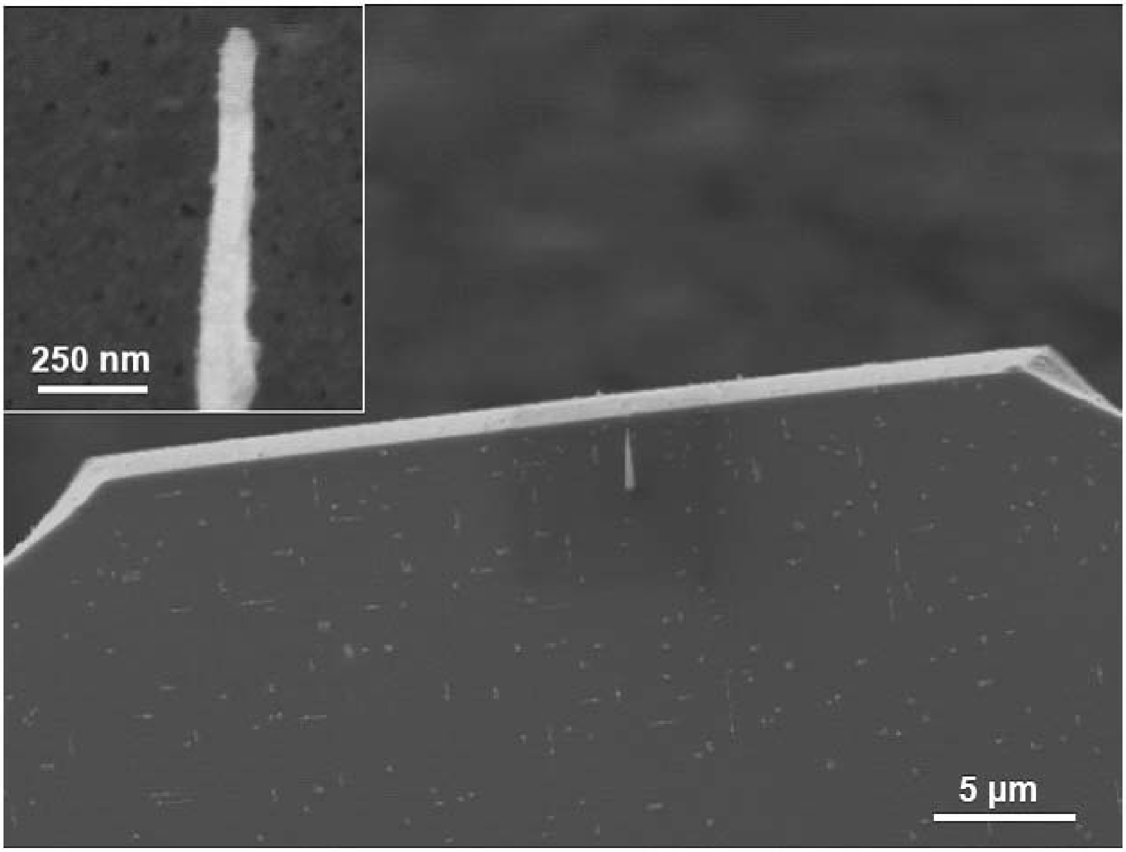

Figure 5.17 SEM image of a single as-grown CNT probe on a tipless cantilever. Inset: high-magnification SEM image of the CNT tip.

To evaluate the performance of CNT MFM probes fabricated in this study, MFM images were obtained and compared with those acquired using a commercial pyramidal Si probe deposited with the identical FePt film. A high-density CoCrPt:SiO/Ru perpendicular magnetic recording medium with density from 700 to 900 kilo flux changes per inch (kfci) was chosen as a test sample. Figures 5.18(a) and (b) show the comparative MFM images of the three different tracks obtained using the FePt-coated Si probe and the CNT probe, respectively. Obviously, the MFM image obtained from the CNT tip reveals much clearer magnetic domain structure characteristics, especially on higher track densities of 800 and 900 kfci.

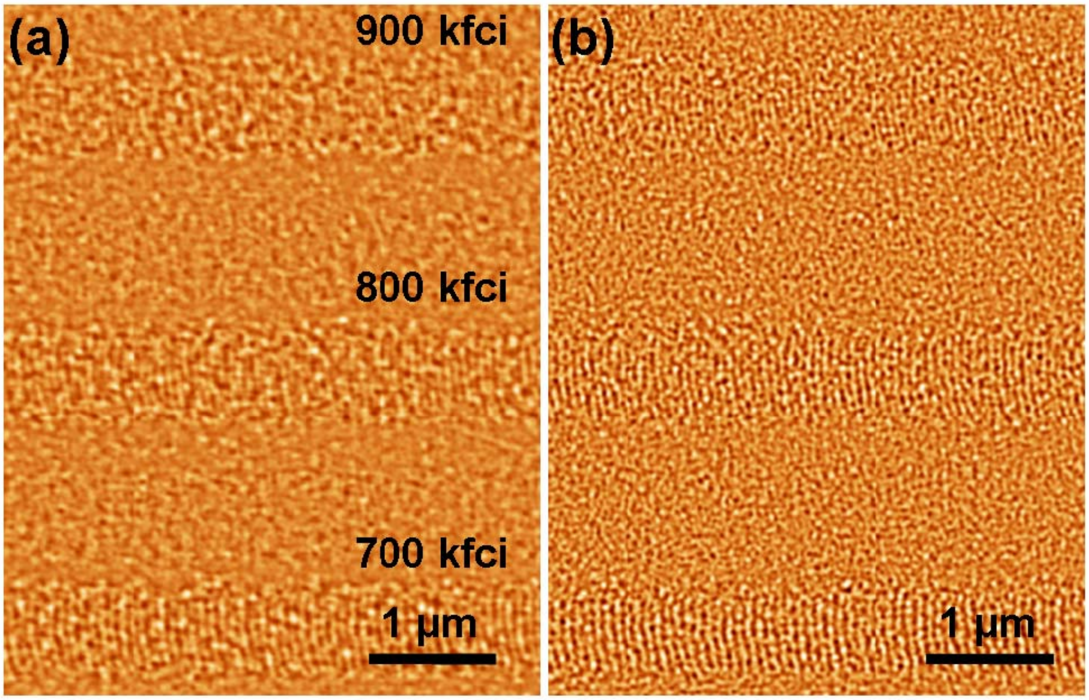

Figure 5.18 Phase images of 700, 800 and 900 kfci recording media track obtained by (a) the Si MFM probe, and (b) the CNC MFM probe.

The detailed MFM images of the 900 kfci track taken with the FePt-coated Si and CNT probes are shown in Figure 5.19(a) and (b), respectively. Compared to the Si probe, the CNT probe provides much sharper images with a significantly improved resolution. The major portion of the magnetic moment of the probe mostly comes from the apex. However, the magnetic dipole interaction is a long-range interaction that includes not only the contribution between the sample and the magnetic material near the tip but also that from extended areas of the tip. Therefore, such an improved image resolution is believed to be the result of a small cone angle of the CNT tip, which reduces lateral magnetic interaction volume on the sidewall of the CNT tip. Another significant and worth noting advantage is that a shorter tip-sample spacing is allowed in the case of our FePt-coated CNT probe without degrading the resolution, which can enhance the contrast as well as the ability to trace the surface topography of the sample. This is primarily due to the high aspect ratio and sharp tip geometry of the CNT probes in general.

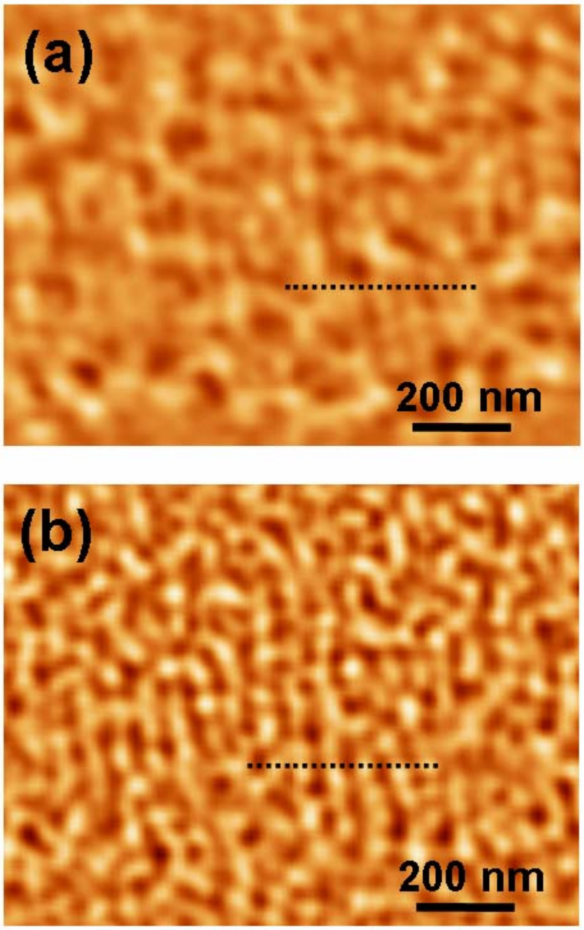

Figure 5.19 Zoom-in MFM image of the 900 kfci track taken with (a) the Si probe and (b) the CNT probe.

5.5.5 Analysis of the MFM images obtained by metal-coated CNT probes

In order to understand if the CNT MFM probe can acquire correct information of the magnetic domain structures, the power spectra of average MFM image profiles of the recording media tracks obtained by the CNT probe were examined. The analyzed area is selected from the recorded bit area parallel to the track direction. Each spectrum was converted from ten 5 μm long line-profiles of magnetic recording patterns by fast Fourier transformation, and then normalized to its maxima in order to compare the strength of different spectra.

Figure 5.20 shows the power spectra of 700-900 kfci tracks plotted against the frequency. The inverse number of the peak position indicates the period of the bit length, which is double the length of the magnetic flux change by definition. As expected, the highest peak in the spectrum occurring at the write frequency shifts to a higher value as the recording density increases. As shown in Figure 5.20, the peak position in each spectrum corresponds to the wavelength (λ) of 78.8 nm, 69 nm and 61.2 nm (i.e., 39.4, 34.5 and 30.6 nm/flux change respectively). Compared with the ideal peak positions of tracks of 700, 800 and 900 kfci corresponding to 36, 32 and 28 nm, the data acquired by the CNT MFM probe is pretty close to the expected values.

As the recording density increases, the signal/noise ratio decreases from 9.17 of 700 kfci to 5.44 of 900 kfci. The noise in MFM imaging may be due to the effects of thermal drift or environmental noise,[21,22] and can be reduced by operating the imaging under lower temperature, which may enhance the image resoltuion.[23]

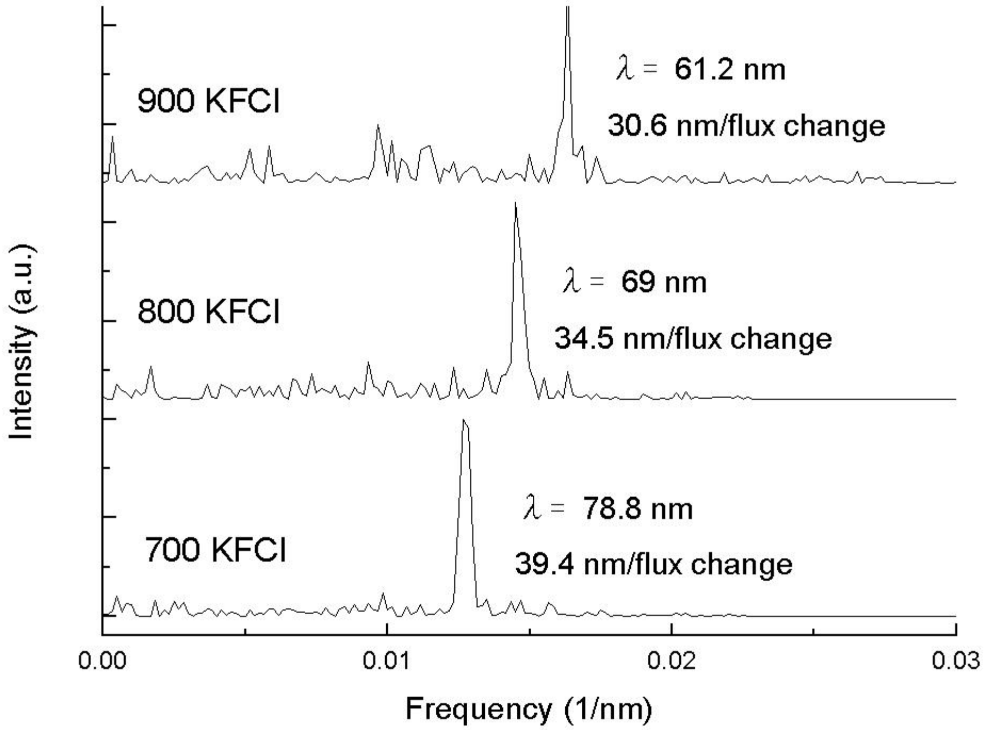

Figure 5.20 Power spectra of the averaged line profile of phase images taken with the CNC MFM probe.

The resolution of the MFM can be characterized in real space by its “point response”[24] or in Fourier transform space by its wave-vector (spatial frequency) response.[15,25] In Figure 5.21, the image resolution was characterized by measuring the full width at half maximum (FWHM) response of small features, which corresponds to the real space resolution. Dash-lines marked in the phase images of Figure 5.19(a) and (b) were chosen to show the line-profiles of the same position in the 900 kfci track image taken with Si and CNT probes, respectively. The CNT probe demonstrates a resolution of ~20 nm FWHM, as shown in Figure 5.21(b). On the other hand, a rather irregular line-profile is produced by the Si probe as shown in Figure 5.21(a), which indicates a poor image quality. On the Si probe tip, more magnetic materials around the tip end area due to its lower aspect ratio pyramidal geometry. The contribution of those surrounding magnetic materials increases the phase shift and decreases the resolution.

In this work, a Fourier transform method was also used to evaluate the MFM resolution. Through this method, we can define λ_c, a cutoff frequence, corresponding to the minimum detectable wavelength, as the MFM resolution.[15] The response of the MFM is a function of spatial frequency components in the stray field. Such a response curve is called the tip transfer function (TTF). For example,[15] a slab-like tip with a magnetic coating on one side is characterized by the transfer functions

$$\vec{F}(k,z) = -\frac{\alpha_0 M_{sam} M_{tip}}{k} e^{-kz}(1-e^{-kt}) \times \sin(\frac{kb}{2})(1-e^{-kl}) \qquad \text{(N)}$$

$$\vec{F}'(k,z) = -\alpha_0 M_{sam} M_{tip} e^{-kz}(1-e^{-kt}) \times \sin(\frac{kb}{2})(1-e^{-kl}) \qquad \text{(N)}$$

Where M_{sam} and M_{tip} are the moments of the sample and the tip, respectively, k is the spatial frequency, z is the tip-sample distance; t is the thickness of the sample film, b and l are the magnetic coating thickness and length of the tip.

The MFM response is proportional to the magnetization of tip and sample. It has an exponential decay e^{-kz} with increasing tip-sample separation. The factor $(1 - e^{-kt})$ describes the thickness loss, resulting from the superposition of the stray fields of the magnetic charge sheets on the top and the bottom side of the measured layer. The term $(1 - e^{-kl})$ describes the low-frequency behavior of the MFM.[15] The *sin(kb/2)* term establishes another limit for high-resolution detection and means that the transfer function is zero at $n\lambda = b$. The MFM response drops below the background level (noise level) below this wavelength, which is the minimum detectable wavelength, also called cutoff wavelength, by the MFM. The MFM resolution is defined as the half of the cutoff wavelength.

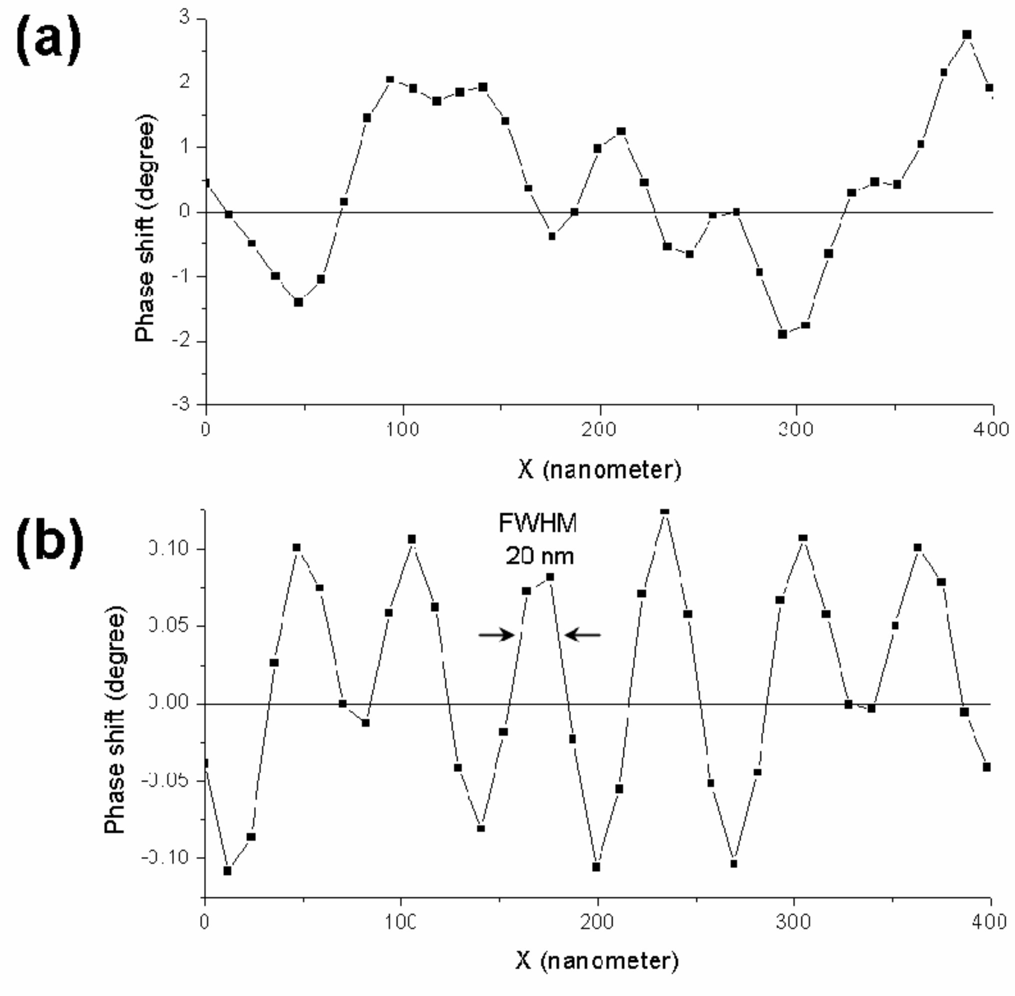

Figure 5.21 Section profile of a 900 kfci track by (a) a FePt-coated Si probe and (b) a FePt-coated CNT probe.

Figure 5.22 shows the power spectra (in log scale) of the three different magnetic density tracks. For the 700 kfci tracks, as shown in Figure 5.22(a), a cutoff wavelength of 34 nm corresponding to the MFM resolution of 17 nm is obtained from the intersection of the signal and the noise lines. For the 800 and 900 kfci tracks, the resolutions obtained from the cutoff wavelengths are 17.5 and 18 nm, respectively, as shown in Figure 5.22(b) and (c). The error of the resolution is about 2 nm, which is due to the inaccuracies of drawing the signal line and the noise line. The MFM resolutions obtained from three tracks are similar and consistent with the result by measuring the FWHM of the MFM signals, as shown in Figure 5.21(b).

Here, we show some example MFM results from CNT probes. It is necessary to further optimize the tip radius, thickness of magnetic coating and select cantilevers with moderate resonant frequency in order to obtain an optimum compromise between image contrast and resolution. Further improvement in the specifics of FePt deposition and related fabrication processes is likely to yield a sharper MFM probe and higher resolution.

5.6 Acknowledgments

The parts of the following papers were selected as the content of this study: “Extremely Sharp Carbon Nanocone Probes for Atomic Force Microscopy Imaging”, I.-C. Chen, L.-H. Chen, X.-R. Ye, C. Daraio, S. Jin, C. A. Orme, A. Quist and R. Lal, Applied Physics Letters 88, 153102 (2006), “Fabrication of high-aspect-ratio carbon nanocone probes by electron beam induced deposition patterning”, I.-C. Chen, L.-H. Chen, C. A. Orme, A. Quist, R. Lal and S. Jin, Nanotechnology 17, 4322 (2006),

"Control of curvature in highly compliant probe cantilevers during carbon nanotube growth", I.-C. Chen, L.-H. Chen, C. A. Orme and S. Jin, Nano Letters (in press) and "Iron-platinum coated carbon nanocone probes on tipless cantilevers for high resolution magnetic force imaging", I.-C. Chen, L.-H. Chen, A. I. Gapin, S. Jin, L. Yuan and S.-H. Liou, Nanotechnology (Submitted). The dissertation author was the primary investigator and author of these papers.

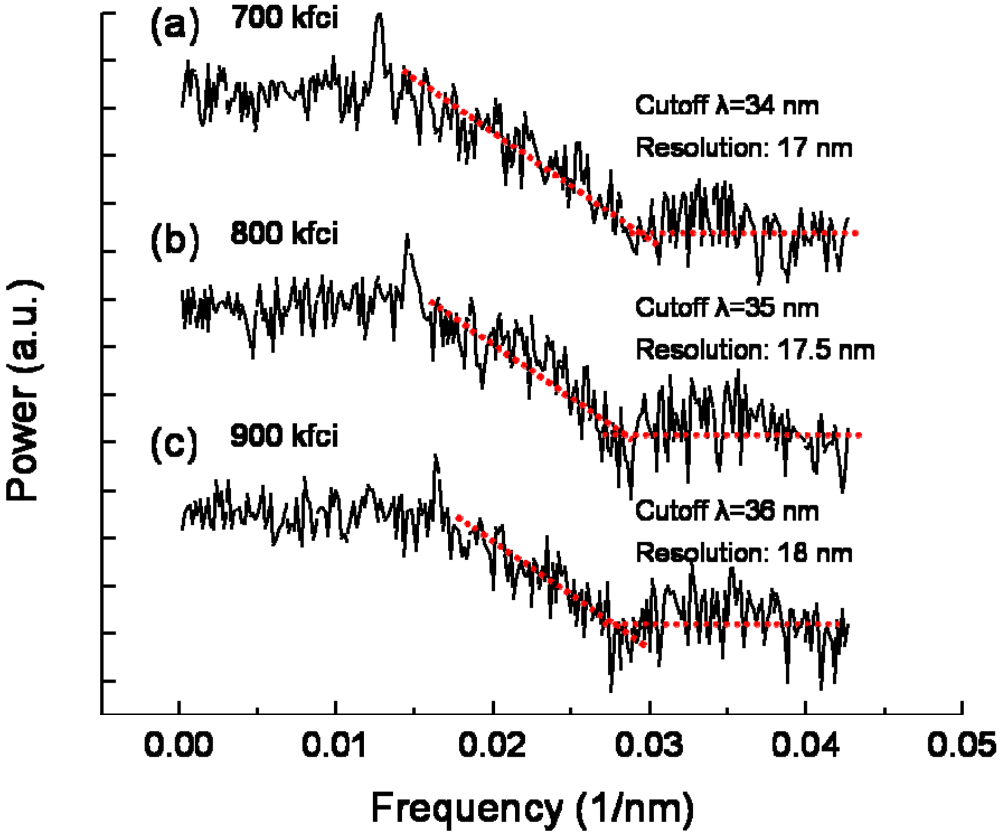

Figure 5.22 MFM resolution analysis by the power spectra of the line profiles of phase images taken with the CNC MFM probe.

5.7 References

[1] J. Li, A. M. Cassell and H. Dai, *Surf. Interface Anal.* **28**, 11 (1999).

[2] R. D. Piner, S. Hong and C. Mirkin, *Langmuir* **15**, 5457 (1999).

[3] H. Knapp and A. Stemmer, *Surf. Interface Anal.* **27**, 324 (1999).

[4] Y. Martin and H. K. Wickramasinghe, *Appl. Phys. Lett.* **50**, 1455 (1987).

[5] J. J. Sáenz, N. García, P. Grütter, E. Meyer, H. Heinzelmann, R. Wiesendanger, L. Rosenthaler, H. R. Hidber, and H. J. Güntherodt, *J. Appl. Phy.* **62**, 4293 (1987).

[6] G. N. Phillips, M. Siekman, L. Abelmann, and J. C. Lodder, *Appl. Phys. Lett.* **81**, 29 (2002).

[7] L. Gao, L. P. Yue, T. Yokata, R. Skomski, S. H. Liou, H. Takahoshi, H. Saito, and S. Ishio, *IEEE Trans. Magn.* **40**, 2194 (2004).

[8] G. D. Skidmore and E. D. Dahlberg, *Appl. Phys. Lett.* **71**, 3293 (1997).

[9] Y. M. Lau, P. C. Chee, J. T. L. Thong, and V. Ng, *J. Vac. Sci. Technol. A* **20**, 1295 (2002).

[10] A. R. Champagne, A. J. Couture, F. Kuemmeth, and D. C. Ralph, *Appl. Phys. Lett.* **82**, 1111 (2003).

[11] N. Yoshida, M. Yasutake, T. Arie, S. Akita, and Y. Nakayama, *Jpn. J. Appl. Phys.*, Part 1 **41**, 5013 (2002).

[12] H. Kuramochi, T. Uzumaki, M. Yasutake, A. Tanaka, H. Akinaga, and H. Yokoyama, *Nanotechnology* **16**, 24 (2005).

[13] A. Winkler, T. Mühl,. S. Menzel, R. Kozhuharova-Koseva, S. Hampel, A. Leonhardt, and Bernd Büchner, *J. Appl. Phys.* **99**, 104905 (2006).

[14] Z. Deng, E. Yenilmez, J. Leu, J. E. Hoffman, E. W. J. Straver, H. Dai, and K. A. Moler, *Appl. Phys. Lett.* **85**, 6263 (2004).

[15] S. Porthun, L. Abelmann, and J. C. Lodder, *J. Magn. Magn. Mater.*, **182**, 238 (1998).

[16] D. Sarid, *Scanning Force Microscopy: with Applications to Electric Magnetic and Atomic Forces*, Oxford Series on Optical Sciences 2, 2nd edn., Oxford University Press, New York (1991).

[17] P. Grütter, D. Rugar, H. J. Mamin, *et al.*, *J. Appl. Phys.* **69**, 5883 (1991).

[18] D. V. Ovchinnikov and A. A. Bukharaev, *Tech. Phys*. **46**, 1014 (2001).

[19] S. L. Tomlinson, S. R. Hoon, A. N. Farley, *et al.*, *IEEE Trans. Magn.* **31**, 3352 (1995).

[20] P. Rice and S. E. Russek, *J. Appl. Phys.* **85**, 5163 (1999).

[21] C. Schonenburger and S. F. Alvarado, *Rev. Sci. Instrum.* **60,** 3131 (1989).

[22] M. J. Cunningham, S. T. Cheng and W. W. Clegg, *Meas. Sci. Technol.* **5** 1350 (1994).

[23] H. Saito, R. Sunahara1, Y. Rheem and S. Ishio, *IEEE Trans. Magn.* **41**, 4394 (2005).

[24] D. Rugar, H. J. Mamin, P. Guethner, S. E. Lambert, J. E. Stern, I. Mc-Fadyen, and T. Yogi, *J. Appl. Phys.*, **68**, 1169 (1990).

[25] H. J. Jug, B. Stiefel, P. J. A. van Schendel, A. Moser, R. Hofer, S.Martin, J. J. Guntherodt, S. Porthum, L. Abelmann, J. C. Lodder, G. Bochi, and R. C. Ohandley, *J. Appl. Phys.*, **83**, 5609 (1998).

CHAPTER 6: CONCLUSIONS AND FUTURE WORK

In summary, the fabrication of a sharp and high-aspect-ratio carbon nanotube probe which possesses desirable thermal stability and mechanical toughness has been demonstrated using resist-free EBID pattering of catalyst nano-dots and electric-field-guided DC-PECVD growth. By adjusting the dc bias between the cathode and anode, the geometry of CNT can be changed from tube-like to conical shape, and the catalyst particle on the CNT tip can be completely removed via time-dependent size reduction by plasma sputtering, thus leading to an extremely sharp tip which can be used for AFM imaging and deep profile analysis. This process which allows easy fabrication of a single nanoprobe on the commercial tipless cantilever is also capable of being integrated into batch production.

I also demonstrated that a high-aspect-ratio CNT probe on a very compliant and low-stiffness AFM probe cantilever can be fabricated using a tunable PECVD process of adjusting hydrogen/ammonia gas ratio in CNT growth and manipulating the surface stress conditions.

High resolution AFM and MFM imaging were demonstrated using fabricated CNT based probes. Compared with commercial Si probes, CNT probes can produce better lateral resolution and reduce tip convolution effect in AFM imaging, and have good stability after prolonged scanning. The MFM images taken with the FePt-coated CNT probe also show better resolution due to the high-aspect-ratio geometry and small radius of the tip.

Based on the fabrication techniques developed in this thesis, new CNT based probes can be further developed for nanotech and biotech related applications. Here, I will show two examples. First, the new MFM CNT based probes can be fabricated using high coercivity metal alloys as catalyst particles for CNT growth. The brief fabrication procedures are illustrated in Figure 5.1. By using EBID catalyst pattering technique and controlling sputtering etch to reduce the particle size during PECVD growth described in chapter 3, magnetic particle-capped CNT probes can be obtained for MFM imaging. Compared with the magnetic-film-coated CNT probe, the magnetic moment only comes from the magnetic nanoparticle on the top of the tip. Thus, the magnetic interactions between the sidewalls of the probe and sample can be significantly reduced, and the image resolution is expected to be improved.

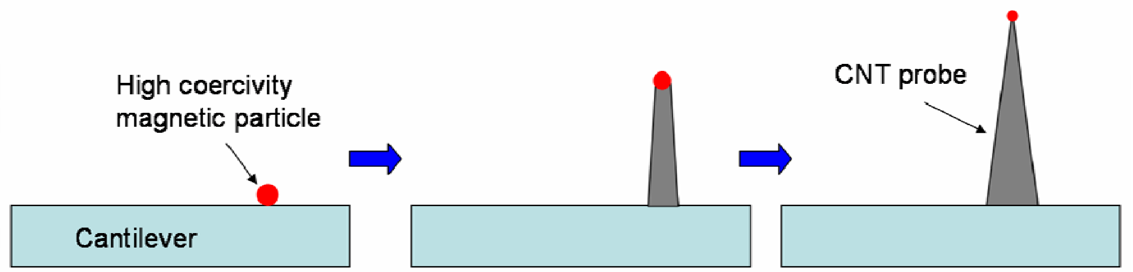

Figure 6.1 Schematic illustration of the fabrication steps of a CNT probe with a capped magnetic nanoparticle.

Second, the nanoprobes for measurements of bio-conductance or chemical reactions can be fabricated using CNTs with insulator coating, as shown in Figure 5.2. The conducting probes for chemical or biological reaction measurements have to be fabricated on low stiffness cantilevers, and whole body of the probe needs to be coated with an electrical insulator film except at the very end of the tip, so that the measurement current does not diverge or leak through the fluid environment.

CNTs have excellent conductivity and electrochemical behavior, and also can be functionalized with other chemicals, which make CNTs a potentially versatile electrode material for electrochemistry applications. In this thesis, fabrication of CNT probes on low stiffness cantilevers has been demonstrated. The challenge in future work is to make good insulating film coated on the whole cantilever and develop a process to expose the very of the probe to ensure accurate and nanoscale electrical measurements.

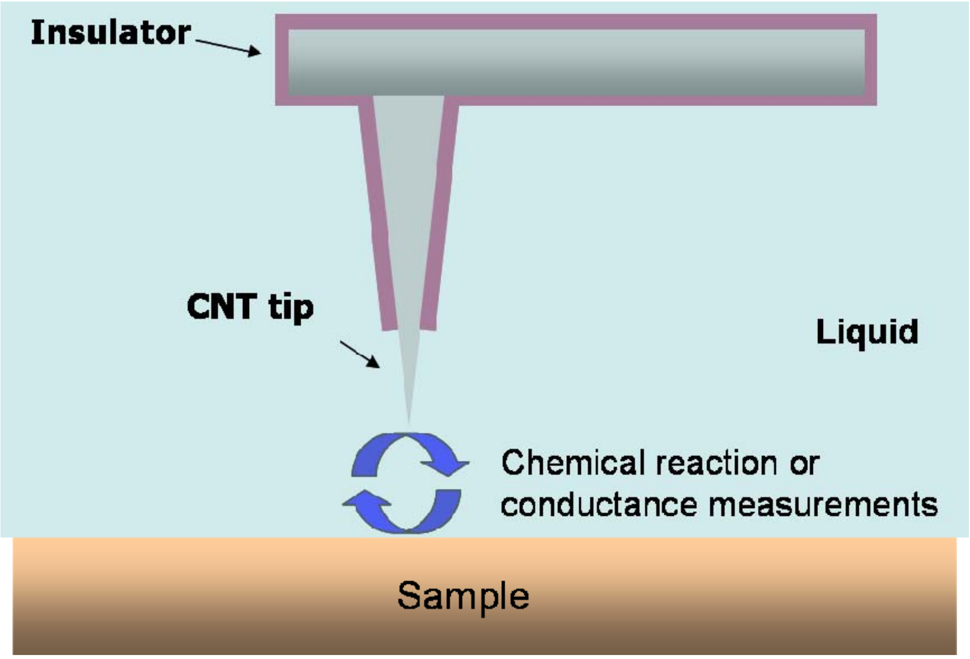

Figure 6.2 Schematic illustration of CNT-based probes for electrochemical or biological applications.

One of the most promising and near-term applications of CNTs is as probes for scanning probe microscopy, which is being recognized by commercial AFM vendors. There are still many work needed to do to further improve the imaging performance and fabricate CNT probes with high yield process for large-scale production. I believe that CNT probes can replace Si probes in some SPM applications after further improvements of the probe properties. Hopefully, the CNT probes and related fabrication methodologies presented in this study will be useful for a variety of other nanotech and biotech related applications, and helpful for commercialization of CNT probes.